On the multi-dimensional microparticle fractionation in a sharp-corner serpentine microchannel

An experimental and numerical study

Zur Erlangung des akademischen Grades Doktor-Ingenieur (Dr.-Ing.)
Genehmigte Dissertation von Sebastian Blahout aus Gladbeck
Tag der Einreichung: 25.01.2022, Tag der Prüfung: 13.04.2022

Erstreferentin: Prof. Dr.-Ing. Jeanette Hussong
Korreferent: Prof. Dr.-Ing. Christian Cierpka
Darmstadt

TECHNISCHE
UNIVERSITÄT
DARMSTADT

Mechanical Engineering
Department

On the multi-dimensional microparticle fractionation in a sharp-corner serpentine microchannel
An experimental and numerical study

Accepted doctoral thesis by Sebastian Blahout

Erstreferentin: Prof. Dr.-Ing. Jeanette Hussong
Korreferent: Prof. Dr.-Ing. Christian Cierpka

Date of submission: 25.01.2022
Date of thesis defense: 13.04.2022

Darmstadt

For Sandra.

Erklärungen laut Promotionsordnung

§8 Abs. 1 lit. c PromO

Ich versichere hiermit, dass die elektronische Version meiner Dissertation mit der schriftlichen Version übereinstimmt.

§8 Abs. 1 lit. d PromO

Ich versichere hiermit, dass zu einem vorherigen Zeitpunkt noch keine Promotion versucht wurde. In diesem Fall sind nähere Angaben über Zeitpunkt, Hochschule, Dissertationsthema und Ergebnis dieses Versuchs mitzuteilen.

§9 Abs. 1 PromO

Ich versichere hiermit, dass die vorliegende Dissertation selbstständig und nur unter Verwendung der angegebenen Quellen verfasst wurde.

§9 Abs. 2 PromO

Die Arbeit hat bisher noch nicht zu Prüfungszwecken gedient.

Darmstadt, 25.01.2022

S. Blahout

Abstract

In this thesis, the multi-dimensional fractionation of particles smaller than 10 µm with respect to their size and density is investigated inside a sharp-corner serpentine microchannel by means of experimental as well as numerical methods.
The motivation for research on multi-dimensional particle fractionation methods is twofold. First, particles with highly specified characteristics are the basis for various products of several different industries. Second, due to environmental or sustainability requirements, particles with defined properties are targeted to be extracted from a bulk quantity. Passive microfluidic approaches have a large potential to provide such fractionation methods, due to their simplicity and parallelizability. One of these approaches is fractionation in sharp-corner serpentine microchannels. This approach is investigated in the present thesis.
Long-exposure measurements are performed to investigate the general behavior of particles of several sizes and different densities at various bulk Reynolds numbers (chapter 4). Besides the confirmation of the high potential of the used method to fractionate micron sized particles with regard to their size, the results also reveal the potential to fractionate particles solely with regard to their density. Furthermore, it is demonstrated that the used method is suitable to focus sub-micron particles on distinct trajectories.
The reconstruction of three-dimensional particle distributions additionally reveals that micron particles with different sizes and densities not only move on trajectories that are spatially separated in-plane, but also out-of-plane (chapter 5). Astigmatism Particle Tracking Velocimetry measurements also enable to determine a size fractionation performance of nearly 100%.
To surpass qualitative descriptions of the force contributions that are relevant for the particle motion inside a serpentine microchannel, numerical simulations are performed (chapter 6). A detailed evaluation of the simulation results reveals that the contributions of the shear-gradient force and depending on the particle size also the drag force are dominant for the motion of a particle inside a serpentine loop under the investigated conditions.
Moreover, a new extension of micro Particle Image Velocimetry is presented that provides the opportunity to measure the bulk dynamics of both phases of a suspension flow simultaneously (chapter 7). For this, a labelling procedure is used to create suspension particles with a ring-shaped particle image. A comparison with Gaussian and plateau-shaped particle images showed the superior characteristics of such ring-shaped particle images with respect to measurement accuracy.

Zusammenfassung

In dieser Arbeit wird die mehrdimensionale Fraktionierung von Partikeln kleiner als 10 µm hinsichtlich ihrer Größe und Dichte in einem Serpentinen-Mikrokanal mittels experimenteller und numerischer Methoden untersucht.
Die Erforschung mehrdimensionaler Partikel-Fraktionierungsmethoden wird durch zwei Anwendungsgebiete motiviert. Zum einen bilden Partikel mit hochspezifischen Eigenschaften die Basis für verschiedene technische Produkte. Zum anderen bedingen Anforderungen des Umweltschutzes und der Nachhaltigkeit, die Extraktion von Partikeln mit definierten Eigenschaften aus verschiedensten Substanzen. Passive, mikrofluidische Fraktionierungs-Ansätze haben hierzu aufgrund ihrer Einfachheit und Parallelisierbarkeit ein großes Potenzial. Einer dieser Ansätze, die Fraktionierung in Serpentinen-Mikrokanälen, wird in dieser Arbeit untersucht.
Dazu werden Messungen mittels Langzeit-Belichtung durchgeführt, um das Verhalten von Partikeln unterschiedlicher Größe und Dichte bei diversen Bulk-Reynoldszahlen zu untersuchen (Kapitel 4). Die Ergebnisse bestätigen das große Potenzial der verwendeten Methode zur Größenfraktionierung von Mikro-Partikeln. Außerdem werden Möglichkeiten aufgezeigt, Partikel ausschließlich aufgrund ihrer Dichte zu fraktionieren. Es wird ebenfalls gezeigt, dass die verwendete Methode geeignet ist, um Submikro-Partikel auf definierten Trajektorien zu fokussieren.
Die Rekonstruktion dreidimensionaler Partikelverteilungen zeigt darüber hinaus, dass sich Mikro-Partikel mit unterschiedlichen Größen und Dichten nicht nur innerhalb einer Ebene auf räumlich getrennten Bahnen, sondern auch auf unterschiedlichen Höhenpositionen bewegen (Kapitel 5). Die dabei eingesetzte Astigmatism Particle Tracking Velocimetry ermöglicht es, einen Trenngrad von nahezu 100% für die Größenfraktionierung zu bestimmen.
Um das qualitative Verständnis des die Partikel-Bewegung bestimmenden Kräftegleichgewichtes zu erweitern, werden numerische Simulationen durchgeführt (Kapitel 6). Die detaillierte Auswertung der Simulationsergebnisse zeigt, dass für die untersuchten Bedingungen Schergradienten und je nach Partikelgröße auch Widerstandskräfte die Partikelbewegung innerhalb einer Serpentine dominieren.
Außerdem wird eine neue Erweiterung der micro Particle Image Velocimetry vorgestellt. Diese ermöglicht die simultane Bestimmung der Dynamik beider Phasen einer Suspensions-Strömung (Kapitel 7). Dazu wird ein Labelling-Verfahren verwendet, um Suspensions-Partikel mit ringförmigem Partikelbild zu erzeugen. Ein Vergleich mit Gauß'schen- und plateauförmigen Partikelbildern zeigt die überlegenen Eigenschaften ringförmiger Partikelbilder hinsichtlich der Messgenauigkeit.

Journal publications

Blahout, S., Reinecke, S.R., Kruggel-Emden, H., Hussong, J., 2021. On the micro-PIV accuracy and reliability utilizing non-Gaussian particle images. Exp. Fluids 62, 191. DOI: 10.1007/s00348-021-03283-8.

Reinecke, S.R., Blahout, S., Rosemann, T., Kravets, B., Wullenweber, M., Kwade, A., Hussong, J., Kruggel-Emden, H., 2021. DEM-LBM simulation of multidimensional fractionation by size and density through deterministic lateral displacement at various Reynolds numbers. Powder Technol. 385, 418–433. DOI: 10.1016/j.powtec.2021.02.062

Blahout, S., Reinecke, S.R., Kazerooni, H.T., Kruggel-Emden, H., Hussong, J., 2020. On the 3D Distribution and Size Fractionation of Microparticles in a Serpentine Microchannel. Microfluid. Nanofluidics 1–10. DOI: 10.1007/s10404-020-2326-7

Kottmeier, J., Wullenweber, M., Blahout, S., Hussong, J., Kampen, I., Kwade, A., Dietzel, A., 2019. Accelerated Particle Separation in a DLD Device at Re $>$ 1 Investigated by Means of µPIV. Micromachines 10, 768. DOI: 10.3390/mi10110768

Conference proceedings

Blahout, S., Reinecke, S.R., Kruggel-Emden, H., Hussong, J., 2019. Experimental study on size fractionation of micro particles in serpentine micro channels, in: PARTEC 2019 - International Congress on Particle Technology. Nuremberg.

Blahout, S., Reinecke, S.R., Kruggel-Emden, H., Hussong, J., 2019. Hydrodynamic size and density fractionation of microparticles in a serpentine channel, in: 27. Fachtagung "Experimentelle Strömungsmechanik." Erlangen.

Reinecke, S.R., Rosemann, T., Kruggel-Emden, H., Blahout, S., Hussong, J., 2019. Coupled DEM / LBM Simulation of DLD Fractionation, in: PARTEC 2019 - International Congress on Particle Technology. Nuremberg.

Blahout, S., Hussong, J., 2018. Determination of fluid-particle slip velocities of microfluidic suspension flows by means of micro-PIV, in: 26. Fachtagung "Experimentelle Strömungsmechanik." Rostock.

Blahout, S., Hussong, J., 2017. Reduced Estimation Error of Cross-Correlation Based Displacements of Refractive Index Matched and Surface Labelled Suspension Particles, in: 25. Fachtagung "Experimentelle Strömungsmechanik." Karlsruhe.

Nomenclature

Acronyms

APTV	Astigmatism Particle Tracking Velocimetry
CCD	Charge-coupled device
DEM	Discrete Element Method
DLDF	Deterministic Lateral Displacement Fractionation
DPM	Discrete Particle Method
FOV	Field of view
FP	Focal plane
FWHM	Full width at half maximum
LBM	Lattice Boltzmann Method
LDV	Laser Doppler Velocimetry
LIF	Laser Induced Fluorescence
LL	Lower limit
MF	Melamine resin
MOFF	Multi Orifice Fluid Fractionation
MRT	Multiple Relaxation Times
Nd:YAG	Neodymium-doped Yttrium Aluminum Garnet
OPF	One phase flow
PIV	Particle Image Velocimetry
PMMA	Polymethylmethacrylate
PS	Polystyrene

PTV	Particle Tracking Velocimetry	
RMS	Root mean square	
RMSE	Root mean square error	
SCL	Suspension carrier liquid	
SP	Suspension particles	
UL	Upper limit	

Greek letters

α	General parameter	-
β	General parameter	-
γ	General parameter	-
Δ	Temporal distance	s
δ	Spatial distance	m
ϵ	Error	-
$\hat{\epsilon}$	Peak fit estimator	-
η	Dynamic viscosity	$\mathrm{Pa\,s}$
κ	Selectivity	-
λ	Wavelength	m
μ	Mean value	-
ν	Kinematic viscosity	$\mathrm{m^2\,s^{-1}}$
ρ	Volumetric mass density	$\mathrm{kg\,m^{-3}}$
$\boldsymbol{\sigma}$	Fluid stress tensor	$\mathrm{N\,m^{-2}}$
σ	Standard deviation	-
σ^2	Variance	-
τ	Relaxation time	-
ϕ	General quantity	-
φ	Particle volume concentration	-

χ	General exponent	-
$\boldsymbol{\Omega}$	Angular velocity vector of particle rotation	$\mathrm{rad\,s^{-1}}$
$\boldsymbol{\omega}$	Angular velocity vector of particle trajectory	$\mathrm{rad\,s^{-1}}$

Indices

a	Approximate
b	Bulk
bn	Binormal to main flow direction
bottom	Bottom
buo	Buoyancy
C	Quantity related to the image mean intensity
c	Centrifugal
cc	Cross-correlated
D	Quantity related to the particle image displacement
d	Drag
Disc	Discretization
DoC	Depth of correlation
e	Extrapolated
F	Quantity related to the image fluctuating noise
G	Gaussian
g	Gravitational
h	Hydraulic
I	Quantity related to the image plane
i	General index
in	Quantity in image in-plane direction
It	Iteration
IW	Quantity related to the interrogation window

j	General index	
l	Quantity related to the liquid phase	
m	In main flow direction	
max	Maximum	
misc	Miscellaneous	
n	Normal to main flow direction	
out	Quantity in image out-of-plane direction	
p	Particle related quantity	
ppp	Particles per pixel	
R	Quantity related to the correlation plane	
r	Refinement	
ref	Reference	
rel	Relative	
rot	Rotational	
S	Quantities related to the particle surface	
s	Shear-gradient	
Saffman	Saffman	
Top	Top	
V	Quantities related to a volume	
x	In x-coordinate direction	
y	In y-coordinate direction	
z	In z-coordinate direction	

Latin letters

A	Cross-sectional area	m^2
a	Major/minor axis length of an auto-correlation peak	px
C	General coefficient	-

D	Detectability	-
d	Diameter	m
$\boldsymbol{F}$	Force vector	N
F	Loss of correlation factor	-
f	Focal length	m
$\boldsymbol{g}$	Gravitational vector	$\mathrm{m\,s^{-2}}$
GCI	Grid convergence index	-
H	Height	m
h	Characteristic grid size	m
I	Intensity distribution	-
K	Number of intersected particle images	-
L	Characteristic length	m
l	Length	m
M	Optical magnification	-
m	Mass	kg
$\boldsymbol{n}$	Normal vector	-
N	Number of a quantity	-
n	Refractive index at the sodium D-line	-
NA	Numerical aperture	-
P	Probability	-
p	Static pressure	Pa
Q	Volume flow rate	$\mathrm{m^3\,s^{-1}}$
$\boldsymbol{r}$	Radial position vector	m
R	Cross-correlation function	-
r	Radius	m
Re	Reynolds number	-

$\boldsymbol{s}$	Separation vector	-
S	Surface	m^2
SNR	Signal to noise ratio	-
St	Stokes number	-
T	Separation degree	-
t	Time	s
$\boldsymbol{u}$	Velocity vector	$\mathrm{m\,s^{-1}}$
U	Uncertainty	-
u	Component of the velocity vector in x-direction	$\mathrm{m\,s^{-1}}$
V	Volume	m^3
v	Component of the velocity vector in y-direction	$\mathrm{m\,s^{-1}}$
W	Width	m
w	Component of the velocity vector in z-direction	$\mathrm{m\,s^{-1}}$
$\boldsymbol{X}$	Position vector	-
x'	Coordinate from inner to outer wall	-
x	Cartesian coordinate system axis	-
y	Cartesian coordinate system axis	-
z	Cartesian coordinate system axis	-

Contents

List of Figures

List of Tables

1. Introduction[1]

Fractionation methods that are capable to separate particles with respect to multiple characteristics are the basis for particle products with highly specified properties. In the present thesis, the ability of a sharp-corner serpentine microchannel to realize such a multi-dimensional particle fractionation is investigated. The motivation for these investigations and the background of microfluidic fractionation systems is provided in section 1.1 of this introductory chapter. The objective and an outline of this thesis is given in section 1.2.

1.1. Motivation and background

Particles with diameters below 10 µm and well-defined properties are increasingly used in the pharmaceutical and chemical industry, but also in the field of metallurgy (Baghban Taraghdari et al., 2019; Li et al., 2019; Kumar and Venkatesh, 2019). Thus, multi-dimensional fractionation processes are essential to fabricate intermediate particle products with e.g. monodisperse size, shape or surface properties. Multi-dimensional fractionation methods are also relevant in the field of medical diagnostics, e.g. to enrich or isolate rare cells like cancer cells in human blood samples (Nagrath et al., 2007; Talasaz et al., 2009). Another field in which multi-dimensional particle fractionation methods are of high potential is electronic waste recycling (Spengler et al., 2003; F. Wang et al., 2017). Even smaller particles in the sub-micrometer and nanometer scale with highly specific characteristics are the basis e.g. for ultrasensitive sensor technologies (Gloag et al., 2019) and have been recently developed for the removal of aqueous pollutants from waste water (Ali et al., 2017).
Overall, there is a huge demand for fractionation methods that are capable to separate micron and sub-micron particles with regard to multiple characteristics. Current research focuses on the development and analysis of existing and new fractionation methods to realize a multi-dimensional fractionation with respect to various particle properties. Typical particle properties that are utilized for fractionation are the particle size and shape, but also the wettability (Leistner et al., 2019; Menter and Segets, 2019; Schreier and Bröckel, 2021), the surface roughness (Olszok et al., 2020) or the electrophoretic mobility (Lösch et al., 2021;

[1] Parts of this chapter are published in Blahout et al. (2020) and Blahout et al. (2021), used under CC BY 4.0. The original contents have been edited and/or extended for this work.

Barasinski and Garnweitner, 2020).
Promising candidates for the realization of multi-dimensional particle fractionation can be found in the field of microfluidics. Such microfluidic systems allow a continuous fractionation process and are generally characterized by small device footprints, which enables to realize a high throughput by parallelization and the usage of small samples (Sajeesh and Sen, 2014). Moreover, microfluidic devices may utilize particle migration effects in a laminar flow, driven by high local velocities and velocity gradients without suffering from undesirable transient flow effects. Consequently, microparticle fractionation has been realized in microchannels by means of active and passive approaches. Active approaches utilize external acoustic, magnetic or electrical force fields (Jo and Guldiken, 2012; Suwa and Watarai, 2011; Podoynitsyn et al., 2019). Passive approaches rely on the interaction of particles with solid structures inside the microchannel or solely on hydrodynamic forces. For example, the interaction of suspended particles with an array of micropillars is utilized in the Deterministic Lateral Displacement Fractionation (DLDF). Here, particles are spatially separated based on their size or density (Reinecke et al., 2021). Recent studies also showed that high throughputs can be realized inside DLDF arrays (Kottmeier et al., 2019). In contrast to this, inertial effects may be utilized to force particles on spatially separated trajectories, whose position depends on both, the particle and fluid flow properties. Inertial effects include particle centrifugal forces as well as inertial particle migration, which is present if the particle diameter is large compared to the channel dimensions (Di Carlo, 2009). A common passive microfluidic fractionation approach that utilizes inertial effects is the Multi Orifice Fluid Fractionation (MOFF) (Sim et al., 2011; L. L. Fan et al., 2014; L.-L. Fan et al., 2015) or the fractionation in expansion-contraction microchannels (Park and Jung, 2009; Mach et al., 2011; Kwak et al., 2018; Jiang et al., 2019). These approaches enhance particle migration by inducing strongly curved streamlines such that a decrease in particle focusing length is achieved.
Spiral and serpentine microchannels have been successfully utilized for particle fractionation (Bhagat et al., 2008; Zhang et al., 2014a). In such channels, Dean vortices are induced due to the channel curvature. In combination with centrifugal forces and hydrodynamic shear forces, particles develop Reynolds number dependent equilibrium trajectories (Di Carlo, 2009; Zhang et al., 2014b).
In the present work a sharp-corner serpentine microchannel is utilized to investigate the ability to realize multi-dimensional fractionation of micron and sub-micron particles with respect to the particle size and density. Serpentine microchannels are generally characterized by periodically alternating flow directions. Besides serpentine geometries that realize sharp 90° turns, also sinusoidal or zigzag geometries have been investigated recently (Ying and Lin, 2019). Serpentine microchannels are promising to realize multi-dimensional fractionation with respect to the particle size and density. Whereas the ability for size fractionation is known (Zhang et al., 2014a), the presence of several flow direction changes induces centrifugal forces that are assumed to spatially separate particles of different densities, as aimed in the

present study. Further advantages of serpentine microchannels are amongst others that possibilities for parallelization are also present such that sufficient yields for industrial applications may be realized in the future. Another advantage of the serpentine microchannel geometry that is used in the present work is the realization of a constant cross-sectional area, which makes the system more robust against clogging compared to e.g. MOFF or DLDF devices. Furthermore, the passive fractionation method that is investigated in the present work, does not depend on the presence of external fields.

Previous experimental studies showed that in asymmetrical serpentine channels, micron and sub-micron sized particles can be focused to stable equilibrium positions (L. Wang and Dandy, 2017). Moreover, the number of equilibrium positions reduces in comparison to straight duct channel flows and the width of the resulting focusing streak is particle Reynolds number dependent (Di Carlo et al., 2007; Di Carlo et al., 2008). From studies of Di Carlo et al. (2008), it becomes evident that equilibrium trajectories narrow with increasing particle Reynolds number and start to blur above a critical Reynolds number. This effect was assumed to result from an increased magnitude of the secondary flow enhancing particle mixing. Further experimental studies aimed to improve the focusing concept to make it usable for practical applications. Oakey et al. (2010) showed that a combination of straight duct and serpentine microchannel stages can lead to a single particle equilibrium trajectory over the channel cross-section at a particle Reynolds number of $\mathrm{Re_p} = 6$ in the straight channel section. Furthermore, it was shown experimentally that the focusing streak width decreases with increasing particle concentration, which is assumed to result from hydrodynamic particle-particle interactions (Oakey et al., 2010). A more recent investigation utilized a sharp corner serpentine microchannel to investigate the importance of particle centrifugal forces and, therefore, of the density difference between the fluid and particles on the development of equilibrium trajectories (Zhang et al., 2014b). Zhang et al. (2014b) provided a scaling factor as a measure for the influence of the centrifugal force relatively to the Dean drag force on the development of particle equilibrium trajectories under the assumption of negligible inertial migration effects. As they also experimentally observed particle focusing for negligible inertial migration effects, this indicates that the density difference between particles and fluid and from this resulting centrifugal forces plays an important role for the development of particle equilibrium trajectories. Based on the knowledge that equilibrium trajectory locations are size and Reynolds number dependent in sharp corner serpentine microchannels, a spatial separation of particles with 3 µm and 10 µm diameter was reported by Zhang et al. (2014a). Extending these investigations, it was recently shown that the usage of an elastic carrier fluid can further accelerate particle focusing and, thus, allows a reduction of the total amount of serpentine loops (Yuan et al., 2019).

Although it was already shown that sharp-corner serpentine microchannels are able to focus particles below 10 µm diameter, detailed investigations that are able to explain the lateral migration of particles in such a flow are still subject of ongoing

research. A reason for this is that previous studies were only able to determine in-plane particle trajectories using fluorescence imaging, where usually long exposure times are used during the recording of particle fluorescence signals (Gossett and Carlo, 2009; Zhang et al., 2014a). This makes it impossible to determine details of the three-dimensional particle dynamics, which is essential to understand the particle migration and focusing behavior, as was also assumed in previous studies (Gossett and Carlo, 2009). Furthermore, the dependence of particle locations inside a sharp-corner serpentine microchannel on the particle density is not yet investigated systematically. The same is true for particles with sizes below 1 µm. The present thesis aims to identify parameters at which a multi-dimensional fractionation with respect to the particle size and density is promising. Moreover, a deeper understanding of the particle dynamics inside serpentine microchannels shall be achieved.

1.2. Objectives and outline of this thesis

The behavior of micron and sub-micron particles of different sizes and densities inside a sharp-corner serpentine microchannel is investigated in the present thesis to analyze its ability for multi-dimensional particle fractionation. With this, a basis is provided for future fractionation applications. For this purpose, different methods are utilized. On the experimental side, long-exposure fluorescence measurements are performed to identify regions at which particles of different size and density are spatially separated inside one serpentine loop. Additionally, Astigmatism Particle Tracking Velocimetry (APTV) is used to reconstruct three-dimensional particle distributions. This enables to determine also quantitatively the fractionation performance. Additionally, numerical simulations are conducted to analyze in detail the force balance that acts on particles during the flow through a single serpentine loop. To investigate such force balances also on the basis of experimental data, velocity fields of both, particles and the ambient fluid have to be known. Thus, a new extension of micro Particle Image Velocimetry (µPIV) is presented that enables the simultaneous determination of bulk velocity fields of both phases of a suspension. This is also relevant for investigations of flow fields inside microfluidic fractionation channels at high particle concentrations.
Relevant background information of inertial particle migration are provided in **chapter 2**. Here, fundamentals of the Astigmatism Particle Tracking Velocimetry and the micro Particle Image Velocimetry approach are given, as well.
The experimental and numerical set-ups that are used for the investigations of this thesis are described in **chapter 3**. Here, also detailed descriptions of individual execution and evaluation procedures are provided.
The general behavior of micron and sub-micron particles inside the sharp-corner serpentine microchannel flow is investigated in **chapter 4**. For this, long-exposure measurements of various particle fractions at different bulk Reynolds numbers and

measurement locations are analyzed.
A detailed investigation of the three-dimensional distribution of micron particles of different size and density is provided in **chapter 5**. This is based on measurements that are performed with the Astigmatism Particle Tracking Velocimetry (APTV) measurement technique.
To identify relevant force contributions that are responsible for the development of distinct particle trajectories, a numerical study is carried out to simulate the trajectories of selected particles at specific bulk Reynolds numbers. The analysis of the resulting force distributions along individual particle trajectories can be found in **chapter 6**.
Possibilities to measure the bulk dynamics of both phases of a suspension simultaneously are investigated in **chapter 7**. For this purpose, the micro Particle Image Velocimetry (µPIV) approach is extended by using standard tracers and significantly larger suspension particles that display a ring-shaped particle image at the same time. The performance of such ring-shaped particle images with regard to the accuracy and reliability in a cross-correlation based evaluation algorithm is investigated on the basis of synthetically generated particle images as well as in an exemplary experimental measurement situation.
In **chapter 8** the main results that are obtained from the previously described studies are summarized. Additionally, an outlook is provided that recommends directions for further investigations.

2. Theoretical background

Passive, hydrodynamic microparticle fractionation in a microfluidic device aims at focusing particles with different properties on spatially separated equilibrium trajectories. Force contributions that are relevant for the development of such trajectories are described in section 2.1.
The investigations of this work utilize optical measurement techniques to determine particle distributions as well as fluid velocity fields. Specifically, Astigmatism Particle Tracking Velocimetry (APTV) and micro Particle Image Velocimetry (µPIV) measurements are performed. The basic principles of both measurement techniques are described in section 2.2.

2.1. Inertial particle migration

Responsible for the evolution of particle property dependent equilibrium trajectories in a microfluidic device is a combination of particle volume forces and hydrodynamic forces acting on the particle surface. Volume forces result from external fields acting on a particle or particle inertia. In contrast to this, surface forces are a result of finite size effects. A particle that is large compared to characteristic fluid flow structures induces inertial migration. First experimental studies of the migration of $d_\mathrm{p} = \mathcal{O}(1\,\mathrm{mm})$ particles in a Poiseuille tube flow were performed by Segré and Silberberg and showed that particles focus at an annulus of approximately 0.6 times the tube radius (Segré and Silberberg, 1962a; Segré and Silberberg, 1962b). This inertial migration effect could later be explained to result from an equilibrium of shear-gradient and wall lift forces (Ho and Leal, 1974; Asmolov, 1999). During the last decades, particle migration and underlying hydrodynamic drag and lift forces have been investigated. Maxey and Riley (1983) assumed infinitely small particles and derived a set of equations considering shear-gradient and Stokes drag but also time-dependent contributions, i.e. virtual mass and history forces (Maxey and Riley, 1983). Later studies aimed to extend the Maxey-Riley equations to develop a model that is also valid for finite particle sizes and Reynolds numbers, as well as for non-uniform, unsteady flow conditions (Loth and Dorgan, 2009). Loth and Dorgan (2009) provide a model to calculate the net lift force on suspended particles if the detailed flow field around a particle is unknown. This is usually the case not only in experimental investigations, but also in numerical simulations, if the particle size is of similar order of magnitude as the numerical mesh. In the last years, direct

numerical simulations have been performed where the flow field in the vicinity of suspended particles is fully resolved. In laminar and turbulent straight duct flow, such fully resolved simulations revealed that the particle migration dynamics strongly depends on the bulk Reynolds number (Kazerooni et al., 2017; Fornari et al., 2018).
Generally, the motion of a particle with mass m_p and diameter $d_\mathrm{p} = 2r_\mathrm{p}$ suspended in a fluid can be described as follows (Maxey and Riley, 1983):

$$\underbrace{m_\mathrm{p}\frac{d\boldsymbol{u}_\mathrm{p}}{dt}}_{I} = \underbrace{m_\mathrm{p}\boldsymbol{g}}_{II} + \underbrace{\oint_{S_\mathrm{p}} \boldsymbol{\sigma}\boldsymbol{n}\,\mathrm{d}S_\mathrm{p}}_{III} \tag{2.1}$$

It shall be noted that the index p denotes particle related quantities and bold variables denote vector quantities. Hence, S_p is the particle surface and $\boldsymbol{u}_\mathrm{p}$ the particle velocity vector. Furthermore, $\boldsymbol{\sigma}$ equals the fluid stress tensor with $\boldsymbol{n}$ being the outward facing normal vector. The no-slip boundary condition is obeyed at the particle surface, i.e. $\boldsymbol{u}|_{S_\mathrm{p}} = \boldsymbol{u}_\mathrm{p} + \boldsymbol{\Omega}_\mathrm{p} \times \boldsymbol{r}_\mathrm{p}$, with the angular particle velocity $\boldsymbol{\Omega}_p$ and the radial distance of a point on the particle surface to the particle center point $\boldsymbol{r}_\mathrm{p}$. Equation (2.1) relates inertial components of the particle motion (I) to volume forces, here the gravitational force (II) and the momentum exchange with the surrounding carrier liquid (III).
The challenge of solving (2.1) for a particle system lies in the determination of the fluid stress tensor $\boldsymbol{\sigma}$ as the exact velocity field distribution in the vicinity of a particle is usually unknown. Nowadays, fully resolved numerical simulations are capable to resolve the flow around individual particles even though they are computationally expensive (Breugem, 2012; Nakagawa et al., 2015; Kazerooni et al., 2017; Fornari et al., 2018). Experimentally it is even more challenging to determine the full stress tensor along the surface of a freely moving particle, especially if it is of micron size or even smaller. As current measurement techniques are seldom capable to resolve the flow around individual particles, models like the previously mentioned Maxey-Riley equation (Maxey and Riley, 1983) for point particles in Stokes flow or the Auton-Hunt-Prud'Homme equation for inviscid, rotational flow (Auton et al., 1988) can be used to determine fluid forces that act on suspended particles.
Generally, the right-hand-side of (2.1) can be expressed as the sum of dominating volume and surface forces $\boldsymbol{F}_\mathrm{V}$ and $\boldsymbol{F}_\mathrm{S}$ as follows (Loth and Dorgan, 2009):

$$m_\mathrm{p}\frac{d\boldsymbol{u}_\mathrm{p}}{dt} = \boldsymbol{F}_\mathrm{V} + \boldsymbol{F}_\mathrm{S} \tag{2.2}$$

$$\boldsymbol{F}_\mathrm{V} = \boldsymbol{F}_\mathrm{b} + \boldsymbol{F}_\mathrm{g} + \boldsymbol{F}_\mathrm{c} \tag{2.2a}$$

$$\boldsymbol{F}_\mathrm{S} = \boldsymbol{F}_\mathrm{d} + \boldsymbol{F}_\mathrm{s} + \boldsymbol{F}_\mathrm{Saffman} + \boldsymbol{F}_\mathrm{misc} \tag{2.2b}$$

Equation (2.2a) contains the buoyancy $\boldsymbol{F}_\mathrm{b}$, the gravitational $\boldsymbol{F}_\mathrm{g}$ force and the centrifugal force $\boldsymbol{F}_\mathrm{c}$. The buoyancy of a particle equals its displaced fluid weight. Buoyancy and gravitational force can be combined for a spherical particle of

constant density ρ_p that is suspended in a fluid with constant density ρ, as follows:

$$\boldsymbol{F}_\mathrm{b} + \boldsymbol{F}_\mathrm{g} = m_\mathrm{p}\boldsymbol{g}\left(1 - \frac{\rho}{\rho_\mathrm{p}}\right) \tag{2.3}$$

If a suspended particle follows a curved streamline, as sketched in Figure 2.1(a), a

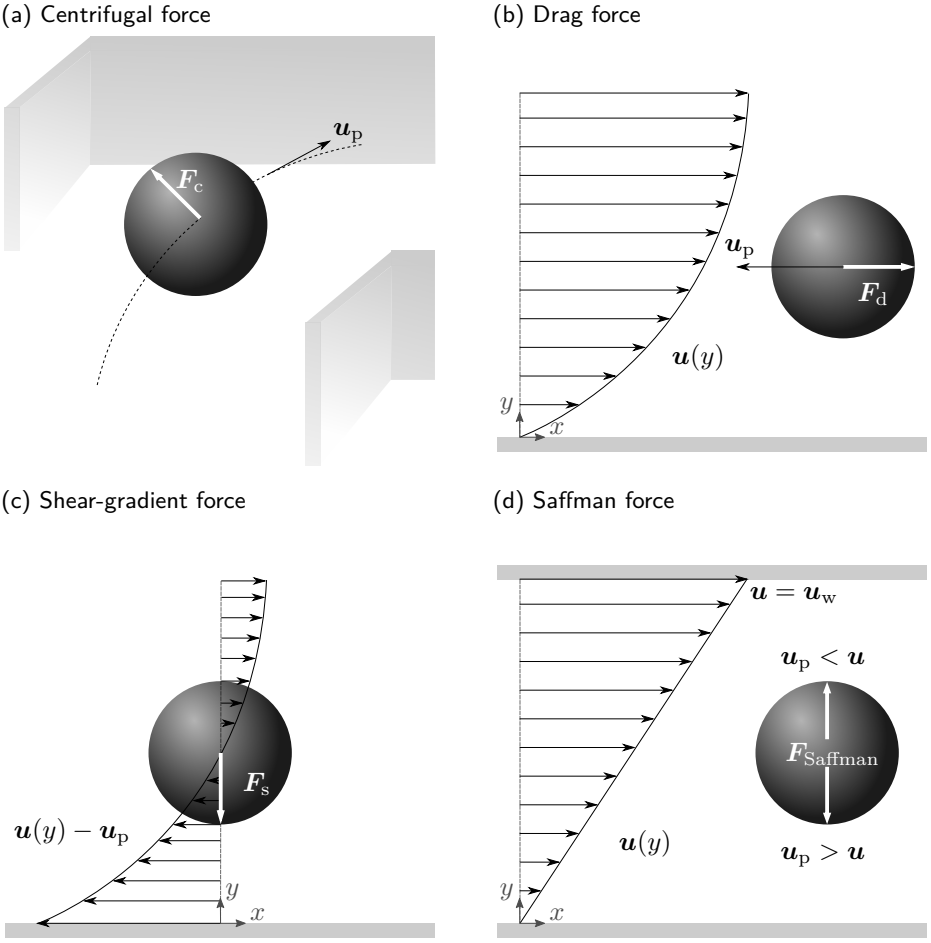

Figure 2.1.: Schematic illustrations of the working mechanism of (a) the centrifugal force $\boldsymbol{F}_\mathrm{c}$; (b) the drag force $\boldsymbol{F}_\mathrm{d}$; (c) the shear-gradient force $\boldsymbol{F}_\mathrm{s}$ and (d) the Saffman force $\boldsymbol{F}_\mathrm{Saffman}$. Illustrations are inspired by Martel and Toner (2014) and Zhang et al. (2016).

fictitious centrifugal force $\boldsymbol{F}_\mathrm{c}$ has to be considered to describe the particle movement. The centrifugal force reads in the particle frame:

$$\boldsymbol{F}_\mathrm{c} = -\frac{1}{6} \cdot (\rho_\mathrm{p} - \rho) \cdot \pi \cdot d_\mathrm{p}^3 \cdot \boldsymbol{\omega}_\mathrm{p} \times (\boldsymbol{\omega}_\mathrm{p} \times \boldsymbol{r}) \tag{2.4}$$

Here, $\boldsymbol{\omega}_\mathrm{p}$ denotes the angular velocity of a particle that follows a curved trajectory and $\boldsymbol{r}$ is the distance vector between the particle center point and the center of the trajectory on which the particle is moving.
Hydrodynamic force contributions that act on the surface of a particle are here divided into the drag force $\boldsymbol{F}_\mathrm{d}$, the shear-gradient force $\boldsymbol{F}_\mathrm{s}$, the Saffman force $\boldsymbol{F}_\mathrm{Saffman}$ and a contribution that summarises miscellaneous lift forces $\boldsymbol{F}_\mathrm{misc}$. The first three force contributions are discussed in the following in detail. These formulations are also considered for simulations with OpenFOAM v1912 and for an investigation of the particle dynamics inside a sharp-corner serpentine microchannel (see chapter 6). Forces that are summarized in the term $\boldsymbol{F}_\mathrm{misc}$ are shortly described afterwards and are not explicitly considered in the further investigations of the present thesis.
If a suspended particle moves with a non-zero relative velocity $(\boldsymbol{u} - \boldsymbol{u}_\mathrm{p}) \neq 0$ in a fluid, a viscous drag force $\boldsymbol{F}_\mathrm{d}$ arises. This situation is sketched in Figure 2.1(b). The drag force that acts on a spherical particle can be expressed as follows:

$$\boldsymbol{F}_\mathrm{d} = \frac{1}{8}\pi\rho \left(\boldsymbol{u} - \boldsymbol{u}_\mathrm{p}\right)^2 d_\mathrm{p}^2 \cdot C_\mathrm{d} \tag{2.5}$$

Investigations of the drag force coefficient C_d led to various analytical and empirical formulations that take the particle Reynolds number as well as the particle shape into account and are still topic of current research (Song et al., 2017; Davuluri et al., 2021). An overview of various formulations is provided by Goossens (2019). Here, the drag force coefficient that is provided by Klyachko (1934) and that is first cited by Torobin and Gauvin (1959) is used for a particle Reynolds number below $\mathrm{Re}_\mathrm{p} \leq 1000$:

$$C_\mathrm{d} = \frac{24}{\mathrm{Re}_\mathrm{p}} \left(1 + \frac{1}{6}\mathrm{Re}_\mathrm{p}^{\frac{2}{3}}\right) \tag{2.6}$$

and is set constant to $C_\mathrm{d} = 0.424$ for $\mathrm{Re}_\mathrm{p} > 1000$. The particle Reynolds number is defined as:

$$\mathrm{Re}_\mathrm{p} = \left(\rho \cdot |(\boldsymbol{u} - \boldsymbol{u}_\mathrm{p})| \cdot d_\mathrm{p}\right) / \eta, \tag{2.7}$$

whereas η denotes the dynamic fluid viscosity. For $\mathrm{Re}_\mathrm{p} \ll 1$, (2.5) reduces to the well-known Stokes drag force. In curved microchannels, the particle motion is influenced by secondary flow motion. In particular, the channel curvature leads to two counter-rotating Dean vortices (Dean, 1928). These are a result of faster fluid at the microchannel center that is driven towards the outer microchannel wall due to higher inertia. As this motion is confined by the microchannel side walls, a recirculation along the top and bottom walls towards the microchannel center

occurs. Consequently, a lateral drag force component, also called Dean drag force, is present, if the lateral fluid velocity that results from the presence of such Dean vortices differs from that of suspended particles.
In laminar, pressure-driven flows, the influence of the velocity gradient on the movement of a neutrally buoyant, spherical particle with zero slip velocity is taken into account by the shear-gradient force $\boldsymbol{F}_\mathrm{s}$ (Ho and Leal, 1974; Schonberg and Hinch, 1989; Martel and Toner, 2014; Liu et al., 2019). The shear-gradient force results from an asymmetrical relative velocity distribution around a suspended particle, as sketched in Figure 2.1(c). In such situations also an asymmetrical pressure distribution around a suspended particle evolves. Thus, the resulting force drives a particle towards the side of lower pressure, i.e. maximum relative velocity and can be interpreted as a type of lift force. The shear-gradient force reads (Maxey and Riley, 1983):

$$\boldsymbol{F}_\mathrm{s} = \rho V_\mathrm{p} \left(\frac{D\boldsymbol{u}}{Dt} \right) \tag{2.8}$$

Here, V_p is the particle volume and $(D\boldsymbol{u}/Dt)$ denotes the fluid velocity material derivative applied at the particle centroid (Maxey and Riley, 1983).
The Saffman force $\boldsymbol{F}_\mathrm{Saffman}$ describes the lateral force contribution that occurs if a neutrally buoyant particle has a non-zero relative velocity in a linear shear flow, i.e. in absence of a flow profile curvature. The Saffman force also emerges due to an asymmetrical relative velocity distribution around a suspended particle. Similar as for the shear-gradient force, the Saffman force drives a particle towards the region of higher relative velocity, as also shown in Figure 2.1(d). Over the decades, several theoretical approaches have been made to extend the initial formulation of Saffman (1965) including neutrally and non-neutrally buoyant particles as well as Reynolds numbers of up to 700 (Asmolov, 1999). In the present work, the Saffman-Mei lift force is utilized, which reads (Mei, 1992):

$$F_\mathrm{Saffman} = m_\mathrm{p} \frac{\rho}{\rho_\mathrm{p}} C_\mathrm{Saffman} \cdot (\boldsymbol{u} - \boldsymbol{u}_\mathrm{p}) \times (\boldsymbol{\nabla} \times \boldsymbol{u}) \tag{2.9}$$

It shall be noted that (2.9) only considers the rotation of the fluid velocity field and is independent of particle rotation. The Saffman force coefficient C_Saffman is particle Reynolds number dependent and reads:

$$C_\mathrm{Saffman} = \frac{3}{2\pi\sqrt{\mathrm{Re}_\mathrm{rot}}} \cdot 6.46 \cdot \gamma, \qquad \mathrm{Re}_\mathrm{p} \leq 40 \tag{2.10}$$

$$C_\mathrm{Saffman} = \frac{3}{2\pi\sqrt{\mathrm{Re}_\mathrm{rot}}} \cdot 6.46 \cdot 0.0524 \cdot \sqrt{\beta \cdot \mathrm{Re}_\mathrm{p}}, \qquad \mathrm{Re}_\mathrm{p} > 40 \tag{2.11}$$

Parameters γ, α and β that are used in (2.10) and (2.11) read (Mei, 1992):

$$\gamma = (1 - \alpha) \cdot e^{-0.1\mathrm{Re_p}} + \alpha \tag{2.12}$$

$$\alpha = 0.3314 \cdot \sqrt{\beta} \tag{2.13}$$

$$\beta = 0.5 \cdot \frac{\mathrm{Re_{rot}}}{\mathrm{Re_p}} \tag{2.14}$$

Furthermore, $\mathrm{Re_{rot}}$ denotes the Reynolds number that takes the curl of the fluid velocity field into account:

$$\mathrm{Re_{rot}} = \frac{\rho}{\eta} \cdot |(\boldsymbol{\nabla} \times \boldsymbol{u})| \cdot d_\mathrm{p}^2 \tag{2.15}$$

Other force contributions that may become relevant to describe the motion of a suspended particle are summarized in the quantity F_misc in the present work. It shall be noted that these force contributions are not explicitly considered in the following investigations of this thesis. Such additional force contributions are the virtual mass or also called added mass force, the Basset or also called history force, the Magnus force and the wall lift force. These force contributions are shortly described in the following.

The virtual or added mass force occurs, if a suspended particle accelerates relative to the ambient fluid. It is a result of the additional momentum transfer that is necessary to displace the fluid in the vicinity of a particle. Formulations of the virtual mass force for spherical particles are given in D. Drew et al. (1979), D. A. Drew and Lahey (1987), and Wakaba and Balachandar (2007), respectively.

Additionally to the virtual mass force, the development of the boundary layer at the particle surface may be delayed, if a suspended particle accelerates relative to the fluid flow and a resistance force emerges that is called Basset or history force (Loth and Dorgan, 2009). To calculate the history force, a time integral of the particle relative movement has to be solved that includes also a particle Reynolds number dependent history kernel. Various studies aimed to find expressions for this history kernel which are feasible for different flow situations and computationally efficient (Mei and Adrian, 1992; Hinsberg et al., 2011).

If a particle rotates with a non-zero angular velocity and moves relative to the surrounding fluid the Magnus force acts as a lift force. The Magnus lift force drives a particle towards the direction that is perpendicular to the plane spanned by the relative translation velocity and the rotation axis.

The hydrodynamic interaction of a suspended particle and the channel walls may lead to a perturbed velocity field that results in a wall lift force (Vasseur and Cox, 1977). To address this, Zeng et al. (2005) utilize fully resolved numerical simulations of a particle that moves at certain distances parallel to a wall in a quiescent fluid. It is revealed that a local acceleration of the fluid in the gap between the particle and the channel wall occurs. Therefore, one force contribution of the wall lift force acts towards the wall. On the other hand, the region between wall and particle acts

as flow constriction, leading to a lubrication lift due to an increased pressure region that drives the particle away from the wall. This was found to be the dominant contribution of the wall lift force (Takemura and Magnaudet, 2003). In general, the wall lift force is a function of the particle Reynolds number and the wall distance of a particle (Vasseur and Cox, 1977; Takemura and Magnaudet, 2003; Zeng et al., 2005).
With the set of equations that can be utilized for (2.2a) and (2.2b), a model is available to determine the hydrodynamic forces that dominate the motion of a suspended particle, even if not all details of the flow field around a particle are known. This is usually the case in experimental investigations of the particle bulk behavior, but also in numerical simulations, if a particle is of a similar order of magnitude as the cells of the numerical grid. In such situations, the general knowledge of the bulk velocity fields and velocity gradients of the underlying flow field can be utilized to determine individual force components and thus the motion of a suspended particle.

2.2. Optical measurement techniques for microscopic flows

To investigate microparticle dynamics in a microfluidic system, dedicated optical measurement techniques are required to gain access to the particle and the flow field dynamics. In this thesis, long-exposure fluorescence microscopy and Astigmatism Particle Tracking Velocimetry (APTV) measurements are performed in a sharp-corner serpentine microchannel to determine the bulk dynamics of suspended microparticles. The basic concept of the APTV measurement approach is described in section 2.2.1.
An extension of micro Particle Image Velocimetry (µPIV) that enables the simultaneous determination of the bulk velocity fields of both phases of a suspension is introduced in chapter 7. For this, the dependency of the measurement accuracy and reliability on the particle image shape is investigated. The theoretical background that provides the basis for this study is described in section 2.2.2.

2.2.1. Astigmatism Particle Tracking Velocimetry[1]

Astigmatism Particle Tracking Velocimetry (APTV) combines a Particle Tracking Velocimetry (PTV) approach with a reconstruction method of the out-of-plane position of a particle from in-plane recordings based on astigmatic imaging of particles. In contrast to the (µ)PIV measurement technique, the seeding density is lower for APTV measurements. Typical effective particle image densities for APTV measurements are in the order of magnitude of $N_{\mathrm{ppp}} = \mathcal{O}\left(10^{-4}\right)$. Thus,

[1] Parts of this section are published in Blahout et al. (2020), used under CC BY 4.0. The original contents have been edited and/or extended for this work.

the probability of overlapping particle images is reduced allowing the detection of individual particle images. This is especially important in APTV measurements, as the characteristics of particle images have to be matched with corresponding calibration data and the size of particle images is increased due to the astigmatism. Furthermore, a low seeding density allows that corresponding particle images can be allocated unambiguously in two consecutive images to determine their displacement.

A simple algorithm with which the in-plane displacement of particle images in two consecutive images can be calculated is the nearest neighbor approach. Here, the Euclidean distance between a particle in the first frame and all particle images in the second frame of a double-frame image are calculated. Thus, the particle image that is located closest to the investigated particle image of the first frame is considered to calculate the particle image displacement. More sophisticated particle tracking approaches that e.g. also take the particle image trajectory into account are investigated by Ouellette et al. (2006) or Schanz et al. (2016).

To reconstruct three-dimensional particle image displacements, astigmatic particle images are created in this work as also performed by Cierpka et al. (2010) and Cierpka et al. (2011). This is realized by inserting a cylindrical lens in front of the utilized camera system. This introduces the astigmatism effect, which leads to elliptical particle images. In combination with a proper calibration that associates the particle image characteristics with a definite out-of-plane position of a particle, this allows to determine the particle position perpendicular to the measurement plane. The astigmatism is characterized by the presence of two focal planes FP1 and FP2, which are spatially separated. This results in particle images, whose shape is rather circular approximately midway between these focal planes. It shall be noted that the particle is defocused at this location. Near the two focal planes, the particle image exhibits either a vertically or a horizontally aligned elliptic shape. In Figure 2.2 the characteristic path of the fluorescence signal of a particle that is aberrated by a cylindrical lens inside a microscope is shown.

The light that is emitted by the particle is first parallelized by an infinity corrected objective lens. Then, the parallelized beam passes a focusing and a cylindrical lens. Due to the presence of the cylindrical lens, the refracted light focuses on two spatially separated, perpendicularly aligned focal planes FP_1 and FP_2. This leads to an elliptical image shape, as shown in Figure 2.2.

To reconstruct the out-of-plane position of a particle from its aberrated image, an in situ calibration has to be performed before each measurement. For this, images of sedimented particles are recorded in a scanning procedure. Then, each particle image is auto-correlated. The resulting auto-correlation peaks are intersected at a certain height $R/R_{\max}$. The major and minor axis lengths of the intersected auto-correlation peak is a measure for the out-of-plane position of a particle (Cierpka et al., 2011; Rossi and Kähler, 2014). Exemplary auto-correlation maps for polystyrene particles of $d_\mathrm{p} = 3.55\,\mu\mathrm{m}$ diameter are given in Figures 2.3(a) to (c). Here, particles are located $\delta_\mathrm{z} = 40\,\mu\mathrm{m}$, $\delta_\mathrm{z} = 0\,\mu\mathrm{m}$ and $\delta_\mathrm{z} = -40\,\mu\mathrm{m}$, respectively,

from the zero position. This zero position is defined as the position where the ratio of the major and minor axis length is closest to unity, i.e. $a_x/a_y \approx 1$. In Figures 2.3(a) to (c), the axis lengths in x- and y-direction a_x and a_y are shown for an intersection of the auto-correlation peaks at $R/R_{max} = 0.2$. The calibration curve that results from the previously described evaluation of the auto-correlation peaks at each stage of the scanning procedure is shown in Figure 2.3(d). Here, the color coding indicates the position of the particle along the z-axis, i.e. the out-of-plane position relatively to the zero position. Black dots indicate the data points that result from the evaluation of the auto-correlation maps that are shown in Figures 2.3(a) to (c).

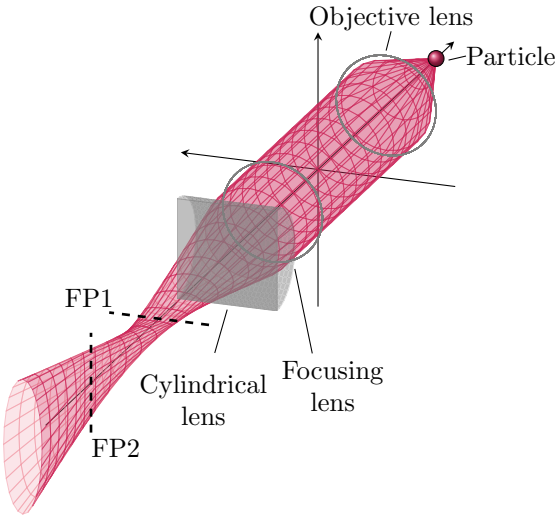

Figure 2.2.: Light path of a fluorescent particle through a microscope with implemented cylindrical lens causing aberration that results in two spatially separated and perpendicularly aligned focal planes, leading to elliptical particle images.

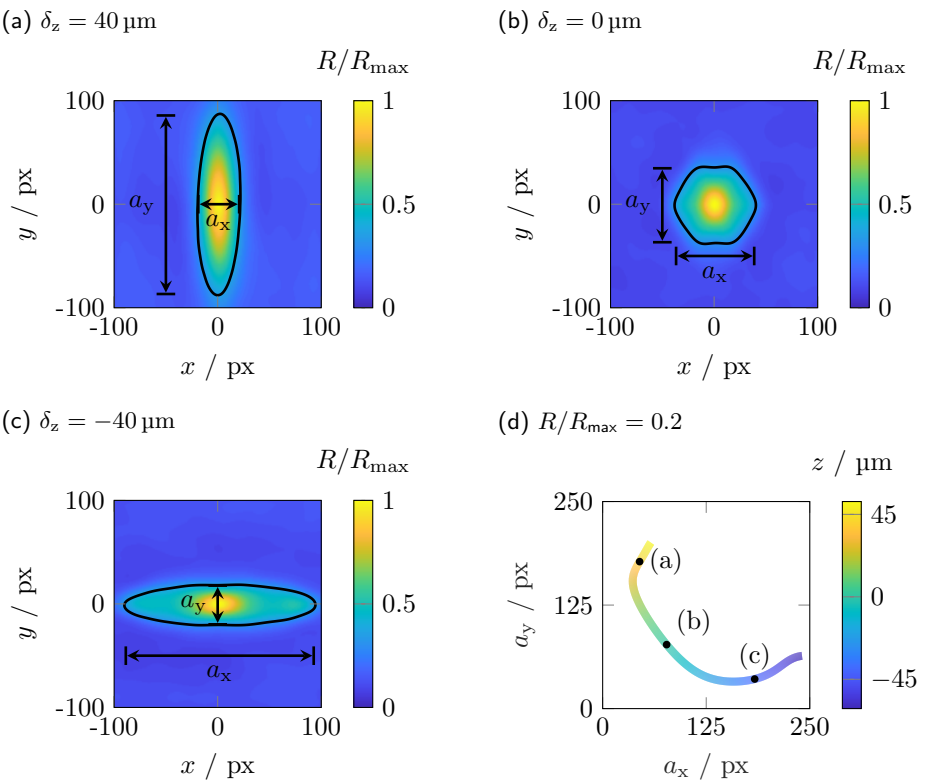

Figure 2.3.: Sample auto-correlation maps of a polystyrene particle with 3.55 µm diameter at an out-of-plane position of (a) $\delta_z = 40\,\mu m$, (b) $\delta_z = 0\,\mu m$ and (c) $\delta_z = -40\,\mu m$. (d) Resulting calibration curve, whereas the axis lengths a_x and a_y of the auto-correlation peaks are measured at $R/R_{max} = 0.2$. Black markers refer to the auto-correlation results that are shown in Figures 2.3(a) to (c).

2.2.2. Micro Particle Image Velocimetry[2]

If optical accessibility is granted, PIV is an established method for non-invasive flow measurements. It can be applied to any type of particle seeded flow to trace the fluid motion, provided that particles behave as ideal fluid tracers. Usually in PIV measurements, tracer particles are chosen such that they follow the liquid phase slip free, i.e. Stokes number $St \ll 1$. This guarantees that measured tracer particle velocities are representative for the liquid phase velocity field.

[2]Parts of this chapter are published in Blahout et al. (2021), used under CC BY 4.0. The original contents have been edited and/or extended for this work.

However, if the Stokes number or the particle size compared to the characteristic channel dimensions is large, a significant slip velocity between suspended particles and the carrier fluid may occur. Thus, the particle velocities are not representative for the liquid phase flow field. Instead, particle velocities can be used to measure the bulk dynamics of particles themselves. In chapter 7, it is demonstrated that the simultaneous usage of both, small tracer particles and large suspension particles allows the measurement of liquid phase velocities as well as suspension particle velocities from the same set of recordings, i.e. at the same time.
PIV is commonly applied to situations of high particle seeding density. It is suitable to measure transient flow fields, also in combination with other optical measurement techniques (Skarman et al., 1996; Funatani et al., 2004; Kordel et al., 2016). In classical PIV applications, fluid tracers should have a small image diameter of only a few pixels (Willert, 1996; Westerweel, 1997). Without astigmatism effects their intensity profile will be typically Gaussian (Adrian, 1991; Willert and Gharib, 1991).
The accuracy and reliability of PIV measurements for such Gaussian particle images is a function of various parameters, such as the amount of particles per interrogation window, the particle image density, the particle image diameter, the signal to noise ratio, out-of-plane as well as in-plane loss-of-pairs and velocity gradients (Adrian, 1991; Willert, 1996; Westerweel, 1997).
A measure for the accuracy of a cross-correlation result is the displacement estimation error. It is known to minimize for particle image diameters of $d_{\mathrm{p,I}} = 2 - 3\,\mathrm{px}$, while it grows for larger diameters due to random errors (Westerweel, 1997). While PIV is typically used to quantify flow fields, it is applicable to any kind of displacement field as long as the particle image shape and particle group formation do not change significantly between correlated frames.
A measure for the reliability of PIV measurements is the detectability, which is the ratio of the highest to the second highest correlation peak value. It can be understood as the probability that the highest correlation peak corresponds to the real particle image displacement (Adrian, 1991).
Particle images are recorded in two consecutive frames using a preset inter-framing time Δ. Depending on the velocities that occur in the investigated flow, the inter-framing time can vary to adhere basic experimental design rules such as the one-quarter rule (Keane and Adrian, 1990; Raffel et al., 2018).
To investigate flows in microfluidic devices, optical systems such as epifluorescence microscopes are utilized. In contrast to classical PIV set-ups where single planes are observed, in µPIV set-ups a volume of the test section is illuminated that is large compared to the focal depth of the microscope optics, i.e. the objective lens. To avoid noise signals such as wall reflections, fluorescence filter systems and fluorescent particles are utilized. These are designed such that only the particle fluorescence signal reaches the camera. Due to the volume illumination, light of both, focused as well as defocused particles, reaches the camera. Thus, an in-plane measurement result can be biased due to the presence of defocused particle

images in a measurement if a significant out-of-plane velocity gradient is present. A measure for the contribution of defocused particles to the in-plane measurement result is the depth of correlation δ_{DoC}, i.e. the effective measurement volume. It can be calculated as (Olsen and Adrian, 2000; Bourdon et al., 2006):

$$\delta_{\mathrm{DoC}} = 2\left(\frac{1-\sqrt{C_{\mathrm{DoC}}}}{\sqrt{C_{\mathrm{DoC}}}}\left[\frac{n^2 d_{\mathrm{p}}^2}{4\mathrm{NA}^2}+\frac{5.95\,(M+1)^2\,\lambda^2 n^4}{16M^2\mathrm{NA}^4}\right]\right)^{0.5} \tag{2.16}$$

Here, C_{DoC} is a weighting factor that considers the range in which particle images contribute to the correlation result and that is usually set to $C_{\mathrm{DoC}} = 0.01$. Furthermore, n denotes the refractive index of the lens immersion fluid, NA and M denote the numerical aperture and the magnification of the objective lens, respectively and λ is the wavelength of the light that is used for illumination.
Recorded measurement images are sub-divided into interrogation windows. Then, a cross-correlation algorithm is applied to determine the particle image displacement and, as the inter-framing time is known, the fluid velocity. Consequently, the number of interrogation windows into which an image is divided determines the spatial resolution of a measurement. A rule of thumb that is commonly used in PIV is that at least five particle images have to be located inside an interrogation window to exceed a detection probability of 95% (Keane and Adrian, 1992; Raffel et al., 2018; Adrian and Westerweel, 2011). Thus, typical particle image densities for PIV measurements are in the order of magnitude of $N_{\mathrm{ppp}} = \mathcal{O}\left(10^{-2}\right)$. Due to the volume illumination that is utilized in µPIV, an increased concentration of tracer particles leads also to an increased background noise that results from defocused particles. Thus, an amount of five particle images per interrogation window may be difficult to realize in combination with a high spatial resolution. As microfluidic flows are usually stationary, i.e. temporal velocity fluctuations are not present, due to low flow rates, the spatial resolution in µPIV can be increased by utilizing ensemble correlation algorithms (Santiago et al., 1998). These determine particle displacements inside each interrogation window from temporal averages that are calculated at the correlation plane (Meinhart et al., 2000).
A mathematical description of the cross-correlation of single exposed double-frame images follows in section 2.2.2.1. Afterwards, methods to estimate the uncertainty of a PIV measurement are discussed in section 2.2.2.2.

2.2.2.1. Cross-correlation of single exposed images

Two single exposed images $I_1(\boldsymbol{X}_{\mathrm{p,I,1}})$ and $I_2(\boldsymbol{X}_{\mathrm{p,I,2}})$ recorded at times t_0 and $t_0+\Delta$ are considered, where $\boldsymbol{X}_{\mathrm{p,I,i}}$ generally contains the center positions of all particle images in image i. If particle images are displaced during the time interval Δ by a separation vector $\boldsymbol{s}_{\mathrm{p,I}}$, then it follows that $\boldsymbol{X}_{\mathrm{p,I,2}} = \boldsymbol{X}_{\mathrm{p,I,1}} + \boldsymbol{s}_{\mathrm{p,I}}$ and the cross-correlation function $R(\boldsymbol{s}_{\mathrm{p,I}})$ of the two images $I_1(\boldsymbol{X}_{\mathrm{p,I,1}})$ and $I_2(\boldsymbol{X}_{\mathrm{p,I,2}})$ can

be defined as (Keane and Adrian, 1992):

$$R(\boldsymbol{s}_{\mathrm{p,I}}) = \int_{A_{\mathrm{IW}}} I_1(\boldsymbol{X}_{\mathrm{p,I,1}}) I_2(\boldsymbol{X}_{\mathrm{p,I,1}} + \boldsymbol{s}_{\mathrm{p,I}})\, d\boldsymbol{X}_{\mathrm{p,I}} \tag{2.17}$$

Here, A_{IW} denotes the interrogation area. The separation vector $\boldsymbol{s}_{\mathrm{p,I}}$ can be also interpreted as the vector by which the second image $I_2(\boldsymbol{X}_{\mathrm{p,I,2}})$ has to be shifted to match the particle positions of the first image, i.e. $\boldsymbol{s}_{\mathrm{p,I}} = -\left(\boldsymbol{X}_{\mathrm{p,I,2}} - \boldsymbol{X}_{\mathrm{p,I,1}}\right) = -\delta\boldsymbol{X}_{\mathrm{p,I}}$. According to Keane and Adrian (1992) the estimator for the cross-correlation can be decomposed into three characteristic parts for single exposed double-frame images:

$$R(\boldsymbol{s}_{\mathrm{p,I}}) = R_{\mathrm{C}}(\boldsymbol{s}_{\mathrm{p,I}}) + R_{\mathrm{D}}(\boldsymbol{s}_{\mathrm{p,I}}) + R_{\mathrm{F}}(\boldsymbol{s}_{\mathrm{p,I}}) \tag{2.18}$$

$R_{\mathrm{C}}(\boldsymbol{s}_{\mathrm{p,I}})$ and $R_{\mathrm{F}}(\boldsymbol{s}_{\mathrm{p,I}})$ contain the convolution of the mean intensities and the fluctuating noise of $I_1(\boldsymbol{X}_{\mathrm{p,I,1}})$ and $I_2(\boldsymbol{X}_{\mathrm{p,I,2}})$, respectively. $R_{\mathrm{D}}(\boldsymbol{s}_{\mathrm{p,I}})$ results from the relative displacement of particle images between $I_1(\boldsymbol{X}_{\mathrm{p,I,1}})$ and $I_2(\boldsymbol{X}_{\mathrm{p,I,2}})$ and is hence on referred to as displacement correlation peak. Thus, the location of the displacement correlation peak in the correlation plane corresponds to the particle image displacement inside an interrogation window. As shown by Willert and Gharib (1991), $R_{\mathrm{D}}(\boldsymbol{s}_{\mathrm{p,I}})$ has a Gaussian peak shape for particle images with a Gaussian intensity distribution. Therefore, a Gaussian peak fit estimator $\hat{\epsilon}_{\mathrm{G}}$ can be used to interpolate the center position of $R_{\mathrm{D}}(\boldsymbol{s})$ from discrete correlation values. With this, peak-locking effects can be reduced and the detection accuracy of the center position of the displacement correlation peak can be extended to sub-pixel range (Willert and Gharib, 1991). The Gaussian peak fit estimator reads (Westerweel, 1997):

$$\hat{\epsilon}_{\mathrm{G}} = \frac{\ln\left(R_{\text{max-1}}\right) - \ln\left(R_{\text{max+1}}\right)}{2\left[\ln\left(R_{\text{max-1}}\right) + \ln\left(R_{\text{max+1}}\right) - 2\ln\left(R_{\text{max}}\right)\right]} \tag{2.19}$$

Here, $R_{\mathrm{max}} = R_{\mathrm{D}}(\delta\boldsymbol{X}_{\mathrm{p,I}})$ and $R_{\mathrm{max}\pm1} = R_{\mathrm{D}}(\delta\boldsymbol{X}_{\mathrm{p,I}} \pm 1)$. Measures for the probability that the displacement correlation peak corresponds to the real particle image displacement and the accuracy with which the displacement correlation peak position is determined are the detectability D and the displacement estimation error ϵ_{D}. Both quantities are discussed in the following.

Detectability The detectability is a measure for the reliability of a cross-correlation result. It is defined as the ratio of the correlation peak values between the highest and the second highest correlation peak of a correlation function $R(\boldsymbol{s}_{\mathrm{p,I}})$ (Coupland and Pickering, 1988; Keane and Adrian, 1990; Adrian and Westerweel, 2011):

$$D = \frac{R_{\mathrm{max,1}}}{R_{\mathrm{max,2}}} \tag{2.20}$$

Displacement estimation error The displacement estimation error can be expressed as the variance of its corresponding peak fit estimator. For a Gaussian peak fit estimator it can be described as (Westerweel, 1997):

$$\epsilon_{\mathrm{D}} = \mathrm{var}\left\{\hat{\epsilon}_{\mathrm{G}}\right\} \approx \sum_{i=-1}^{+1}\sum_{j=-1}^{+1} \frac{\partial\hat{\epsilon}_{\mathrm{G}}}{\partial R_{\mathrm{max+i}}}\frac{\partial\hat{\epsilon}_{\mathrm{G}}}{\partial R_{\mathrm{max+j}}} \cdot \mathrm{cov}\left\{R_{\mathrm{max+i}}, R_{\mathrm{max+j}}\right\} \tag{2.21}$$

In case of a non-fractional displacement, (2.21) simplifies to:

$$\tilde{\epsilon}_{\mathrm{D}} = \underbrace{\left(\frac{\partial\hat{\epsilon}_{G}}{\partial R_{\mathrm{max}\pm1}}\right)^{2}}_{\tilde{\epsilon}_{\mathrm{D},1}} \underbrace{\left[\mathrm{var}\left\{R_{\mathrm{max\text{-}1}}\right\} + \mathrm{var}\left\{R_{\mathrm{max+1}}\right\} - 2\mathrm{cov}\left\{R_{\mathrm{max\text{-}1}}, R_{\mathrm{max+1}}\right\}\right]}_{\tilde{\epsilon}_{\mathrm{D},2}} \tag{2.22}$$

with:

$$\tilde{\epsilon}_{\mathrm{D},1} = \left(\frac{4\cdot\left[\ln(R_{\mathrm{max}\mp1}) - \ln(R_{\mathrm{max}})\right]}{R_{\mathrm{max}\pm1}\left[2\cdot\ln(R_{\mathrm{max}\pm1}) - 4\ln(R_{\mathrm{max}}) + 2\cdot\ln(R_{\mathrm{max}\mp1})\right]^{2}}\right)^{2} \tag{2.23}$$

Both terms $\tilde{\epsilon}_{\mathrm{D},1}$ and $\tilde{\epsilon}_{\mathrm{D},2}$ represent different properties of the displacement correlation peak. The first term $\tilde{\epsilon}_{\mathrm{D},1}$ is the squared derivative of the Gaussian peak fit estimator $\hat{\epsilon}_{\mathrm{G}}$ given in (2.19). If the correlation peak flattens out, i.e. $R_{\mathrm{max}\pm1} \to R_{\mathrm{max}}$, the denominator of (2.23) approaches zero sooner than the nominator and $\tilde{\epsilon}_{\mathrm{D},1}$, and therefore $\tilde{\epsilon}_{\mathrm{D}}$, goes towards infinity. The second term $\tilde{\epsilon}_{\mathrm{D},2}$ is a measure of (i) the spread of the normalized correlation peak slope i.e. its width as well as (ii) the spread of the correlation peak symmetry of an ensemble. For an ensemble with only perfectly symmetric correlation peaks, i.e. $R_{\mathrm{max+1}} = R_{\mathrm{max\text{-}1}}$, the second term and (2.22), respectively, will approach zero for a finite correlation peak width.

2.2.2.2. Uncertainty estimation of PIV measurements

Results from PIV measurements, can be biased by systematic and random errors. Several methods to account for these errors or, more specifically, to estimate the uncertainty of a PIV measurement result, have been developed over the last decades. Comprehensive overviews of these approaches can be found in Sciacchitano et al. (2015) and Sciacchitano (2019). Generally, the methods can be categorized into statistical as well as, according to Sciacchitano (2019), direct and indirect methods. Statistical approaches calculate the deviation of a flow quantity from its time or spatial average to determine the measurement uncertainty (Sciacchitano and Wieneke, 2016). With this, e.g. the uncertainty of mean flow quantities or flow fluctuations can be estimated.
Direct uncertainty quantification approaches are the particle disparity (Sciacchitano et al., 2013) or the correlation statistics (Wieneke, 2015) approach. Both methods

use the displacement field of a PIV evaluation to remove the image shift between two corresponding frames. As measurement errors result in mismatches between such frames, either the contribution of individual particle images or individual pixels inside an interrogation window to the displacement correlation peak, are used to calculate the measurement uncertainty. Other examples for direct methods are the moment of correlation plane (Bhattacharya et al., 2018) and the error sampling approach (Smith and Oberkampf, 2014). The moment of correlation plane approach calculates the standard uncertainty from the second moment of the generalized cross-correlation that is convolved with a two-dimensional Gaussian fit function. The error sampling approach suggests to repeat an experiment several times while systematically varying different aspects of the experiment that affect the measurement error to receive an accurate estimate of the overall error.
Indirect methods are the uncertainty surface approach (Timmins et al., 2012) and the correlation signal to noise ratio metrics (Charonko and Vlachos, 2013; Xue et al., 2014) approach. The uncertainty surface approach utilizes synthetic data that are representative for the corresponding measurement situation to determine an uncertainty surface, from which the resulting measurement uncertainty is calculated. In contrast to this, the correlation SNR metrics approach uses an empirical equation of the form

$$U_\mathrm{i} = \sqrt{\left(C_1 \cdot \exp\left(-0.5\left(\frac{\mathrm{SNR_R} - C_2}{C_3}\right)^2\right)\right)^2 + \left(C_4 \cdot \mathrm{SNR_R}^{-C_5}\right)^2 + C_6^2} \quad (2.24)$$

to calculate the measurement uncertainty U_i at the lower limit (LL) and the upper limit (UL) of the 68.5% and 95% confidence intervals from differently defined signal to noise ratios of the correlation plane $\mathrm{SNR_R}$. In (2.24), C_1 to C_6 are fitting coefficients that are dependent on the used correlation signal to noise ratio metric and the confidence interval level. Applying this, Xue et al. (2014) showed that the error magnitude of PIV data is not necessarily normally distributed. In the present work, the correlation map entropy is utilized as signal to noise ratio metrics for an uncertainty estimation (see section 7.2). To calculate the correlation map entropy, first, a histogram with 30 bins is calculated from the correlation map of an interrogation window. From this, the probability P_j that a correlation value can be found within a certain bin is calculated (Xue et al., 2014). Then, the correlation map entropy can be determined as follows:

$$\mathrm{SNR_R} = \left(\sum_{\mathrm{j}=1}^{30} P_\mathrm{j} \cdot \log_2\left(\frac{1}{P_\mathrm{j}}\right)\right)^{-1} \quad (2.25)$$

Fitting coefficients C_1 to C_6 used in (2.24) are provided in Table 2.1 for the lower and upper limit of the 68.5% and 95% confidence interval (Xue et al., 2014).

Table 2.1.: Fitting coefficients to calculate the measurement uncertainty based on the correlation map entropy (Xue et al., 2014).

	$U_{\mathrm{LL},68.5}$	$U_{\mathrm{UL},68.5}$	$U_{\mathrm{LL},95}$	$U_{\mathrm{UL},95}$
C_1	0.05352	0.2739	0.02047	1.757
C_2	0	0	0	0
C_3	3.188	3.076	3.063	3.056
C_4	0.02148	5.527	0.05605	14.7
C_5	-12.25	-11.59	-13.41	-7.985
C_6	0	0	0.001905	0.1407

3. Materials and methods

Possibilities for a multi-dimensional fractionation inside a sharp-corner serpentine microchannel are explored experimentally and numerically in this thesis. Experimental investigations are performed with a micro Particle Image Velocimetry set-up that can be extended to perform Astigmatism Particle Tracking Velocimetry measurements. A description of the experimental set-up as well as relevant technical specifications of the individual components are provided in section 3.1.
For investigations on the bulk dynamics of suspensions, the velocity fields of both, the liquid and the particulate phase have to be known. The present thesis provides an approach to determine both of these velocity fields simultaneously. This approach is applied to a suspension flow inside a straight microchannel with trapezoidal cross-section. Both, the straight microchannel as well as the sharp-corner serpentine microchannel are introduced in section 3.2. Here, also specifications of particles that are either used as tracers or as particulate phase of a suspension are provided.
To determine parameters at which multi-dimensional fractionation is promising, long-exposure measurements are performed inside the sharp-corner serpentine microchannel. The experimental procedure as well as the evaluation procedure of recorded images are described in section 3.3.
A detailed investigation of the three-dimensional distributions of microparticles inside the sharp-corner microchannel is performed by means of Astigmatism Particle Tracking Velocimetry. Details on the experimental set-up as well as on the calibration procedure and the experimental execution are given in section 3.4.
The forces that are responsible for the motion of individual particles inside a sharp-corner serpentine microchannel flow are analyzed based on numerical simulations. The numerical set-ups that are used for these simulations are described in section 3.5. Here, relevant details on the calculation of individual force contributions are provided as well. Additionally, the experimental procedure that is utilized to measure reference flow fields is described.
A new extension of the micro Particle Image Velocimetry utilizes particles with ring-shaped images to determine flow fields of both phases of a suspension. The accuracy and reliability of such particle images are compared to other particle image shapes based on synthetically generated images. The procedure for the synthetic image generation is described in section 3.6. As the developed approach is also applied to a real measurement situation, a description of relevant experimental parameters is provided here, as well.

3.1. Experimental set-up

Core of the experimental set-up is an epifluorescent microscope (Nikon Eclipse LV100) with an infinity-corrected objective lens (20X Nikon CFI60 TU Plan Epi ELWD). The objective lens has a magnification of $M = 20$ and a numerical aperture of NA $= 0.4$. For illumination, the beam of a double-pulsed Nd:YAG-laser either of type Litron Nano S 65-15 PIV or NewWave SOLO PIV III is coupled into the microscope. Long-exposure recordings of up to 1 s are illuminated by a 100 W white light halogen lamp (Nikon D-LH). Images are recorded by a double-frame CCD camera either of type LaVision Imager pro SX or LaVision Imager SX 6M. The individual camera resolutions and the field of views that are obtained in combination with the previously described objective lens are provided in Table 3.1.

Table 3.1.: Recording properties.

Camera type	Resolution / px	FOV / mm
Imager pro SX	2456×2058	0.57×0.48
Imager SX 6M	2752×2200	0.89×0.71

For Astigmatism Particle Tracking Velocimetry (APTV) measurements, a cylindrical lens with a focal length of $f = 200$ mm is positioned in front of the CCD camera. Image acquisition and evaluation is performed by the commercial DaVis software (LaVision GmbH, Germany). The feed flow is generated by a syringe pump of type HLL LA-800. The experimental set-up with the installed NewWave laser and Imager SX 6M camera is shown in Figure 3.1(a).
A chip holder (Micronit Fluidic Connect Pro) connects the inlet and outlet pipes with microfluidic chips. A close-up of the assembled chip holder including a microfluidic chip and the pipe connections is shown in Figure 3.1(b). Figure 3.1(c) shows a close-up of a microfluidic chip prototype that contains also the serpentine microchannel geometry that is used in the present thesis.

(a) Overview

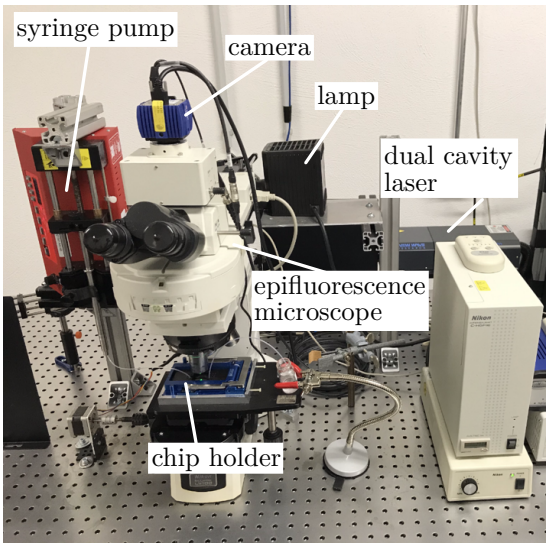

(b) Detail chip holder

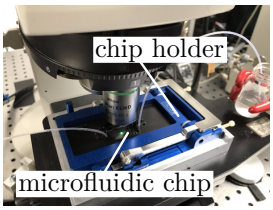

(c) Detail chip

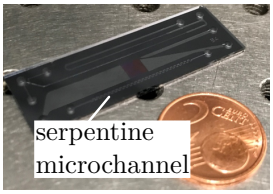

Figure 3.1.: (a) Overview of the experimental set-up (with the installed NewWave laser and the Imager SX 6M camera, the cylindrical lens is not assembled); (b) close-up of the microfluidic chip holder; (c) close-up of a microfluidic chip prototype.

3.2. Materials

Relevant materials that are used in the present thesis are described in this section. Microchannel geometries that are the basis for experimental studies are described in section 3.2.1. An overview of the properties of utilized particles is provided in section 3.2.2.

3.2.1. Microchannel geometries

For the experimental studies of the present work, two different microchannel geometries are used. These are a straight microchannel with trapezoidal cross-section and a sharp-corner serpentine microchannel with rectangular cross-section. Both microchannels are fabricated by Micronit GmbH, Germany. Schematics of the straight trapezoidal and the sharp-corner serpentine microchannel are shown in Figures 3.2(a) and (b), respectively.

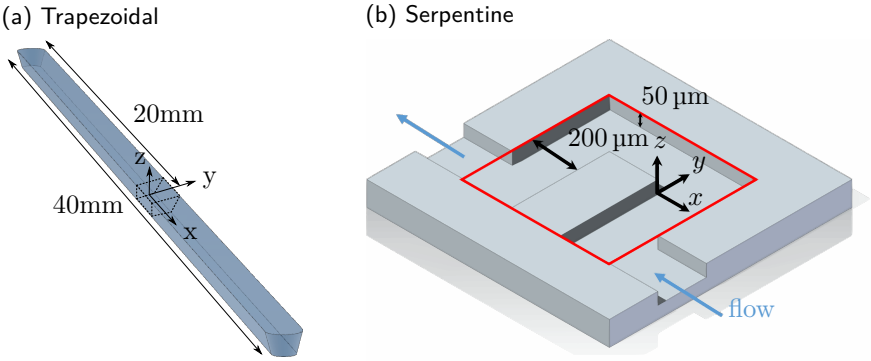

Figure 3.2.: (a) Schematic figure of the straight microchannel with trapezoidal cross-section. The region of interest is indicated by black dashed lines; (b) Schematic figure of the sharp-corner serpentine channel. The region of interest is indicated by a red rectangle.

The straight microchannel (Figure 3.2(a)) has a height of $H \approx 580\,\mu m$ and a top and bottom width of $W_{top} \approx 578\,\mu m$ and $W_{bottom} \approx 321\,\mu m$, respectively. The inclination of the microchannel sidewalls is a result of the fabrication process. This microchannel is used for the measurements of suspension bulk dynamics by means of µPIV utilizing ring-shaped particle images (chapter 7).
The sharp-corner serpentine microchannel (Figure 3.2(b)) has a height of $H = 50\,\mu m$ and a width of $W = 200\,\mu m$. Before the first and after the last serpentine loop, there is a straight inlet and outlet section of 10 mm length with equal cross-sectional dimensions. The serpentine microchannel is utilized to investigate the focusing

behavior of micron and sub-micron particles as well as the fractionation performance of micron particles (see chapters 4 and 5). This microchannel geometry is also used as a basis for the numerical investigations that are discussed in chapter 6.

3.2.2. Particles

The role of particles in the present work is twofold: they are used either as tracers or as the particulate phase of a suspension. In the first case, it is assumed that particles follow the carrier liquid flow slip-free and can therefore be used to determine liquid flow velocity fields. In the latter case, the suspension particle bulk behavior might differ from that of the carrier liquid. In this case, the suspension particle bulk behavior itself or the hydrodynamical interactions between liquid and particulate phase are the subject of study.
An overview of the particles that are used in the present thesis as tracers as well as particulate phase of a suspension is given in Table 3.2. The relevant particle properties, specifically the particle material, the diameter d_p and the density ρ_p are assigned to a unique particle label and a unique representation style that are used throughout this thesis. All particles are fluorescently labelled for optical detection with the epifluorescence microscope.

Table 3.2.: Particle properties.

Label	Material	d_p / µm	ρ_p / kg m^{-3}	Style	Producer
Gauss	polymethyl methacrylat	60 ± 3	1200	△	Microbeads AS
MF-3	melamine resin	3.34 ± 0.08	1510	△	microParticles GmbH
MF-10	melamine resin	9.84 ± 0.26	1510	▽	microParticles GmbH
OPF	polystyrene	1.19 ± 0.03	1050	×	microParticles GmbH
Plateau	polymethyl methacrylat	60 ± 3	1200	□	Microbeads AS
PS-0.45	polystyrene	0.450 ± 0.009	1050	▼	microParticles GmbH
PS-0.60	polystyrene	0.600 ± 0.018	1050	▲	Thermo Fisher Scientific
PS-0.71	polystyrene	0.710 ± 0.021	1050	♦	Thermo Fisher Scientific
PS-0.79	polystyrene	0.790 ± 0.024	1050	●	Thermo Fisher Scientific
PS-0.86	polystyrene	0.860 ± 0.026	1050	■	Thermo Fisher Scientific
PS-3	polystyrene	3.55 ± 0.07	1050	○	microParticles GmbH
PS-10	polystyrene	9.89 ± 0.10	1050	□	microParticles GmbH
Ring, SP	polymethyl methacrylat	60 ± 3	1200	○	Microbeads AS
SCL	polystyrene	1.19 ± 0.03	1050	+	microParticles GmbH
SiO_2-3	silica	3.59 ± 0.21	1850	◊	microParticles GmbH
SiO_2-10	silica	9.92 ± 0.28	1850	⬠	microParticles GmbH

3.3. Long-exposure fluorescence microscopy

Long-exposure fluorescence microscopy is conducted to identify parameters at which multi-dimensional fractionation inside a sharp-corner microchannel is promising. The experimental procedure that is utilized for this is provided in section 3.3.1. The procedure with which acquired particle streak intensity images are evaluated is described in section 3.3.2.

3.3.1. Experimental procedure

The particle focusing behavior of different particle groups is investigated utilizing the experimental set-up as described in section 3.1. The properties of particle streaks are determined by means of long-exposure measurements with an exposure time of 1 s. A white light halogen lamp is used for illumination. Images are recorded by the Imager SX 6M CCD camera. The suspension flow is generated by a stainless steel syringe that is driven by the syringe pump.
Particle streaks are recorded at six different measurement locations of the serpentine microchannel, which are depicted in Figure 3.3 as red rectangles. The numbers denote the downstream measurement locations counting full serpentine loops.

Figure 3.3.: Schematic of the sharp corner serpentine microchannel indicating the measurement locations at which particle streaks are investigated by red rectangles.

Streaks for micron ($d_p > 1\,\mu m$) and sub-micron ($d_p < 1\,\mu m$) particles are evaluated. In case of micron particles, polystyrene (PS-3, PS-10), melamine (MF-3, MF-10) and silica (SiO_2-3, SiO_2-10) particles are used. In case of sub-micron particles, polystyrene particles with diameters between $0.45\,\mu m \leq d_p \leq 0.86\,\mu m$ are utilized. Detailed information on the particle properties are listed in Table 3.2. All particle groups are measured separately.
Each particle group is suspended in a carrier liquid that consists of distilled water and the surfactant Pluronic F-127 (Sigma-Aldrich). In case of micron particles, a solution with 1 weight-% F-127 and a nominal particle volume concentration of $\varphi = 0.0005$ is used. In case of sub-micron particles, a solution with 0.1 weight-% F-127 and a nominal particle volume concentration of $\varphi = 0.0004$ is used. The addition of the surfactant prevents particles from clustering and sticking to the peripherals as well as to the microchannel walls. The addition of the surfactant has an influence on the viscosity of the carrier liquid. Therefore, the dynamic viscosity η and the density ρ of the carrier liquids are determined with a rheometer (Brookfield DV-III Ultra) and a pycnometer, respectively. Five independent probes of both

carrier liquids are measured at five different rotational speeds. As a reference, also the viscosity of five independent probes of distilled water at a single rotational speed and the density is measured. The kinematic viscosity ν is calculated from both measured quantities as $\nu = \eta/\rho$. Resulting dynamic viscosities as well as densities and kinematic viscosities are provided in Table 3.3.

Table 3.3.: Carrier liquid properties.

	H_20	H_20 + 0.1w.-% F-127	H_20 + 1w.-% F-127
η / Pa s	$(1.048\pm0.017)\times10^{-3}$	$(1.054\pm0.009)\times10^{-3}$	$(1.267\pm0.028)\times10^{-3}$
ρ / kg m^{-3}	995.63±0.35	994.64±0.58	996.42±0.97
ν / m^2 s^{-1}	$(1.053\pm0.017)\times10^{-6}$	$(1.058\pm0.009)\times10^{-6}$	$(1.265\pm0.028)\times10^{-6}$

Measurements of micron particles are performed at volume flow rates of $0.25\,\mathrm{mL\,min^{-1}} \leq Q \leq 1.20\,\mathrm{mL\,min^{-1}}$ with steps of $0.05\,\mathrm{mL\,min^{-1}}$. Corresponding bulk Reynolds numbers are calculated as $\mathrm{Re_b} = (u_\mathrm{b} \cdot d_\mathrm{h})/\nu$, using the bulk flow velocity $u_\mathrm{b} = Q/(W \cdot H)$ and the hydraulic diameter $d_\mathrm{h} = (4WH)/(2(W+H))$. Sub-micron particles are measured at volume flow rates of up to $Q = 1.40\,\mathrm{mL\,min^{-1}}$. Thus, the highest considered bulk Reynolds number is $\mathrm{Re_b} = 177$.

3.3.2. Evaluation procedure

This section describes the procedure with which experimental data of long-exposure measurements are processed (section 3.3.2.1) and subsequent particle streak evaluation is carried out (section 3.3.2.2).

3.3.2.1. Image pre-processing

Before particle streaks are evaluated, a pre-processing procedure is applied to all recorded images to enhance the signal to noise ratio (SNR) of particle streaks. This is performed in the commercial software DaVis 10 (LaVision GmbH, Germany). For polystyrene and melamine particles, a sliding average filter with Gaussian weight and 3 px filter length is applied in the first step. In the second step, a background image is calculated from the minimum intensity values in a 200 px × 200 px environment of each pixel and then subtracted from the corresponding image. A sample raw image of PS-3 particles at $\mathrm{Re_b} = 26$ inside the 25th serpentine loop is shown in Figure 3.4(a). The same image after application of the described pre-processing procedure is shown in Figure 3.4(b). Here, the signal to noise ratio could be enhanced by 40 times for the pre-processed image.
As the fluorescence signal of silica particles is weaker than for polystyrene and melamine particles due to different fluorescence properties, the pre-processing procedure that is applied on images containing silica particles is modified. Specifically, additional to ten measurement images that capture particle streak intensities, ten

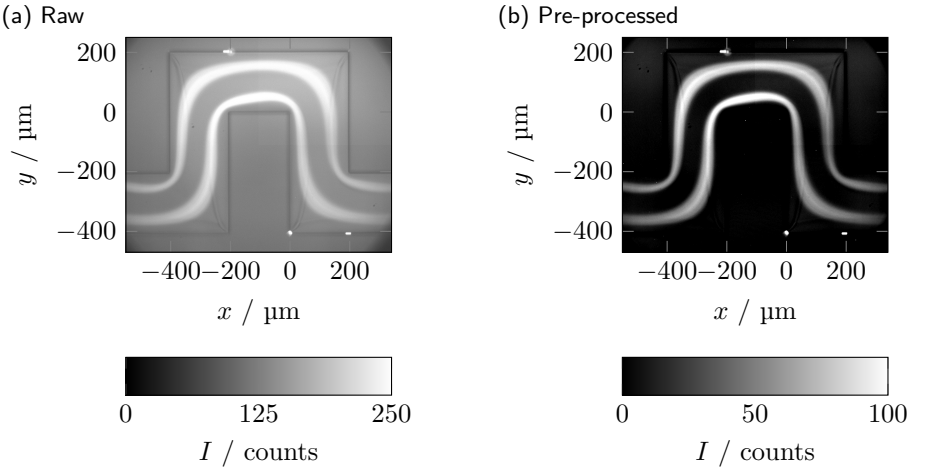

Figure 3.4.: Sample raw (a) and pre-processed (b) image of PS-3 particles at $\mathrm{Re_b} = 26$ in the 25th serpentine loop. Flow direction is from right to left.

independent reference images using pure carrier liquid are recorded. On both, reference and measurement images, a sliding average filter with Gaussian weight and 3 px length is applied. Afterwards, a minimum background image is calculated from reference images. In contrast to this, a maximum intensity image is determined from measurement images to enhance the particle signal strength. In the end, the background image is subtracted from the processed measurement image and an additional sliding average filter with Gaussian profile and 3 px length is applied.

3.3.2.2. Streak evaluation

From pre-processed measurement images (see section 3.3.2.1) intensity profiles along the microchannel cross-section are evaluated at different locations using an in-house Matlab code. The locations at which intensity profiles are extracted are indicated by arrows in Figure 3.5(a).
In a first step, intensity gradients that may result from reflections at the microchannel side walls are corrected. Afterwards, extracted intensity profiles are sampled by a low-pass frequency filter using a rectangular filter window in the frequency domain. The corrected and sampled intensity profile extracted from data at the location that is indicated by the red arrow, i.e. at $x = -100\,\mu\mathrm{m}$, in Figure 3.5(a) is shown in Figure 3.5(b). The variable x' is the coordinate that points from the inner towards the outer microchannel wall and is normalized by the microchannel width $W = 200\,\mu\mathrm{m}$. Thus, generally $x'/W = 0$ corresponds to the inner and $x'/W = 1$

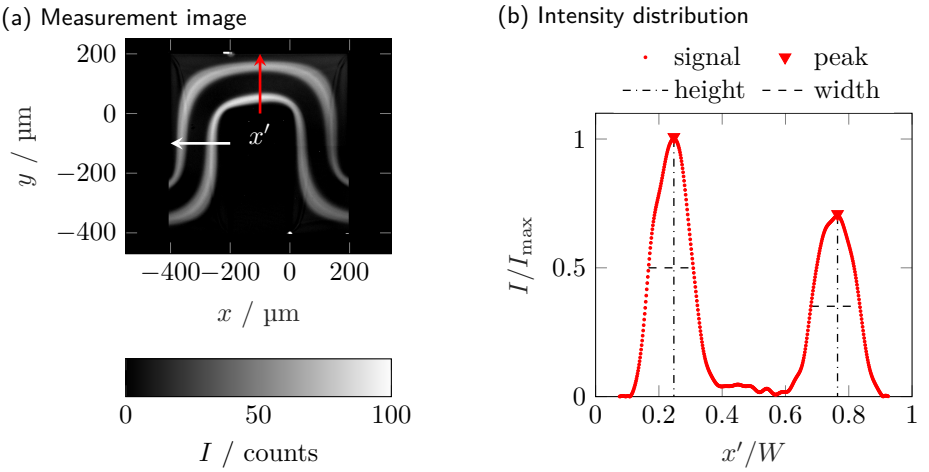

Figure 3.5.: (a) Sample of pre-processed image containing PS-3 particles at $\mathrm{Re_b} = 26$ in the 25th serpentine loop. Arrows indicate the locations and directions of evaluation. Flow direction is from right to left; (b) Corrected, sampled and normalized intensity profile extracted along the red arrow that is shown in Figure 3.5(a).

to the outer microchannel wall. Intensities I are normalized by the respective maximum intensity value I_{max} of each extracted intensity profile. In the end, peaks of the resulting intensity profiles are detected. Their location and width, which is defined as the full width at half the maximum peak intensity (FWHM), are used as characteristics of particle streaks. In Figure 3.5(b), the streak widths are indicated by horizontal dashed lines.

3.4. Astigmatism Particle Tracking Velocimetry[1]

Astigmatism Particle Tracking Velocimetry (APTV) measurements are performed in the sharp-corner serpentine microchannel to determine the three-dimensional distribution of microparticles of different sizes and densities. The results are evaluated with regard to the size fractionation performance and to explore possibilities for density fractionation along the microchannel height.
The principal experimental set-up that is used for this study is described in section 3.1. Additional technical details that are relevant for the performed APTV

[1] Parts of this section are published in Blahout et al. (2020), used under CC BY 4.0. The original contents have been edited and/or extended for this work.

measurements are provided in section 3.4.1. The procedures with which calibration and measurement images are recorded and pre-processed are described in section 3.4.2.

3.4.1. Experimental set-up

To reconstruct three-dimensional particle distributions inside the sharp-corner serpentine microchannel, the experimental set-up that is described in section 3.1 is utilized. Illumination is provided by the Litron Nano S 65-15 PIV laser and images are recorded with the LaVision Imager pro SX CCD camera. In front of the camera, a cylindrical lens with a focal length of $f = 200\,\mathrm{mm}$ is used. The commercial software DaVis 8.4 (LaVision GmbH, Germany) is used for image acquisition and pre-processing.
APTV measurements are performed inside the 25th serpentine loop (see also Figure 3.3). The size and density fractionation performance is studied by using PS-3, PS-10 and MF-10 particles that are suspended in distilled water. For more details on the particle properties see also Table 3.2 in section 3.2.2.

3.4.2. Calibration procedure and experimental execution

Double-frame calibration images are recorded using a scanning procedure with $\delta_\mathrm{z} = 1\,\mu\mathrm{m}$ step size. All recorded images, calibration as well as measurement images, are pre-processed with the same procedure before evaluation. Following Cierpka et al. (2010), a median filter with 5 px filter length is applied to reduce spatial image noise, in the first step. In the second step, a bandwidth filter is used to nearly completely eliminate background noise, while keeping structures between 3 and 70 px diameter. In the last step, images are dewarped on the basis of the recording of a calibration grid. All pre-processing steps are performed in the commercial software DaVis 8.4 (LaVision GmbH, Germany).
Seven to eight sedimented particles that are distributed over the field of view are used for each calibration curve. For APTV data evaluation, an in-house Matlab code is used that utilizes the Euclidean method proposed by Cierpka et al. (2011). To determine the measurement uncertainty with which the out-of-plane particle position can be reconstructed, absolute z-positions of the centers of sedimented particles are reconstructed from the calibration recordings and are compared to their theoretical position at $z = d_\mathrm{p}/2$. The resulting standard deviations between reconstructed and theoretical z-positions are smaller than 2.7 µm for all particle groups. Additional analyses also confirmed that particle z-positions can be reconstructed over the complete microchannel height with the previously described procedure.
After the in situ calibration, measurements are performed inside the 25th serpentine loop (see also Figure 3.3) at different bulk Reynolds numbers of $67 \leq \mathrm{Re_b} = (u_\mathrm{b} \cdot d_\mathrm{h})/\nu \leq 100$. Here, u_b denotes the bulk velocity that is calculated from the

volume flow rate Q and the cross-sectional area A as $u_\mathrm{b} = Q/A$. Bulk Reynolds numbers and corresponding volume flow rates for the APTV measurements are given in Table 3.4.

Table 3.4.: Flow parameters at which APTV measurements are performed

$\mathrm{Re_b}$	67	73	80	87	93	100
Q / $\mathrm{mL\,min^{-1}}$	0.50	0.55	0.60	0.65	0.70	0.75

For both, calibration and measurements, a mixture of PS-3 particles and either PS-10 or MF-10 particles is injected into the serpentine microchannel. Small and large particles are distinguished during the evaluation, due to different astigmatism characteristics. These result in individual calibration curves for small and large particles. Thus, size fractionation results of PS-3 and PS-10 particles can be obtained from the same measurements. An outlier criterion is applied on measurement images to exclude particle images from the evaluation that exceed a certain Euclidean distance from the calibration curve. Particle distributions of MF-10 particles are obtained from separate measurements and are superimposed with results of PS-10 particles at the same bulk Reynolds numbers. This is done as both, PS-10 and MF-10 particles, have the same image diameter and are, therefore, not differentiable through image processing. As the particle volume concentration in all experiments is low, that is in the order of magnitude of $\varphi = \mathcal{O}(10^{-4})$, no particle-particle interactions are expected in the experiments. Assuming negligible particle-particle interactions, particle locations of both measurement series are assumed to be independent from each other and representative for the hydrodynamic behavior of the individual particle groups. Thus, a superposition of PS-10 and MF-10 particle locations is done here.
During all measurements, 500 double-frame images are recorded at three reference plane positions, which are located $\delta_\mathrm{z} = 20\,\mu\mathrm{m}$ apart from each other. The time delay between the first and second frame is adjusted, depending on the bulk Reynolds number to obtain similar particle image displacements throughout all measurements. Thus, each particle appears once in each frame. This measurement procedure results in a total number of evaluated particles of 6899 ± 1658 (PS-3), 2518 ± 615 (PS-10) and 2461 ± 419 (MF-10), respectively, for measurements at a constant bulk Reynolds number.

3.5. Particle simulations inside a sharp-corner serpentine microchannel

In the present thesis, the focusing behavior and the fractionation performance of micron and sub-micron particles inside a sharp-corner serpentine microchannel is investigated. To deepen the understanding of the force balance that is dominant

for the motion of particles, trajectories of PS-3 and PS-10 particles are simulated with different simulation approaches. The numerical set-up and the simulation parameters of fully coupled simulations of PS-10 particles are described in section 3.5.1. The numerical set-up and the simulation procedure of one-way coupled simulations of PS-3 particles are described in section 3.5.2.

3.5.1. Fully coupled simulations of PS-10 particles

Trajectories of PS-10 particles are simulated by a fully coupled simulation approach that combines the Lattice Boltzmann Method (LBM) with the Discrete Element Method (DEM). The flow domain has the same geometrical dimensions as the sharp-corner serpentine microchannel that is used for experimental investigations (see section 3.2.1). It shall be noted that for these simulations an in-house algorithm of the Chair of Mechanical Process Engineering and Solids Processing of the Technische Universität Berlin is utilized. The simulations are conducted by S. R. Reinecke at the Technische Universität Berlin. Simulation results are kindly provided for further analysis of the force contributions that act on individual particles. The simulation algorithm is also used in Reinecke et al. (2021).
The liquid flow simulations are performed by the LBM approach. For this, the flow domain is discretised by a grid with equidistant spacing. This results in a grid that contains 526848 nodes, whereas the microchannel height is discretized by 14 nodes. It shall be noted that the provided number of nodes also includes nodes that are inside the actual microchannel walls. The time step size during the individual simulations is kept constant. For the LBM approach, a D3Q19 model is utilized that uses discrete velocities in all three spatial dimensions and in 19 directions. For the collision model, a Multiple Relaxation Times (MRT) operator (d'Humières, 2002) is used, which is modified to deliver viscosity independent truncation errors for steady state solutions (Khirevich et al., 2015). The liquid flow is realized by applying a body force on the fluid volume. For the LBM simulations of this work, the body force method that is provided by He et al. (1997) in the formulation of Mohamad and Kuzmin (2010) is utilized. At the microchannel walls and surfaces of individual particles, the no-slip condition is applied by bounce-back methods. A periodic boundary condition is applied at the inlet and outlet of the flow domain, as shown in the schematic of the flow domain in Figure 3.6.
The system of suspended particles is simulated by a DEM approach (Cundall and Strack, 1979). For this, the translational and rotational motion of particles is determined based on Newton's and Euler's second laws.
The LBM and DEM simulations are coupled by exchanging specific quantities between both algorithms. Thus, hydrodynamic forces determine the motion of suspended particles. In turn, the presence of particles disturbs the liquid flow field. Specifically, the particle positions inside the flow domain as well as their velocities are transferred from the DEM to the LBM algorithm. Vice versa, the hydrodynamic forces and torques that are exerted onto the particles and their

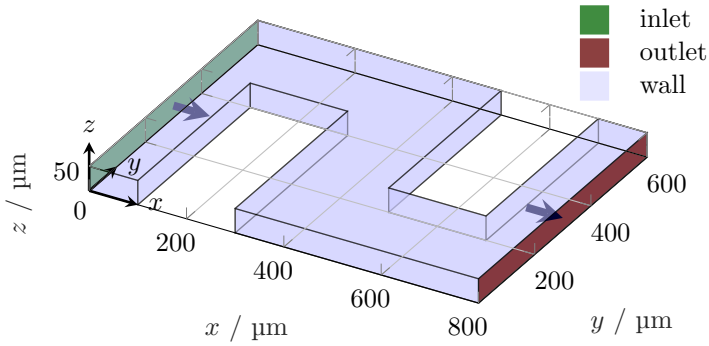

Figure 3.6.: Numerical flow domain and boundary conditions that are utilized for the coupled LBM-DEM simulations.

respective positions are the basis for the calculation of the particle motion. For this, the force algorithm described by Aidun et al. (1998) is used, which is modified to work with interpolated bounce-back methods.
In the first time step, 15 PS-10 particles are injected at random positions inside the flow domain. The simulations are run, until the particle positions in the cross-sectional plane at $x = 600\,\mu m$ are constant. In the end, simulation results are extracted such that particles pass at least one complete serpentine loop. These results are the basis for the analysis of the force balance that is acting on individual particles.

3.5.2. One-way coupled simulations of PS-3 particles

For simulations of PS-3 particle trajectories a flow domain with the same geometrical dimensions as the microchannel that is used for experimental investigations (see section 3.2.1) is used. Simulations are performed at bulk Reynolds numbers of $Re_b = 33$ and $Re_b = 67$, utilizing an one-way coupled Euler-Lagrange approach. Thus, simulations are performed in two consecutive steps. First, solely the liquid flow field is simulated with a finite volume approach. For this, the Navier-Stokes equations are solved for a Newtonian liquid. As the highest bulk Reynolds number that is considered in these simulations is $Re_b = 67$, a laminar simulation is performed without considering turbulent effects. Furthermore, the flow field simulations are isothermal, i.e. the liquid properties are constant. Second, resulting flow fields are used to simulate the particle movement in the flow using an one-way coupling approach. This means, a particle is moved by solving its equation of motion, whereas the sum of hydrodynamic forces that is acting on the particle is calculated on the basis of the flow field in its vicinity. Furthermore, the presence of particles does not disturb the liquid flow field. Both simulations are performed

with OpenFOAM v1912. For the liquid flow simulations the stationary, finite volume solver simpleFOAM is used. Particle simulations are performed with an in-house extension of the publicly available Discrete Particle Method (DPM) solver DPMFoam. The formulations and implementations of the particle forces that are utilized in this work are identical to those of the original DPMFoam solver. Further information about the extended DPMFoam solver can be found in Wegt et al. (2020).
The boundary conditions that are utilized for simulations of the liquid flow fields are described in section 3.5.2.1. An error estimation of the liquid flow field simulations follows in section 3.5.2.2. The boundary conditions that are utilized for simulations of the particulate flows are described in section 3.5.2.3.

3.5.2.1. Boundary conditions of the liquid flow simulations

The liquid flow field is calculated by solving the incompressible, stationary Navier-Stokes equations. The geometry of the flow domain and the individual regions at which boundary conditions are applied are shown in Figure 3.7.

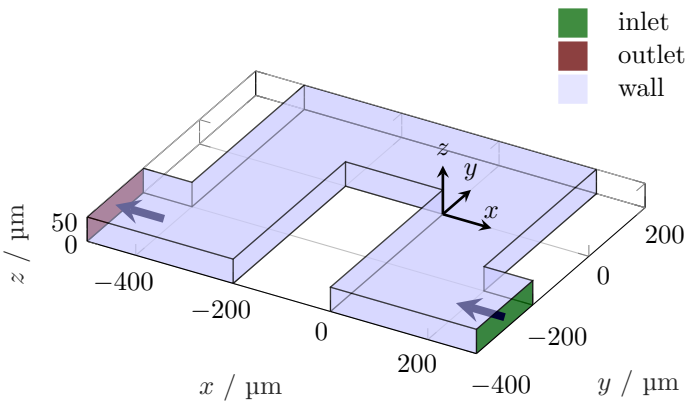

Figure 3.7.: Geometry and boundary conditions that are utilized for the liquid flow simulations.

To reduce the size of the numerical domain, only a single serpentine loop is simulated and a periodic boundary condition between the inlet and outlet is used. Furthermore, a no-slip boundary is provided at the channel walls. A static pressure of $p = 100\,000\,\mathrm{Pa}$ is applied at the face center of the outlet, i.e. $(x, y, z) = (-500\,\mu\mathrm{m}, -300\,\mu\mathrm{m}, 25\,\mu\mathrm{m})$. At the inlet, the bulk velocity that is calculated from the corresponding bulk Reynolds number $\mathrm{Re_b} = \boldsymbol{u}_\mathrm{b} \cdot d_\mathrm{h}/\nu$ is used as boundary condition. From this, a force is calculated and applied on all cells that belong to the inlet face to preserve the specified mean velocity. The simulated bulk Reynolds numbers as well as the corresponding mean velocities $\boldsymbol{u}_\mathrm{b}$ and volumetric

flow rates $Q = \boldsymbol{u}_\mathrm{b} \cdot A$ are given in Table 3.5.

Table 3.5.: Reynolds number, mean velocity and volumetric flow rate that are used for simulations of PS-3 particle trajectories.

Re_b	$\boldsymbol{u}_\mathrm{b}$ / $\mathrm{m\,s^{-1}}$	Q / $\mathrm{mL\,min^{-1}}$
33	-0.417	0.25
67	-0.833	0.5

The flow domain is spatially discretized with a block-structured grid that consists of 9600000 hexahedral cells. Due to the simplicity of the flow domain, the numerical grid is orthogonal in all spatial directions. To take flow gradients appropriately into account, a grading is applied to refine the grid towards the top, bottom and side walls, as well as towards the center plane at half the flow domains height, i.e. $z = 25\,\mu\mathrm{m}$. The convergence of the simulations as well as the grid independence are verified by estimating the iteration and discretization errors. An analysis of these error estimates is provided in section 3.5.2.2.

3.5.2.2. Error estimation

As the Navier-Stokes equations cannot be solved analytically for a serpentine microchannel flow like it is investigated in the present study, these have to be solved iteratively on a numerical grid that discretizes the flow domain. For this, the partial derivatives of the Navier-Stokes equations are approximated by a second order central differencing scheme.
Due to the discretization of the flow domain and the truncation that results from the approximation of the partial derivatives, numerical results may differ from the true solution. In this section, error estimates are reported to account for the iteration error as well as for the discretization error, respectively.

Iteration errors Due to the iterative solution of the Navier-Stokes equations, the simulation results may differ from the exact solutions, even if simple flow problems are considered. A measure for this difference is the iteration error $\epsilon_{\mathrm{It,i}}$. Although the iteration error may not be eliminated completely, even if a simulation is run for a large amount of time steps, its estimation is crucial to be able to evaluate the accuracy of the numerical solution. The iteration error is calculated for every cell i of the numerical grid as:

$$\epsilon_{\mathrm{It,i}} = \left| \frac{\phi_\mathrm{i}(t) - \phi_\mathrm{i}(t = t_\infty)}{\phi_\mathrm{i}(t = t_\infty)} \right| \tag{3.1}$$

Here, $\phi_\mathrm{i}(t)$ denotes an arbitrary flow quantity at time t and $\phi_\mathrm{i}(t = t_\infty)$ is the same flow quantity after a large amount of iterations at which no further reduction of the iteration error can be expected. In the present study, the iteration error is

calculated with regard to the velocity components in x-, y- and z-direction, i.e. u, v and w, respectively, as well as to the static pressure p. The calculation of the iteration error with respect to the individual flow quantities is performed for the flow results at bulk Reynolds numbers of $\mathrm{Re_b} = 33$ and $\mathrm{Re_b} = 67$.
The iteration errors that are given in the following are calculated at the time steps, where the root mean square (RMS) of the residuals of the iterative solution is smaller than 10^{-7} for the velocity components and smaller than 1×10^{-6} for the static pressure. These are compared to the respective values that are obtained, if the RMS of the respective residuals are in the order of magnitude of $\mathcal{O}(10^{-10}) - \mathcal{O}(10^{-9})$ for the velocity components and $\mathcal{O}(10^{-7})$ for the static pressure. After the iteration errors are calculated in every cell of the numerical grid, they are averaged over the whole flow domain for every flow quantity individually. The resulting error estimates are given in Table 3.6.

Table 3.6.: Averaged iteration error estimates for individual flow quantities.

$\mathrm{Re_b}$	$\bar{\epsilon}_{\mathrm{It,u}}$ / %	$\bar{\epsilon}_{\mathrm{It,v}}$ / %	$\bar{\epsilon}_{\mathrm{It,w}}$ / %	$\bar{\epsilon}_{\mathrm{It,p}}$ / %
33	0.013 ± 0.12	0.0077 ± 0.047	0.047 ± 0.80	$(0.00 \pm 1.85) \times 10^{-8}$
67	0.0015 ± 0.01	0.0011 ± 0.0052	0.0055 ± 0.062	$(0.0 \pm 9.1) \times 10^{-9}$

All averaged iteration errors are smaller than 1% for the solutions that are obtained at the RMS limits of 1×10^{-7} for the velocity components and 1×10^{-6} for the static pressure. Thus, the results are considered to be sufficiently accurate and are utilized as a basis for the subsequent particle simulations.

Discretization errors Due to the spatial discretization of the flow domain by a numerical grid in which the governing equations, i.e. the Navier-Stokes equations, are approximated, the numerical solution of a flow differs from the exact solution. A measure for this truncation is the discretization error (Ferziger and Peric, 2008). An estimate of the discretization error can be obtained by comparing the flow solutions resulting from systematically refined numerical grids. The discretization error furthermore provides information about the dependency of the solution on the numerical grid.
As a basis for the estimation of the discretization error, a characteristic grid size L_i of every cell i is defined as:

$$L_\mathrm{i} = V_\mathrm{i}^{\frac{1}{3}} \tag{3.2}$$

Here, V_i denotes the volume of cell i. From the grid size a grid refinement factor can be calculated for systematically refined numerical grids. In the present study, three numerical grids are considered for the estimation of the discretization error. The coarsest grid (3) has 600000 cells in total and is the basis for the grid refinement. Specifically, the amount of cells is continuously doubled in x- and y-direction to generate a medium (2) and a fine (1) grid, whereas the amount of cells in z-direction is set constant to 30. The resulting total numbers of cells for the three numerical

grids are given in Table 3.7.

Table 3.7.: Number of cells for the fine (1), medium (2) and coarse (3) grid.

	fine (1)	medium (2)	coarse (3)
N	9600000	2400000	600000

Based on the three, systematically refined numerical grids, the following grid refinement factors C_r are determined:

$$C_{\mathrm{r,i},21} = \frac{L_{\mathrm{i},2}}{L_{\mathrm{i},1}} \tag{3.3}$$

$$C_{\mathrm{r,i},32} = \frac{L_{\mathrm{i},3}}{L_{\mathrm{i},2}} \tag{3.4}$$

The average grid refinement factor between the fine (1) and the medium (2) grid reads $\overline{C}_{\mathrm{r},21} = 1.59 \pm 0.0053$. Between the medium and the coarse grid, the average grid refinement factor reads $\overline{C}_{\mathrm{r},32} = 1.59 \pm 0.012$. Therefore, the grid refinement factors are larger than the recommended value of $C_\mathrm{r} > 1.3 - 1.5$ (Celik et al., 2008; Ferziger and Peric, 2008). As both grid refinement factors are nearly identical and the deviations throughout the individual numerical grids are small, a global refinement factor of $C_{\mathrm{r,i}} = 1.59$ is used for the following calculations.
The discretization error $\epsilon_{\mathrm{Disc,i}}$ in cell i is estimated as (Ferziger and Peric, 2008):

$$\epsilon_{\mathrm{Disc,i}} = \left| \frac{\phi_{\mathrm{i},1} - \phi_{\mathrm{i},2}}{C_{\mathrm{r,i}}^{\chi_\mathrm{i}} - 1} \right| \tag{3.5}$$

with the exponent χ_i:

$$\chi_\mathrm{i} = \frac{\ln \left| \frac{\phi_{\mathrm{i},2} - \phi_{\mathrm{i},3}}{\phi_{\mathrm{i},1} - \phi_{\mathrm{i},2}} \right|}{\ln C_{\mathrm{r,i}}} \tag{3.6}$$

The resulting discretization errors with regard to the flow velocities in x-, y- and z-direction u, v and w, respectively, as well as to the velocity magnitude $|\boldsymbol{u}|$ are provided in Table 3.8. Flow quantities are obtained from simulations at a bulk Reynolds number of $\mathrm{Re_b} = 67$ and from time steps where the iteration errors of all flow quantities are smaller than 1%. The individual error estimates are averaged over the whole flow domain.
Celik et al. (2008) recommend additional estimates of the discretization error. These are also based on the flow results of three systematically refined grids. These estimates are the approximate discretization error $\epsilon_{\mathrm{a,Disc}}$, the grid convergence index GCI and the extrapolated relative error $\epsilon_{\mathrm{e,Disc}}$. Averages of these estimates are also provided in Table 3.8.
The underlying formulations of the previously described discretization error estimates are given in the following. The approximate discretization error $\epsilon_{\mathrm{a,Disc}}$ is

estimated as (Celik et al., 2008):

$$\epsilon_{\mathrm{a,Disc,i}} = \left| \frac{\phi_{\mathrm{i},1} - \phi_{\mathrm{i},2}}{\phi_{\mathrm{i},1}} \right| \tag{3.7}$$

From this, the grid convergence index $\mathrm{GCI_i}$ is calculated as:

$$\mathrm{GCI_i} = \frac{1.25\epsilon_{\mathrm{a,Disc,i}}}{C_{\mathrm{r,i}}^{\chi_\mathrm{i}} - 1} \tag{3.8}$$

The grid refinement factor $C_{\mathrm{r,i}}$ and its exponent χ_i are herein identical to the formulations that are described above.
The extrapolated relative error $\epsilon_{\mathrm{e,Disc,i}}$ is calculated as:

$$\epsilon_{\mathrm{e,Disc,i}} = \frac{\phi_{\mathrm{e,i}} - \phi_{\mathrm{i},1}}{\phi_{\mathrm{e,i}}}, \tag{3.9}$$

utilizing the extrapolated flow quantities $\phi_{\mathrm{e,i}}$ as follows:

$$\phi_{\mathrm{e,i}} = \frac{C_{\mathrm{r,i}}^{\chi_\mathrm{i}} \cdot \phi_{\mathrm{i},1} - \phi_{\mathrm{i},2}}{C_{\mathrm{r,i}}^{\chi_\mathrm{i}} - 1} \tag{3.10}$$

Table 3.8.: Averaged discretization error estimates according to Ferziger and Peric (2008) and Celik et al. (2008)

ϕ_i	$\overline{\epsilon}_{\mathrm{Disc,i}}$ / %	$\overline{\epsilon}_{\mathrm{a,Disc,i}}$ / %	$\overline{\mathrm{GCI}}_\mathrm{i}$ / %	$\overline{\epsilon}_{\mathrm{e,Disc,i}}$ / %
u	0.16 ± 0.15	1.5 ± 1.2	0.99 ± 1.30	1.3 ± 1.2
v	0.20 ± 0.19	1.5 ± 1.1	1.1 ± 1.2	1.3 ± 1.2
w	0.0027 ± 0.0026	2.3 ± 1.7	0.96 ± 2.60	2.0 ± 1.9
$\lvert\boldsymbol{u}\rvert$	0.29 ± 0.28	0.82 ± 0.65	0.51 ± 0.77	0.73 ± 0.69

As can be seen from Table 3.8, the largest uncertainty estimate occurs for the approximated discretization error with regard to the flow velocity in z-direction, which reads $\epsilon_{\mathrm{a,Disc,w}} = (2.3 \pm 1.7)\%$. However, no definite regions with systematically increased error estimates are present. Instead, error estimates are distributed randomly over the flow domain. Consequently, the finest grid that is considered here is assumed to be sufficient to receive grid independent flow solutions and, thus, are used for the subsequent particle simulations.

3.5.2.3. Boundary conditions of the particle flow simulations

For one-way coupled particle simulations, the same flow domain and numerical grid as for the liquid flow simulations are utilized. Flow fields are obtained at residual limits of 1×10^{-7} for the velocity components and 1×10^{-6} for the static pressure.

These are the basis for the particle simulations. In the first time step of the particle simulations, 100 particles with an initial zero-velocity are injected at the inlet (see also Figure 3.7) with equidistant spacing. Specifically, all particles have an initial spatial distance of 10 µm to each other in y- and z-direction and an initial spatial distance of 5 µm to the walls. This is schematically shown in Figure 3.8.

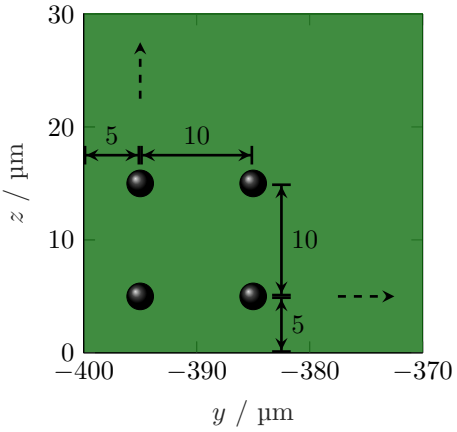

Figure 3.8.: Schematic figure of the initial particle distribution at the inlet of the sharp-corner serpentine microchannel.

To assure that particles are not displaced by a too large amount, a time step size of 1×10^{-6} s is chosen and simulations are run for a simulation time of 0.1 s, i.e. 100000 time steps. Force contributions that are considered are the drag force, gravity, the shear-gradient force and the Saffman force.

3.5.3. Force evaluation

Trajectories of PS-3 and PS-10 particles are simulated at different bulk Reynolds numbers with the previously described simulation approaches. The corresponding simulation results are the basis for subsequent force evaluations. Here, individual force contributions are calculated based on the equations that are described in section 2.1. The calculation of these contributions are performed with an in-house Matlab algorithm. Details on certain implementation aspects are described in the following.
For the calculation of the drag, the shear-gradient and the Saffman force, the liquid flow velocities and corresponding velocity gradients in the vicinity of a particle are considered. As the liquid flow velocities are only known in the cell centers of the numerical grid, the previously described flow quantities are interpolated to the particle center. For this, flow quantities are interpolated linearly, while taking all values from a cubic region around the particle center into account.

The calculation of the particle centrifugal force is based on the orbit of the particle trajectory. This orbit is determined by calculating the radius of the corresponding osculating circle. For this calculation, the location of the particle center at a certain time step, as well as the center locations of the same particle at the previous two time steps are used. Any torsion of the particle trajectory is neglected.
The previously described procedures are performed for every simulated particle at each time step and for the results of both simulation approaches. Solely for the particle simulation results that are obtained from the coupled LBM-DEM approach, a symmetric moving mean filter with five time steps filter length is applied on the particle velocities. This is done, because raw particle velocities show significant scattering, which also affects force contributions that are based on the particle velocity. It is assumed that the particle velocities are scattered for fully coupled LBM-DEM simulations, because a coarser numerical grid is used in comparison to the one-way coupled simulations. An exemplary distribution of the velocity magnitude $|\boldsymbol{u}_\mathrm{p}|$ of a particle that flows along the lower, inner trajectory at a bulk Reynolds number of $\mathrm{Re_b} = 33$ through one serpentine loop is shown as a function of the normalized restitution time t/t_ref in Figure 3.9. The normalized restitution time corresponds to the simulation time that is scaled and normalized such that the considered particle enters the serpentine loop at $t/t_\mathrm{ref} = 0$ and exits the loop at $t/t_\mathrm{ref} = 1$. The raw signal that is obtained from the simulation results is plotted as a gray line, time filtered data are plotted as black dots. It shall be noted that the time filtered velocity magnitudes are calculated from the individual, time filtered particle velocity components.
Figure 3.9 shows that the application of the previously described time filter reduces the scattering of the raw velocity magnitudes significantly, while the velocity magnitude peaks at $t/t_\mathrm{ref} \approx 0.43$ and $t/t_\mathrm{ref} \approx 0.57$ are reproduced accurately.
To associate the restitution time of the temporal force distributions with the exact locations within one serpentine loop, cross-sectional evaluation planes are defined. Unique identifiers are assigned to these planes in ascending order in flow direction. Locations of individual evaluation planes as well as the corresponding identifier are shown in Figure 3.10.
Particle simulations are performed in a Cartesian coordinate system. For the analysis of individual force contributions that act on particles, a frame that is related to the particle motion is used. The relation between the initial Cartesian and the transformed, particle related coordinate system is shown in Figure 3.11.
Figure 3.11 depicts the motion of a particle along a curved trajectory (blue arrow). The initial Cartesian coordinate system is indicated with black arrows at the lower left corner. The force vectors that are calculated in this initial Cartesian coordinate system are transformed such that the first component of the transformed force vector is tangential to the particle main flow direction (F_m). As the particle coordinate system shall be orthogonal and right-handed, the normal force component F_n is perpendicular to the particle main flow direction and thus also to F_m and is defined to be parallel to the x-y-plane of the initial Cartesian coordinate system. The

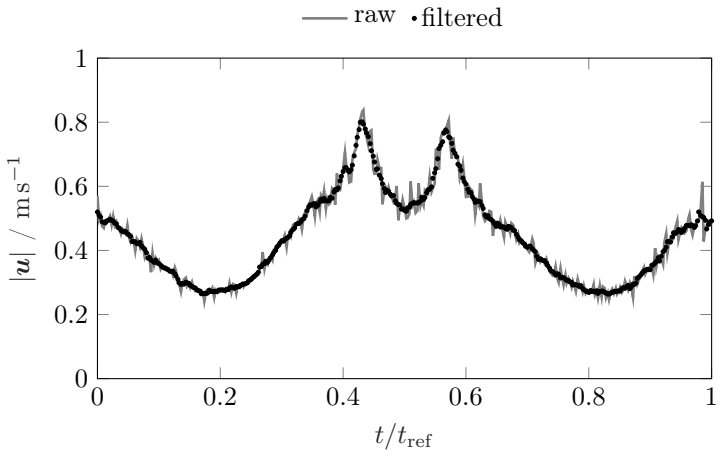

Figure 3.9.: Velocity magnitude for an exemplary PS-10 particle that flows at a lower, inner trajectory through a single serpentine loop as a function of the normalized restitution time. Results are obtained from a fully coupled LBM-DEM simulation at $\mathrm{Re_b} = 33$. The gray line denotes raw velocity magnitudes, black dots denote time filtered velocity magnitudes.

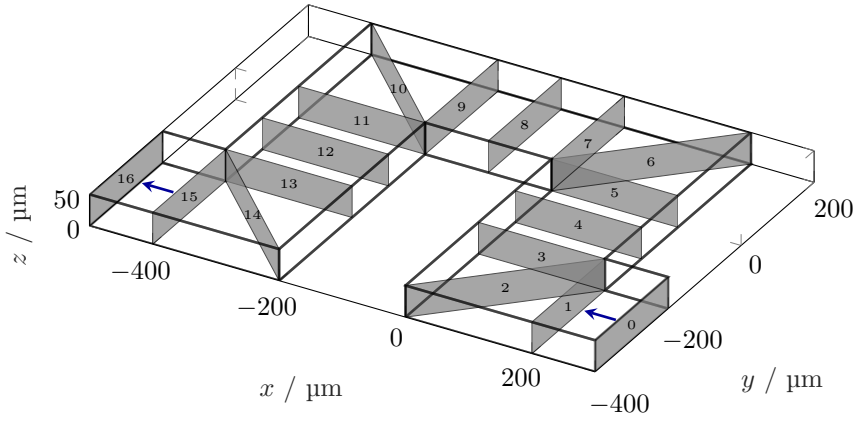

Figure 3.10.: Location of uniquely labelled evaluation planes inside one serpentine loop.

third component of the transformed force vector, the bi-normal force component F_{bn}, is orthogonal to each of the previously described force components F_{m} and F_{n}. Thus, the directions of the transformed coordinate system components are depending on the particle flow direction. Force distributions are transformed during the evaluation process for every particle and time step individually.

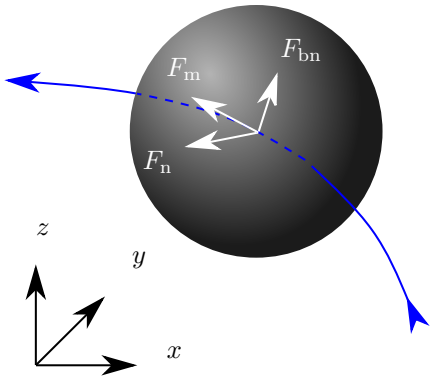

Figure 3.11.: Relation of the initial Cartesian coordinate system and the transformed coordinate system that is related to the particle flow direction.

3.5.4. Acquisition of reference flow fields

For one-way coupled simulations, the solution of the stationary, laminar flow field inside one serpentine loop is simulated as a first step. These flow field solutions are utilized to calculate the motion of individual particles in a second step. For a comparison of the simulated flow fields with experimental data, µPIV measurements are performed in a sharp-corner serpentine microchannel that is the basis for the numerical flow domain. Image acquisition, pre-processing and evaluation are performed in the commercial software DaVis 10 (LaVision GmbH, Germany). For these µPIV measurements, the experimental set-up that is described in section 3.1 is utilized. Images are recorded with the LaVision Imager SX 6M CCD camera, illumination is provided by the NewWave SOLO PIV III laser. Measurements are performed utilizing PS-0.86 particles as tracers that are suspended in pure, distilled water. In combination with the optical properties of the experimental set-up, the usage of such tracers results in an effective measurement volume of $\delta_{DoC} = 14.5\,\mu m$ (Olsen and Adrian, 2000). In accordance with the simulated flow fields, µPIV measurements are performed at bulk Reynolds numbers of $Re_b = 33$ and $Re_b = 67$ and inside the 27th serpentine loop (see also Figure 3.3). A scanning procedure that starts at the microchannel bottom is utilized to measure flow fields at seven measurement planes that have a spatial distance of $\delta_z = 12\,\mu m$ from each other. At every measurement plane, 750 double-frame images are recorded with an inter-framing time that is dependent on the considered bulk Reynolds number. For a bulk Reynolds number of $Re_b = 33$ an inter-framing time of $\Delta = 7.5\,\mu s$ and at $Re_b = 67$ an inter-framing time of $\Delta = 4\,\mu s$ is used.
Before cross-correlation, recorded measurement images are pre-processed. This targets to increase the signal to noise ratio of tracer particles. As a first pre-processing step, a spatial sliding filter with Gaussian weight and 3 px filter length is applied.

From each of these images, a background image is subtracted that is calculated from the minimum intensity value inside each pixel of the first 19 images. In the last pre-processing step, the background intensity is further reduced by applying a subtract sliding filter with a filter length of 50 px.
Pre-processed measurement images are cross-correlated with an ensemble averaging, multi-pass evaluation algorithm. For this, measurement images are sub-divided into interrogation windows of 96×96 px in the first pass and of 48×48 px in the subsequent three passes. During all passes, an interrogation window overlap of 50% is used. After the actual cross-correlation evaluation, invalid vectors are removed. Here, vectors are identified as invalid, if the detectability of the corresponding displacement correlation peak is smaller than $D < 2$ or if the deviation of the vector result is too large compared to the median averaged vector result that is obtained from its 3×3 environment. In the last step, empty vector spaces are filled up with the displacement results obtained from secondary or even smaller correlation peaks, if they fulfill the validity criteria instead or by interpolation.

3.6. Particle Image Velocimetry utilizing ring-shaped particle images[2]

Due to a reduced optical accessibility of suspension flows, PIV measurements of multiphase flows were often limited to dilute suspensions (Koutsiaris et al., 1999) or bubble flows of low gas volume fractions (Lindken and Merzkirch, 2002). For optical investigations of suspension flows with higher volume fractions, a refractive index matching of the liquid to the solid phase can be done to increase the optical accessibility (Wiederseiner et al., 2011; Blanc et al., 2013). The concept of refractive index matching can be applied to every liquid-solid combination with a transparent liquid and solid phase. Solely difficulties in handling of highly flammable or toxic liquids may restrict the choice of materials (Hassan and Dominguez-Ontiveros, 2008; Wiederseiner et al., 2011). Hence, this concept was already successfully applied for Particle Tracking Velocimetry (PTV) (P. Wang et al., 2008), Laser Doppler Velocimetry (LDV) (Haam et al., 2000), Laser Induced Fluorescence (LIF) (Chen et al., 2005) and Astigmatism Particle Tracking Velocimetry (APTV) (Brockmann et al., 2020; Brockmann and Hussong, 2021) measurements in multi-phase flows. An advantage of the PIV measurement technique compared to other optical, non-invasive measurement techniques like, e.g., the APTV approach is that no sophisticated calibration technique is required and all suspension particles can be labelled and, therefore, contribute to the measurement result.
An extension of the commonly used micro Particle Image Velocimetry (µPIV) measurement technique in presented in the present thesis. This extension utilizes particles that display a ring-shaped image. Ring-shaped intensity profiles may

[2] Parts of this section are published in Blahout et al. (2021), used under CC BY 4.0. The original contents have been edited and/or extended for this work.

emerge for refractive index matched particles with fluorescent surface labelling. This situation may be encountered for optical investigations of dense particle laden flows but also in situations where particles naturally contain mainly carrier liquid such as e.g. hydrogel particles (Byron and Variano, 2013) or cells (Lima et al., 2006). For the investigations of the present work, the displacement estimation error and the detectability of such ring-shaped particle images is compared to Gaussian and plateau-shaped particle images (section 7.1).
While a Gaussian intensity distribution is characteristic for small particle image diameters (Willert and Gharib, 1991), particles show rather a plateau-shaped intensity distribution for large image diameters. To separate the size effect from the shape effect for PIV measurements, the behavior of both, Gaussian and plateau-shaped particle images is studied over the whole investigated image size regime.
To investigate the influence of the particle image diameter and shape on the displacement estimation error and the detectability, Monte Carlo simulations are performed that are based on synthetically generated images. A description of the generation of synthetic particle images is provided in section 3.6.1.
Furthermore, ring-shaped particle images are utilized in combination with standard tracer particles to measure the bulk dynamics of both phases of a suspension simultaneously (section 7.2). The corresponding experimental procedure is described in section 3.6.2.

3.6.1. Synthetic particle image generation

In the course of this thesis, the influence of the particle image diameter on the cross-correlation result is investigated for different particle image shapes. For this, synthetic particle images are generated with Gaussian, ring- and plateau-shaped intensity profiles. While Gaussian intensity profiles are based on an analytical function, ring- and plateau-shaped profiles are taken from fit functions of experimental image data. For this, self-labelled and commercially labelled PMMA particles with a nominal particle diameter of $d_\mathrm{p} = 60\,\mu\mathrm{m}$ are suspended in a carrier liquid and recorded under laser illumination. Examples of both, ring- and plateau-shaped particle images with $d_\mathrm{p,I} \approx 70\,\mathrm{px}$ image diameter are shown in Figures 3.12(a) and (d), respectively. A particle image of Gaussian shape is shown in Figure 3.12(g).
Obviously, self-labelled PMMA particles display a ring-shaped particle image, while commercially labelled particles show a plateau-shaped intensity profile. To achieve ring-shaped particle images, first a molecular Rhodamine B dye is solved in distilled water. Afterwards, PMMA particles are suspended in this solution. After half an hour at room temperature, particles are recovered by sedimentation. The remaining solution of water and Rhodamine B is removed. In the end, labelled particles are dried in a heat bath at 70 °C. After this procedure, particles show to have a limited take up of dye, such that only the particle surface is labelled. When the particles are suspended in a refractive index matched liquid consisting of distilled water, Glycerine and Ammoniumthiocyanate (Bailey and Yoda, 2003),

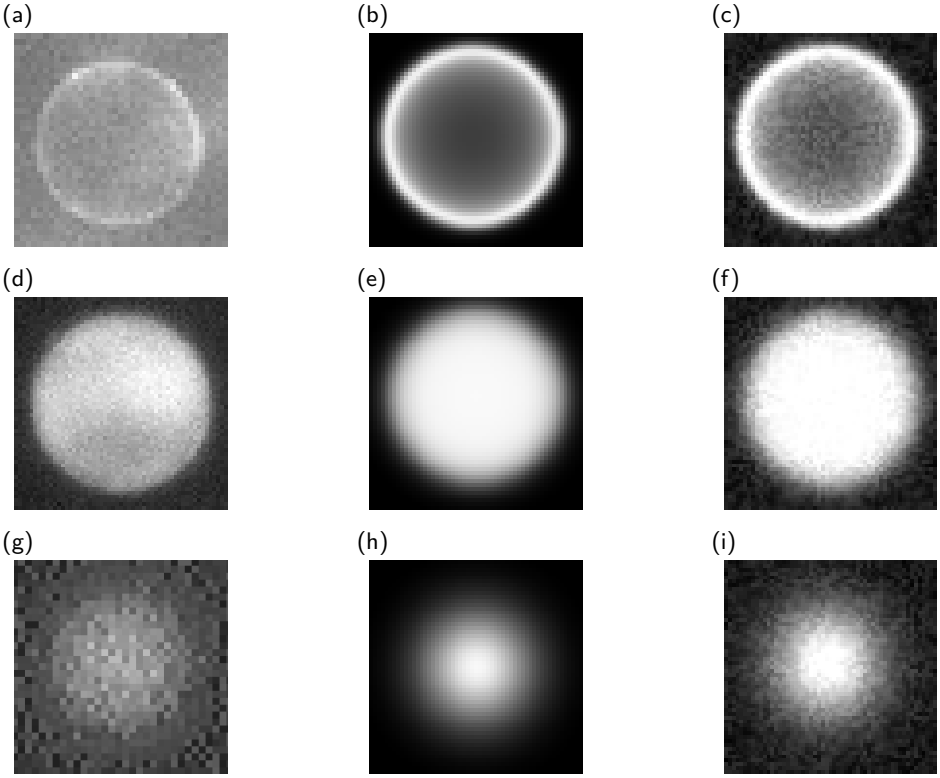

Figure 3.12.: (a) Recorded ring-shaped particle image, (b) synthetically generated ring-shaped particle image, (c) synthetically generated ring-shaped particle image with 8.5% image noise, (d) recorded plateau-shaped particle image, (e) synthetically generated plateau-shaped particle image, (f) synthetically generated plateau-shaped particle image with 8.5% image noise, (g) recorded Gaussian particle image, (h) synthetically generated Gaussian particle image, (i) synthetically generated Gaussian particle image with 8.5% image noise.

they appear transparent with a fluorescent particle rim. In contrast to this, the material of commercially available particles is completely labelled, resulting in a plateau-shaped particle image.
Radial intensity distributions of ring- and plateau-shaped particle images are determined from approximately 500 recorded, individual particle images by fitting a smoothing-spline to all intensity distributions. With that, different synthetic particle image diameters are realized for synthetic data generation of ring-shaped and plateau-shaped particle images by scaling the smoothing-spline function. The

radial intensity distribution of synthetic Gaussian particle images are calculated by the Gaussian density function:

$$I(\boldsymbol{r}) = \frac{1}{\sqrt{2\pi\sigma^2}} \cdot \exp\left(-0.5 \cdot \frac{(\boldsymbol{r}-\mu)^2}{\sigma^2}\right) \tag{3.11}$$

with $\mu = 0$. The variance of the Gaussian density function σ^2 is adjusted iteratively, so that the width of the Gaussian density function corresponds to the specified particle image diameter. This width is defined to be at the point where the Gaussian curve reaches 0.5% of its maximum value. Finally, this threshold value is subtracted from the resulting shape function to reach a zero intensity value at $r_{\mathrm{p,I}}/r_{\mathrm{p,I,max}} = 1$. The resulting radial intensity distributions $I\left(r_{\mathrm{p,I}}/r_{\mathrm{p,I,max}}\right)$, normalized by the corresponding maximum intensity $I_{\max}$ of all three particle image shapes are shown in Figure 3.13.

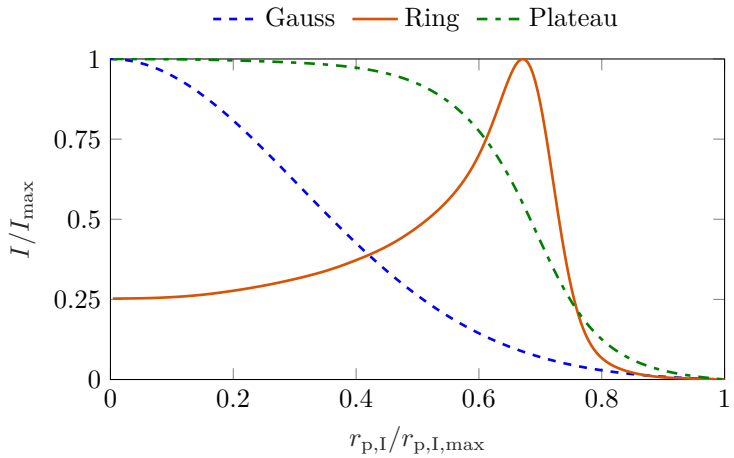

Figure 3.13.: Radial, fitted intensity distributions of Gaussian, ring- and plateau-shaped particle images.

To create particle images of different discrete pixel sizes, radial intensity distributions are intersected and piecewise averaged intensity values are assigned to the corresponding pixel locations. Synthetic ring- and plateau-shaped particle images of $d_{\mathrm{p,I}} = 60\,\mathrm{px}$ are shown in Figure 3.12(b) and (e), respectively. As experimental data are usually affected by image noise, both, synthetic particle images without (see Figure 3.12(b), (e), (h)) and with 8.5% image noise (see Figure 3.12(c), (f), (i)), are analysed and compared in the course of this paper. Image noise is calculated as the ratio of the mean background intensity and the maximum intensity value of images with a particle image diameter of $d_{\mathrm{p,I}} = 60\,\mathrm{px}$. Noise levels in the order of magnitude as mentioned above are encountered, even after pre-processing of raw

recordings of suspension flows with ring-shaped particle images.
It may be noted, that assigning a continuous intensity function (as given in Figure 3.13) to discrete pixels leads to a reduction of the maximum particle intensity values for small particle image diameters. Figure 3.14 shows the intensity maxima as a function of the particle image diameter.

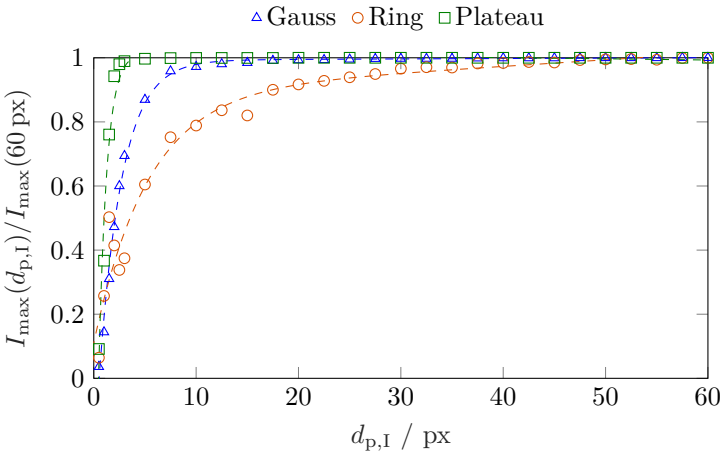

Figure 3.14.: Maximum intensity values as a function of the particle image diameter for Gaussian, ring- and plateau-shaped particle images. Dashed lines denote fits to the respective data.

As can be seen, this discretisation error becomes prominent for small particle images of a few pixels diameter and is strongest for ring-shaped particle images due to a very sharp intensity peak at $r_{\mathrm{p,I}}/r_{\mathrm{p,I,max}} \approx 2/3$, evident in Figure 3.13. However, in real experimental situations where e.g. noise-affected ring-shaped particle images may indeed give a weaker fluorescence signal for identical laser energy input compared to noise-affected plateau-shaped particle images, the cross-correlation result may be significantly affected for particle image diameters of $d_{\mathrm{p,I}} \leq 10\,\mathrm{px}$. Further details are discussed in section 7.1.
To evaluate the size sensitivity of Gaussian, ring- and plateau-shaped particle images on the cross-correlation result, 500 double-frame images with five randomly distributed particle images in each interrogation window are created synthetically. To investigate solely the influence of the particle image shape on the cross-correlation result by means of the detectability and the displacement estimation error, defocused particle images are not considered, i.e. all particle images are in focus in all synthetically generated images. Furthermore, particle images either have a zero displacement between consecutive frames or, in case of non-zero displaced particle images, are always fully located inside interrogation windows. Due to this, neither an in-plane loss-of-pairs nor an out-of-plane loss-of-pairs is present and

the corresponding factors with which these effects are taken into account, F_{in} and F_{out}, respectively, read $F_{\mathrm{in}} = F_{\mathrm{out}} = 1$. This results in a constant effective number of particle images of $N_{\mathrm{p,I}} \cdot F_{\mathrm{in}} \cdot F_{\mathrm{out}} = N_{\mathrm{p,I}} = 5$ for all particle image diameters, which is in agreement with the recommended value for PIV measurements (Keane and Adrian, 1992). The displacement estimation error is evaluated based on (2.21). For all investigations the interrogation window size is chosen to be $256 \times 256\,\mathrm{px}$. At first, overlapping particle images as well as particle images intersected at the interrogation window border, are suppressed to isolate the effect of the particle image size and shape on the cross-correlation result (see sections 7.1.1 and 7.1.2). Consequently, particle images are also zero displaced between two consecutive frames.
The influence of zero displaced particle images that are located on the interrogation window border is investigated separately in section 7.1.3. For this, sets of double frame images with one, three and five out of five particle images are placed with their center point on the interrogation window border. Particle images inside the interrogation window and those on its border are distributed randomly whereas particle overlaps are excluded again. Examples of synthetically generated ring-shaped particle images of $d_{\mathrm{p,I}} = 60\,\mathrm{px}$ with zero and three intersected particle images are shown in Figures 3.15(a) and (b).

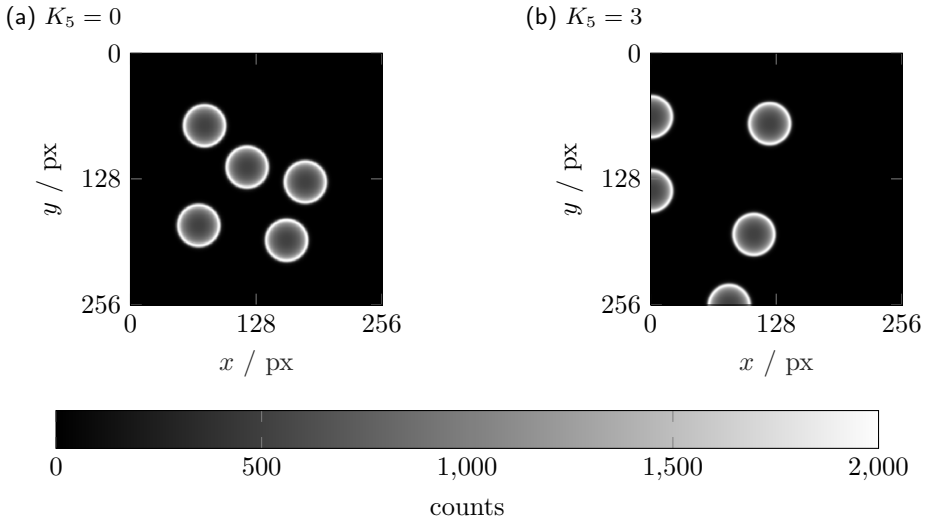

Figure 3.15.: Synthetic sample images of (a) five ring-shaped particle images and (b) five ring-shaped particle images including three intersected particle images ($K_5 = 3$).

The effect of non-zero particle image displacements on the cross-correlation result is investigated in section 7.1.4. Overlapping particle images and intersections at the interrogation window borders are excluded.

3.6.2. Experimental application

The concept of utilizing particles with ring-shaped image is also demonstrated experimentally in chapter 7. Details of the experimental set-up that are relevant for these measurements and go beyond the description that is provided in section 3.1 are given in section 3.6.2.1. Afterwards, the experimental procedure is described in section 3.6.2.2. Details of the image pre-processing and evaluation procedure are provided in section 3.6.2.3.

3.6.2.1. Experimental set-up

Micro Particle Image Velocimetry (µPIV) measurements of a suspension flow inside the straight microchannel with trapezoidal cross-section (see Figure 3.2(a)) are performed with the experimental set-up that is described in section 3.1. Here, the Litron Nano S 65-15 PIV laser is used for illumination and images are recorded by the LaVision Imager pro SX double-frame CCD camera. To grant optical accessibility despite the presence of large ring-shaped particle images, a refractive index matching is applied. For this, a ternary carrier liquid that consists of distilled water, Glycerine and Ammoniumthiocyanate (Bailey and Yoda, 2003) is used. Polymethylmethacrylate (PMMA) particles with 60 µm diameter that are labelled as described in section 3.6.1 are suspended in this carrier liquid. The carrier liquid has a density of $\rho = (1178.07 \pm 0.37)\,\mathrm{kg\,m^{-3}}$, a refractive index of $n = 1.489$ and a dynamic viscosity of $\eta = (5.96 \pm 0.11) \times 10^{-3}\,\mathrm{Pa\,s}$. PMMA particles (Microbeads Spheromers CA60) have a density of $\rho_\mathrm{p} = 1200\,\mathrm{kg\,m^{-3}}$ and a refractive index of $n_\mathrm{p} = 1.4895 \pm 0.0035$. Thus, the deviations between carrier liquid and particle properties are less than 2% in density and 0.3% in refractive index. A nominal volumetric concentration of $\varphi = 5\%$ is used throughout the experiments. Standard polystyrene tracer particles of 1.19 ± 0.03 µm diameter (microParticles GmbH) are added to the suspension. The same tracer particles are also used for reference measurements of the one phase flow. For both, reference and suspension flow measurements, the same batch of carrier liquid is used.

3.6.2.2. Experimental procedure

Measurements inside the straight microchannel with trapezoidal cross-section are performed at a bulk Reynolds number of $Re_\mathrm{b} = (u_\mathrm{b} \cdot h)/\nu = 0.71$. Here, u_b denotes the bulk fluid velocity calculated from the volume flow rate and the measured microchannel cross-section and ν denotes the kinematic viscosity of the ternary carrier liquid, that is calculated from the measured dynamic viscosity and density (see section 3.6.2.1). Resulting velocity fields of the suspension flow are compared

to velocity results of the one phase flow at the same bulk Reynolds number. As the depth of correlation (Olsen and Adrian, 2000) is $\delta_{\mathrm{DoC}} \approx 16\,\mu\mathrm{m}$ for 1.19 µm PIV tracer particles in combination with the optical configuration of the experimental set-up, measurements are performed at 25 different z-planes with a spatial distance of $\delta_{\mathrm{z}} \approx 22\,\mu\mathrm{m}$ from each other to prevent an overlapping of measurement volumes. At every measurement plane, 500 double-frame images are recorded with a frequency of 4 Hz. An inter-framing time of $\Delta = 750\,\mu\mathrm{s}$ is used.

3.6.2.3. Image pre-processing and evaluation

Image pre-processing steps are performed before the actual cross-correlation evaluation to increase the signal to noise ratio of particle images. In the following, the utilized general image pre-processing procedure is described.
Afterwards, the procedure that is used to segment tracer and ring-shaped suspension particle images is described. This is necessary to measure bulk slip velocities, as tracer particles with small particle image diameters and suspension particles with large particle image diameters are suspended simultaneously to the flow. For the cross-correlation evaluation both types of particle images are evaluated individually. Lastly, the parameters that are used for the cross-correlation evaluation of pre-processed and segmented particle images are described.

General image pre-processing The general image pre-processing procedure consists of three steps. In a first step a minimum intensity image of the first 19 images of each recording sequence is generated and subtracted from each recorded image of the same recording sequence. This reduces stationary background noise and reflections. In a second step, a spatial sliding average filter of 3 px edge length including a Gaussian weighting function is applied to each image to reduce salt-and-pepper noise. In a third step, a spatial subtract sliding average filter of 200 px edge length is applied to each image to further enhance the signal to noise ratio. This results in an increased intensity gradient at the ring-shaped suspension particle image rim and, therefore, facilitates the detection of ring-shaped suspension particle images. The segmentation procedure is described in the following section.

Particle image segmentation Pre-processed images contain signals from both, PIV tracers and ring-shaped suspension particle images. To segment individual particle groups, an in-house Matlab code is used. The segmentation procedure is based on Anders et al. (2019).
The first step during image segmentation is to detect large suspension particle images, specifically their center points and radii. This is done for both frames of a double-frame image. The center point and radius information are used to define one masking function that is applied on both frames. With this, intensity information of the area that is covered by suspension particle images within the original, pre-processed images are extracted.

The extraction of suspension particle images leaves spaces with zero intensity in the original images (that now contain only signals from PIV tracer particles). As shown by Anders et al. (2019), this can lead to a velocity bias, when using cross-correlation based evaluation methods. To overcome this, a spectral random masking algorithm is proposed. This utilizes the image noise information of the vicinity of suspension particle images and combines these with a bilinear fit of the spatial intensity information to fill the regions, where suspension particle images are extracted.
Intensity information of extracted suspension particle images are stored in a separate double-frame image. As these images may contain also intensity information resulting from small PIV tracer particles, further pre-processing steps are performed to obtain solely the intensity signals of suspension particles. Specifically, a sliding average filter with 7 px edge length and a Gaussian weighting function is utilized first. Afterwards, a bandwidth filter is applied that retains only structures with a length between 7 px and 25 px.

Cross-correlation evaluation Based on the pre-processed and segmented particle image recordings, velocity fields are obtained by performing sum-of-correlation cross-correlations with the commercial DaVis software (LaVision GmbH). A multi-pass method (Willert, 1996) with decreasing interrogation window sizes of $256\,\mathrm{px} \times 256\,\mathrm{px}$ during the first pass and $128\,\mathrm{px} \times 128\,\mathrm{px}$ during both, the second and third pass are utilized for the evaluation of the carrier liquid flow, i.e. for PIV tracer particle images. As suspension particles have a particle image diameter of $d_{\mathrm{p,I}} \approx 270\,\mathrm{px}$, interrogation window sizes are set to $512\,\mathrm{px} \times 512\,\mathrm{px}$ during the first pass and $256\,\mathrm{px} \times 256\,\mathrm{px}$ during the second and third pass. This is suitable, as the results based on synthetic images show that the estimation error of ring-shaped particle images is insensitive to intersections at the interrogation window borders (see section 7.1.3). For all cross-correlation evaluations, a 50% overlap of interrogation windows is used. Vector post-processing is performed to eliminate erroneous velocity data. Specifically, vector results with a detectability below two are deleted and, additionally, an universal outlier detection is applied with a 5×5 median filter. This median filter defines velocity vectors as outliers if the value of a velocity component exceeds the median of the surrounding velocity data by an absolute value that corresponds to one times the median absolute deviation. Emerging empty vector spaces are filled with velocity information resulting from the 2nd, 3rd or 4th highest correlation peak, if they fulfill the median outlier criterion instead. In the end, all remaining empty vector spaces are filled up by interpolation. Overall, $4\% - 6\%$ of all vector information are replaced in an evaluation. 90% of all replaced vectors are interpolated.

4. On the focusing behavior of micron and sub-micron particles

This chapter deals with the focusing behavior, i.e. the development of characteristic particle trajectories, of micron and sub-micron particles inside the sharp-corner serpentine microchannel. The aim is to identify experimental conditions where fractionation of individual particle groups with high purity is promising in future microfluidic systems. Hence, long-exposure fluorescence images of different microparticles are acquired and the intensity profiles are analyzed to determine the locations and widths of particle streaks. Micron sized particles of polystyrene (PS), melamine (MF) and silica (SiO_2) are investigated with respect to the size and density dependence of particle streak locations. In addition, the influence of the size of sub-micron polystyrene particles on the focusing behavior is investigated. This is a relevant development step for future microfluidic fractionation systems. A discussion of the focusing behavior of micron particles is provided in section 4.1. The focusing behavior of sub-micron particles is analysed in section 4.2.

4.1. Micron particles

The focusing behavior of polystyrene, melamine and silica particles of $d_p \approx 3.5\,\mu m$ and $d_p \approx 10\,\mu m$ is examined. In a first step, the influence of the particle size on the development of particle streaks is analyzed for each particle group separately in section 4.1.1. In a second step, the influence of the particle density is investigated for particles with equal diameters in section 4.1.2.
Particle trajectories are evaluated at different locations inside a serpentine loop. For a better conciseness, Figure 3.5(a) from section 3.3 is reproduced in Figure 4.1. Here, the location at which the particle size fractionation is evaluated is depicted with a red vertical arrow. The location at which the particle density fractionation is evaluated is depicted with a white horizontal arrow.

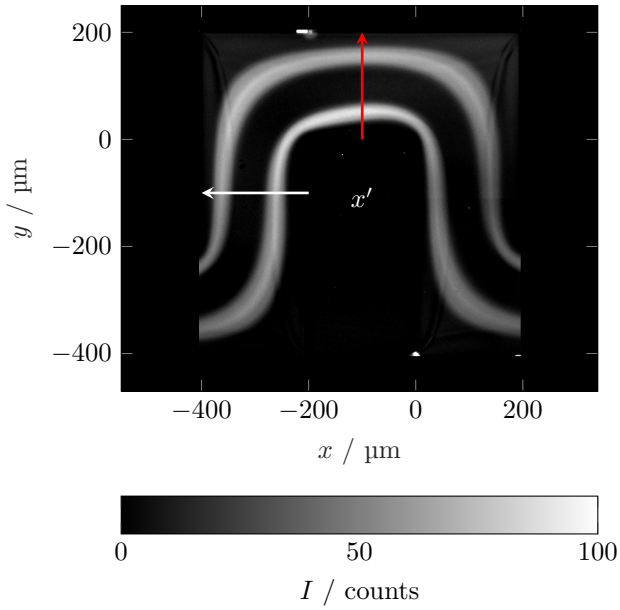

Figure 4.1.: Sample pre-processed image of PS-3 particles at $\mathrm{Re_b} = 26$ in the 25th serpentine loop. Arrows indicate the locations and directions of evaluation. Flow direction is from right to left.

4.1.1. Influence of the particle size on the focusing behavior

Particle streaks are evaluated inside the 27th serpentine loop at the location that is indicated with a vertical red arrow in Figure 4.1. Figure 4.2 shows center locations of particle streaks normalized by the microchannel width x'/W as a function of the bulk Reynolds number $\mathrm{Re_b}$ for PS-3 and PS-10 particles. Vertical errorbars indicate the particle streak width that is defined as the width at which the fluorescence signal of the particle streak is 50% of its maximum intensity. A detailed description of the determination of particle streak center locations and widths is given in section 3.3.2.2. Details on the particle properties are provided in Table 3.2. Horizontal errorbars indicate the uncertainty of the individual bulk Reynolds number, which results from the uncertainty of the kinematic viscosity determination.
Figure 4.2 shows that both, PS-3 and PS-10 particles, develop two visible streaks at $x'/W \approx 0.75$ and $x'/W \approx 0.25$ for low bulk Reynolds numbers. With increasing bulk Reynolds numbers, these two visible streaks converge until they merge into a single equilibrium streak at $x'/W \approx 0.6$. For PS-3 particles an intermediate state is observed at $105 < \mathrm{Re_b} < 121$, where up to three particle streaks become visible. While the peak locations of both particle groups are similar at low bulk Reynolds numbers, the bulk Reynolds number at which the transition from two to one visible

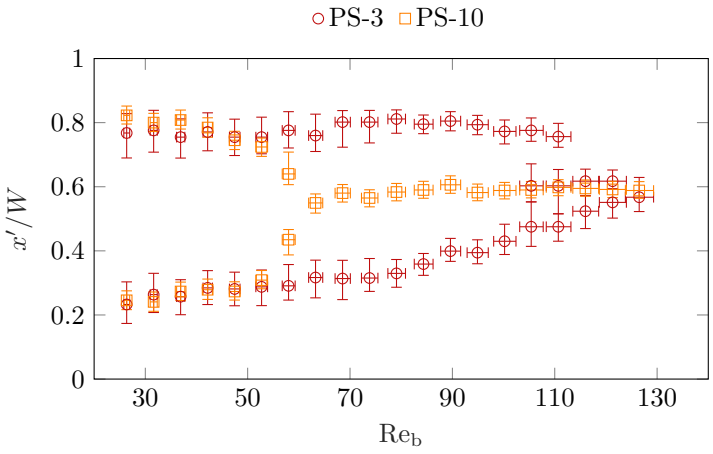

Figure 4.2.: Normalized particle streak locations and widths for PS-3 (○) and PS-10 (□) particles as a function of the bulk Reynolds number inside the 27th serpentine loop.

particle streak occurs depends on the particle size. Specifically, PS-10 particles develop a single visible streak at $\mathrm{Re_b} > 63$, while higher bulk Reynolds numbers of $105 \leq \mathrm{Re_b} \leq 121$ are required to reach the intermediate state and finally a single visible particle streak for PS-3 particles. The transition process for PS-10 particles tends to be symmetric, while for PS-3 particles a more asymmetric transition occurs. This means that for PS-3 particles the visible streak located near the inner microchannel wall continuously transitions towards the microchannel bisector, while the visible streak located near the outer microchannel wall remains at its original location for a wide bulk Reynolds number range until a single particle streak has developed. For both particle types, the single visible particle streak is located near the bisector of the microchannel. Qualitatively, this behavior is consistent with observations of Zhang et al. (2014a) and Ying and Lin (2019). Moreover, the single visible streak of PS-10 particles clearly emerges for $\mathrm{Re_b} \geq 63$, while visible streaks for PS-3 particles already start to disintegrate, i.e. particles are more evenly distributed over the microchannel cross-section. As PS-3 and PS-10 microparticles are focused on spatially separated locations between $63 \leq \mathrm{Re_b} \leq 105$, a good size fractionation performance can be expected in this bulk Reynolds number regime. The focusing behavior of MF-3 and MF-10 particles is shown in Figure 4.3 as a function of the bulk Reynolds number inside the 27th serpentine loop.
For both types of melamine particles, the focusing behavior is similar compared to that of polystyrene particles of the corresponding size. Specifically, MF-3 and MF-10 particles develop two spatially separated visible streaks at low bulk Reynolds numbers that converge into one visible streak surpassing a critical bulk Reynolds

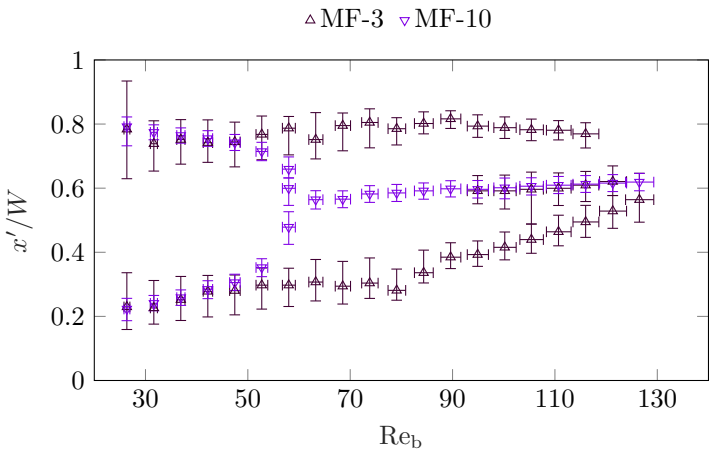

Figure 4.3.: Normalized particle streak locations and widths for MF-3 (▵) and MF-10 (▿) particles as a function of the bulk Reynolds number inside the 27th serpentine loop.

number, as shown in Figure 4.3. During the transition, MF-3 particles develop a third visible particle streak at $x'/W \approx 0.6$ that is located between the two outer visible streaks for $95 \leq \mathrm{Re_b} \leq 116$. Size fractionation of MF-3 and MF-10 particles is promising in the bulk Reynolds number regime of $63 \leq \mathrm{Re_b} \leq 90$, as individual particle streaks are spatially separated here.
The focusing behavior of SiO_2-3 and SiO_2-10 particles is shown in Figure 4.4 as a function of the bulk Reynolds number inside the 27th serpentine loop.
The dependency of the particle streak location on the bulk Reynolds number as shown in Figure 4.4 is similar as for polystyrene and melamine particles. Again, a transition occurs from two visible particle streaks to either one visible particle streak or two merged visible streaks above a critical bulk Reynolds number. Near this critical bulk Reynolds number, SiO_2-3 particles also develop three visible streaks, with two merged visible streaks between the inner microchannel wall and the microchannel bisector. Size fractionation is promising in the bulk Reynolds number regime of $58 \leq \mathrm{Re_b} \leq 111$.
The streak locations of all particle groups considered here do not change significantly after eleven full serpentine loops. This is also true for the streak widths of the larger polystyrene, melamine and silica particles of $d_\mathrm{p} \approx 10\,\mu\mathrm{m}$ diameter. Inside the 27th serpentine loop, particle streak widths are one to two particle diameters. In contrast to this, the streak width decreases with increasing downstream position for smaller polystyrene, melamine and silica particles of $d_\mathrm{p} \approx 3.5\,\mu\mathrm{m}$ diameter. These particles develop visible streaks with widths in the order of magnitude of $\mathcal{O}(10^1)$ particle diameters. Thus, smaller particles tend to develop broader particle

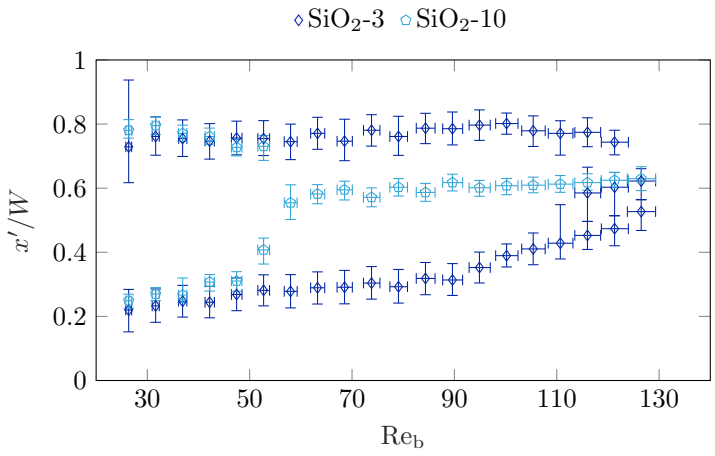

Figure 4.4.: Normalized particle streak locations and widths for SiO_2-3 (◇) and SiO_2-10 (⬠) particles as a function of the bulk Reynolds number inside the 27th serpentine loop.

streaks than larger particles in both, an absolute scale and relative to their particle size. Corresponding data that show the normalized streak locations and widths of polystyrene, melamine and silica particles as a function of the downstream measurement location are given in Appendix A in Figures A.1 to A.3.
Overall, the results that are shown in Figures 4.2 to 4.4 demonstrate that the focusing behavior of micron particles depends on the particle size. This becomes apparent by the fact that there is a transition from two to one visible particle streak that occurs at smaller bulk Reynolds numbers for larger particles. Thus, there exists a bulk Reynolds number range of $63 \leq \mathrm{Re_b} \leq 90$ at which size fraction is promising for polystyrene, melamine and silica particles of $d_\mathrm{p} \approx 3.5\,\mu\mathrm{m}$ and $d_\mathrm{p} \approx 10\,\mu\mathrm{m}$ diameter, respectively. Here, larger particles are focused on one visible streak, while smaller particles still develop two visible particle streaks. At higher bulk Reynolds numbers, streaks of smaller particles also transition towards one visible particle streak. However, these also start to disintegrate. Furthermore, particle streaks are developed after eleven full serpentine loops.

4.1.2. Influence of the particle density on the focusing behavior

The results that are shown in Figures 4.2 to 4.4 indicate that the influence of the particle density on particle streak locations is small at the evaluation location that is depicted with a vertical red arrow in Figure 4.1. Instead, the influence of the particle density on the development of particle streaks is evaluated at the location that is indicated with a horizontal white arrow in Figure 4.1. At this

location, particles have passed two consecutive 90° turns without changing sign of the particle trajectory curvature. Consequently, the contribution of the centrifugal force, which is proportional to the density difference between ambient fluid and particles, is assumed to be largest.
Normalized particle streak center locations and corresponding widths are evaluated inside the 27th serpentine loop. Results are shown as a function of the bulk Reynolds number for polystyrene, melamine and silica particles of $d_p \approx 3.5\,\mu m$ diameter in Figure 4.5(a) and for particles of $d_p \approx 10\,\mu m$ diameter in Figure 4.5(b).

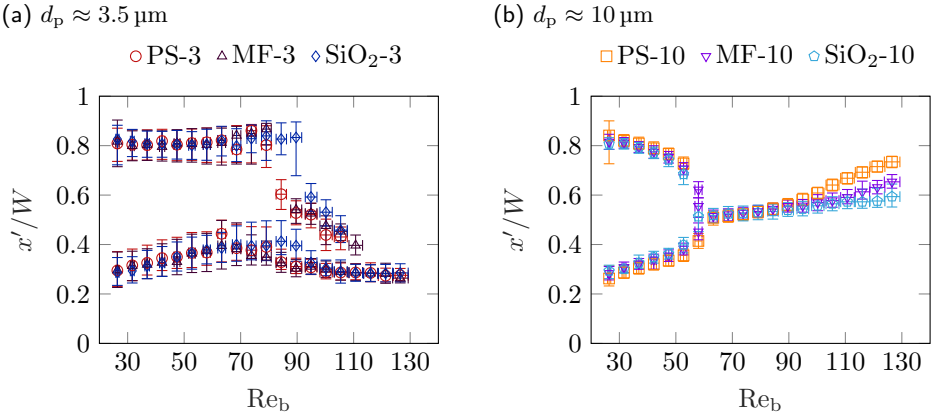

Figure 4.5.: Normalized particle streak locations and widths as a function of the bulk Reynolds number inside the 27th serpentine loop for (a) PS-3 (○), MF-3 (△) and SiO_2-3 (◇) particles and (b) PS-10 (□), MF-10 (▽) and SiO_2-10 (⬠) particles.

For smaller particles no significant influence of the particle density on the visible streak center locations is observed at the considered evaluation location, as shown in Figure 4.5(a). Specifically, the transition from two to one visible particle streak occurs at similar bulk Reynolds numbers, even though the density of melamine and silica particles is 1.4 and 1.8 times larger than for polystyrene particles. Even though silica particles show the tendency to start with the transition process at slightly larger bulk Reynolds numbers than polystyrene and melamine particles, particle trajectories near the inner microchannel wall, i.e. at $0.2 \leq x'/W \leq 0.4$, overlap for all considered particle groups in the investigated bulk Reynolds number range. In this region also single visible particle streaks develop at high bulk Reynolds numbers. Furthermore, the particle streak width does not increase significantly with increasing particle density.
In contrast to smaller particles, polystyrene, melamine and silica particles of $d_p \approx 10\,\mu m$ diameter focus near the microchannel bisector at high bulk Reynolds numbers, as shown in Figure 4.5(b). If the bulk Reynolds number is further

increased after transition to one particle streak, i.e. for $\mathrm{Re_b} \geq 105$, the streak center locations tend to drift towards the outer microchannel wall. Remarkably the degree of lateral drift seems to scale with the particle density. This behavior has not been reported before, but it is of great importance as it opens up the opportunity to realize also density fractionation in serpentine microchannels. In contrast to this, the focusing behavior is rather identical for all considered particle groups for $\mathrm{Re_b} < 105$. Surprisingly, particles with a lower density are driven more strongly towards the outer microchannel wall compared to particles of higher density for $\mathrm{Re_b} \geq 105$. An investigation of the hydrodynamic forces that act on polystyrene particles with $d_\mathrm{p} \approx 10\,\mu\mathrm{m}$ at a bulk Reynolds number where a single visible particle streak develops, shows that the dominant force contributions are the shear-gradient force and the drag force (see chapter 6). An increase of the particle density can be associated with a relative increase of the centrifugal force compared to the shear-gradient force and the drag force. This is assumed to lead to a lateral displacement of denser particles away from the inner microchannel wall when particles pass the 90° turn at $(x, y) = (0\,\mu\mathrm{m}, 0\,\mu\mathrm{m})$. Even a small displacement of particles probably changes the contributions of the shear-gradient force and the drag force after this turn compared to lighter particles of the same size. Such a general change of the force balance is assumed to be the reason that denser particles are located closer to the inner microchannel wall than lighter particles at the considered evaluation location.
Summed up, larger particles generally focus closer to the outer microchannel wall compared to smaller microparticles with the same densities. This offers the opportunity to fractionate particles with regard to their size and additionally large particles also with regard to their density at the same microchannel location and at the same bulk Reynolds number. Thus, this location and bulk Reynolds number regime are promising to realize multi-dimensional particle fractionation.

4.2. Sub-micron polystyrene particles

Sub-micron particles with defined characteristics are of increasing interest as a basis, e.g. for electronic devices or medical applications. Thus, the focusing behavior of sub-micron polystyrene particles in the size range of $0.45\,\mu\mathrm{m} \leq d_\mathrm{p} \leq 0.86\,\mu\mathrm{m}$ is investigated. Pre-processed sample streak images of PS-0.60 particles at $\mathrm{Re_b} = 132$ and $\mathrm{Re_b} = 158$ inside the 27th serpentine loop are shown in Figures 4.6(a) and (b), respectively. These images are characteristic for the focusing behavior of sub-micron particles that are considered in this investigation.
Figure 4.6(a) shows two visible particle streaks that clearly develop for a bulk Reynolds number of $\mathrm{Re_b} = 132$. As a reference, an image without particles has been subtracted from all measurement images of sub-micron particles during the pre-processing procedure. Thus, intensity values that are larger than zero indicate the presence of particles during the recording sequence. From Figure 4.6(a) it

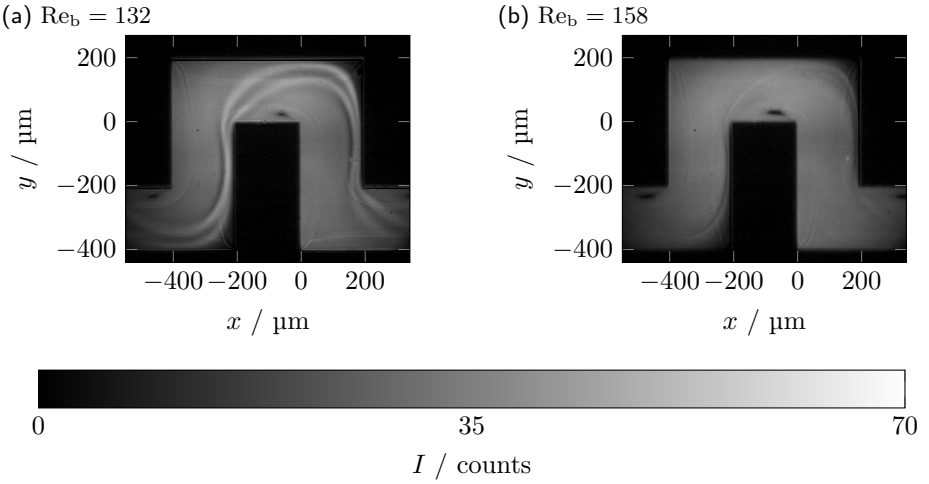

Figure 4.6.: Pre-processed images of PS-0.60 particles inside the 27th serpentine loop at a bulk Reynolds number of (a) $\mathrm{Re_b} = 132$ and (b) $\mathrm{Re_b} = 158$. Flow direction is from right to left in both images.

becomes evident that particles are distributed nearly over the whole microchannel cross-section. The dark region at $-100\,\mu\mathrm{m} \leq x \leq 0\,\mu\mathrm{m}$ and $0\,\mu\mathrm{m} \leq y \leq 50\,\mu\mathrm{m}$ also indicates that this is a region where no particles are present. Numerical and experimental results (see also chapter 6) show that a stationary flow separation occurs in this region. Obviously, particles are driven away from the corresponding vortex center leading to this particle-free region.
Figure 4.6(a) also shows that the particle streak locations differ from that of micron sized particles (see also Figure 4.1). Specifically, both visible particle streaks of sub-micron particles are driven towards the outer microchannel wall for $x \geq 0\,\mu\mathrm{m}$ and $y \geq 0\,\mu\mathrm{m}$, whereas visible streaks of micron sized particles are distributed rather symmetrical relative to the microchannel bisector. This is assumed to be caused by a region of high flow velocities near the inner microchannel wall at $(x, y) = (0\,\mu\mathrm{m}, 0\,\mu\mathrm{m})$, resulting in large flow velocity gradients that drive particles towards the outer microchannel wall. As the bulk Reynolds number for sub-micron particles is significantly larger than for micron particles, the flow gradients along the microchannel cross-section are also increasing (see also chapter 6).
A further increase of the bulk Reynolds number drives the inner visible particle streak towards the outer visible streak until both disintegrate, as shown in Figure 4.6(b). This is surprising as sub-micron particles are observed to develop a single visible streak in asymmetric serpentine microchannels (L. Wang and Dandy, 2017). However, disintegration is assumed to result from the fact that the Dean drag force is becoming dominant at increased bulk Reynolds numbers, which is

known to lead to particle mixing in curved microchannels (Di Carlo et al., 2008). The normalized particle streak center locations and widths of sub-micron particles are evaluated inside the 27th serpentine loop and midway of the horizontal serpentine section at $x = -100\,\mu m$ (see also vertical red arrow in Figure 4.1). Figure 4.7 shows these particle streak characteristics as a function of the bulk Reynolds number.

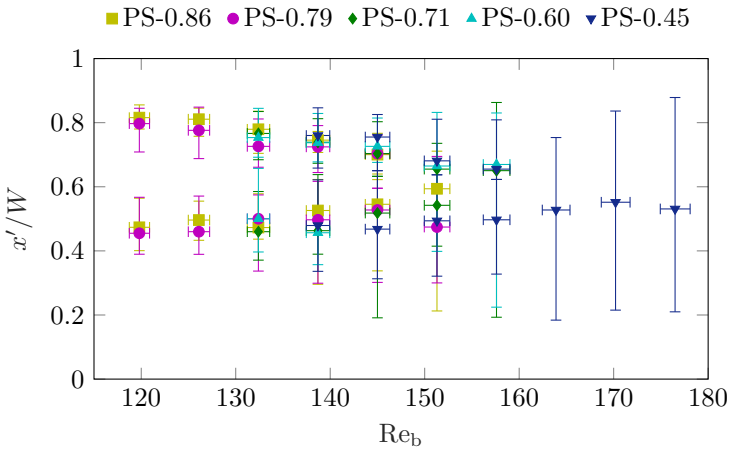

Figure 4.7.: Normalized particle streak locations and widths for PS-0.86 (■), PS-0.79 (●), PS-0.71 (♦), PS-0.60 (▲) and PS-0.45 (▼) particles as a function of the bulk Reynolds number inside the 27th serpentine loop.

For all considered sub-micron particles considered in the present study, a development of two visible particle streaks is observed at specific bulk Reynolds numbers. When the bulk Reynolds number increases further, a transition takes place at which streak centers of all considered sub-micron particles first approach each other and then disintegrate. As particles are distributed over the whole microchannel cross-section in this disintegration state, this results in a rather random peak detection at the location of the highest intensity value and large streak widths. The beginning of such a disintegration behavior was also observed for PS-3 particles at high bulk Reynolds numbers, as described in section 4.1.1.
Overall, sub-micron particles develop streaks with small spatial distances and large widths. Furthermore, even inside the 27th serpentine loop, particles are distributed nearly over the whole microchannel cross-section at all considered bulk Reynolds numbers. In contrast to micron particles, sub-micron particles do not develop a clear single visible streak, but disintegrate with increasing bulk Reynolds numbers. This indicates that a size fractionation of sub-micron particles with high purity of one fraction is difficult to realize.

4.3. Conclusion

The focusing behavior of micron and sub-micron particles in the sharp-corner serpentine microchannel is investigated by means of long-time exposure fluorescence images. It is demonstrated that polystyrene, melamine and silica particles with diameters of $d_\mathrm{p} \approx 3.5\,\mu\mathrm{m}$ and $d_\mathrm{p} \approx 10\,\mu\mathrm{m}$ develop two visible particle streaks below a critical bulk Reynolds number. These transition to one visible particle streak above this critical bulk Reynolds number. Whilst this transition process is dependent on the particle size, it is rather independent on the particle density within the considered size and density range. However, the particle streak locations are dependent on the particle size, as well as on the density, if particle sizes and bulk Reynolds numbers are large. Consequently, a bulk Reynolds number regime is identified at $63 \leq \mathrm{Re_b} \leq 90$ at which a size fractionation with a high purity is promising for all three particle materials. Density fractionation is promising for particles of $d_\mathrm{p} \approx 10\,\mu\mathrm{m}$ diameter for $\mathrm{Re_b} \geq 105$. Overall, the current observations indicate for the first time that a multi-dimensional fractionation may be possible. Additionally, sub-micron polystyrene particles of $0.45\,\mu\mathrm{m} \leq d_\mathrm{p} \leq 0.86\,\mu\mathrm{m}$ diameter also develop two particle streaks below a critical bulk Reynolds number. In contrast to micron particles, it has been shown that an increase of the bulk Reynolds number rather leads to the disintegration of particle streaks than to a development of a single visible particle streak for sub-micron particles. As sub-micron particles of different sizes develop no spatially separated trajectories in the investigated bulk Reynolds number regime, the possibilities for a size fractionation of sub-micron particles with high purity are limited.

5. On the 3D distribution of microparticles in a sharp-corner serpentine microchannel[1]

The previous chapter revealed a bulk Reynolds number regime that is promising for the realization of particle size fractionation. In this chapter, the size fractionation performance is investigated for polystyrene particles of 3.55 µm (PS-3) and 9.89 µm diameter (PS-10) in a sharp-corner serpentine microchannel of cross-sectional aspect ratio $H/W = 0.25$. Experimental results are obtained through Astigmatism Particle Tracking Velocimetry (APTV) measurements, from which three-dimensional particle distributions are reconstructed for bulk Reynolds numbers between $67 \leq \mathrm{Re_b} \leq 100$. Additionally, APTV measurements are performed utilizing melamine particles with 9.84 µm diameter (MF-10) in the same bulk Reynolds number regime. As melamine particles have a density that is approximately 1.4 times larger than the density of polystyrene particles (see also Table 3.2), the possibility to realize a density fractionation of melamine and polystyrene particles of $d_\mathrm{p} \approx 10\,\mu\mathrm{m}$ along the microchannel height is explored.
To realize microparticle fractionation, each particle group has to develop trajectories that are spatially separated across the flow such that each particle group may be separated through a flow branching downstream the fractionation channel. Thus, to validate the capability of the serpentine microchannel to fractionate particles according to size and density, three-dimensional particle distributions are determined in a first step. Afterwards, a virtual flow branching is performed, i.e. the serpentine microchannel is divided virtually into individual segments in the post-processing and fractionation efficiencies are analyzed with respect to varying virtual partitioning wall positions. Size fractionation results are analyzed in section 5.1, a discussion with regard to density fractionation is provided in section 5.2.

[1] Parts of this section are published in Blahout et al. (2020), used under CC BY 4.0. The original contents have been edited and/or extended for this work.

5.1. Influence of the particle size

An APTV approach is utilized to reconstruct three-dimensional distributions of polystyrene particles with diameters of 3.55 µm (PS-3) and 9.89 µm (PS-10). Figure 5.1 shows exemplary distributions of both particle groups at a bulk Reynolds number of $\mathrm{Re_b} = 73$ inside the 25th serpentine loop (see also Figure 3.3 for the exact measurement location). As results that are obtained from long-exposure measurements show no significant change of the particle trajectory characteristics after eleven serpentine loops, the results that are shown here are considered to be independent from the downstream measurement location (see also chapter 4 and Appendix A). The in- and outflow direction is in negative x-direction and the channel walls are sketched with black dashed lines. The region of interest for which the size fractionation performance is investigated, is indicated with blue dashed lines. It shall be noted that Figure 5.1 shows a superposition of both particle fractions including all reconstructed particle centroid positions of a time series of 1500 double-frame images. Both particle fractions are recorded simultaneously.

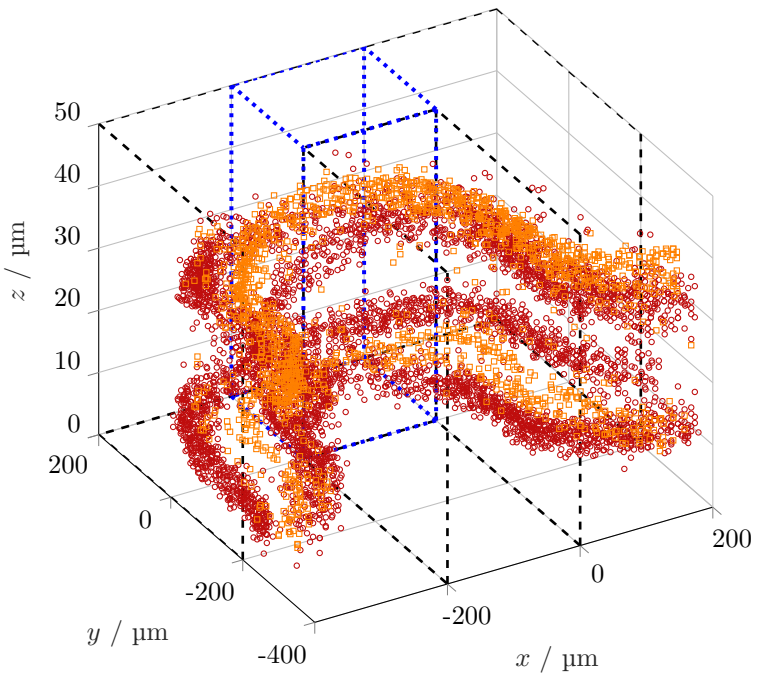

Figure 5.1.: Measured particle centroid positions of PS-3 (○) and PS-10 (□) particles at $\mathrm{Re_b} = 73$. The particle distribution inside the flow volume between $-200 < x < 0$ and $0 < y < 200$ (sketched in blue) is analyzed.

As shown in Figure 5.1, each particle fraction forms spatially separated equilibrium trajectories. In contrast to the findings of Zhang et al. (2014b) and Zhang et al. (2014a) as well as to the results of chapter 4 that are obtained by fluorescence imaging to detect in-plane particle trajectories, the three-dimensional reconstruction reveals that particle separation takes also place over the microchannel height (z-direction) leading to four and two equilibrium positions for PS-3 and PS-10 particles, respectively. The particle trajectory configuration with four trajectories is henceforth referred to as 2×2 trajectory configuration. Consequently, the particle trajectory configuration with two trajectories that are located above each other is henceforth referred to as 1×2 trajectory configuration. Furthermore, a slight height variation between in-plane equilibrium trajectories of PS-3 particles becomes visible.
The fractionation performance is analyzed in the region of interest that is sketched with blue dashed lines in Figure 5.1. The spatial distribution of particles at different bulk Reynolds numbers is provided in Figures 5.2(a) to (f). An increase of the bulk Reynolds number from $\mathrm{Re_b} = 67$ to $\mathrm{Re_b} = 100$ reduces the spread of the equilibrium trajectories of PS-10 particles in y-direction. In contrast to this, PS-3 particles stay in a 2×2 trajectory configuration up to a bulk Reynolds number of $\mathrm{Re_b} = 87$ with centroid positions of $y/W \approx 0.33$ and $y/W \approx 0.8$, respectively. Therefore, they are located closer to the channel side walls compared to the larger particles. At $\mathrm{Re_b} = 100$, PS-3 and PS-10 particles are not significantly spatially separated over the channel width anymore as PS-3 particle bands are merged, spanning a region of $0.2 < y/W < 0.8$. It shall be noted that all equilibrium trajectories are displaced towards the bottom of the channel.
To evaluate the fractionation performance, the cross-sectional particle distributions of Figures 5.2(a) to (f) are virtually divided into three segments, indicated by two vertical black lines. These virtual partitioning walls are placed symmetrically around $y/W = 0.5$ at different distances δ_y to the channel side walls, as denoted in Figure 5.2(a). Here δ_y is varied between $0.05 < \delta_\mathrm{y} < 0.45$ in steps of 0.025. This corresponds to a step size of 5 µm. In each of these three segments, particle concentrations of both fractions are evaluated by means of a separation degree $T = N_{\mathrm{PS-10}}^2 / \left(N_{\mathrm{PS-10}}^2 + N_{\mathrm{PS-3}}^2\right)$ (Stieß, 2009). Here, N_i denotes the number of particles of fraction i inside the corresponding evaluation volume. T becomes zero in regions, where only PS-3 particles are located and one if only PS-10 particles are included in a segment. Thus, three values for T are obtained, i.e. one for each segment. The difference in two neighbouring segments is defined as selectivity $\kappa_\mathrm{y} = |T_{\mathrm{i+1}} - T_\mathrm{i}|$. In the following, the selectivity for different partitioning wall positions δ_y and bulk Reynolds numbers $\mathrm{Re_b}$ is evaluated. κ_y reaches one if both particle fractions are completely separated. Due to the fact that particles are almost symmetrically distributed around $y/W = 0.5$, both values for κ_y are averaged and mean values $\bar{\kappa}_\mathrm{y}$ are plotted as a function of the bulk Reynolds number $\mathrm{Re_b}$ and the partitioning wall position δ_y in Figure 5.3(a). Here, red crosses indicate $\bar{\kappa}_\mathrm{y}$ values that are calculated for the particle distributions and partitioning wall positions

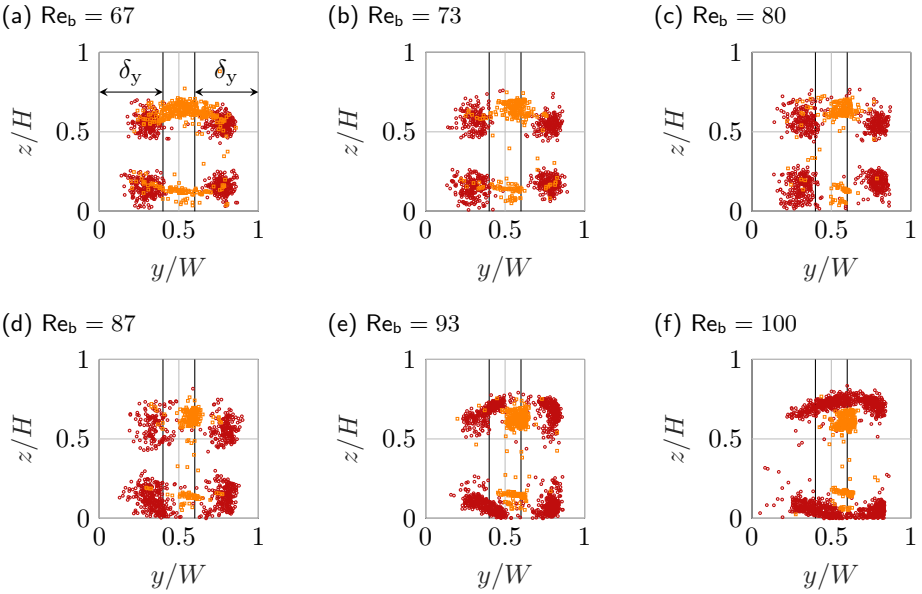

Figure 5.2.: Projected view of particle positions of PS-3 (○) and PS-10 (□) particles inside the region of interest. The size fractionation performance is investigated for segments, which divide the test volume at $y/W = \delta_y$, as well as $y/W = 1 - \delta_y$. Here, $\delta_y = 0.4$, which corresponds to the optimum size fractionation performance at Re$_b$ = 73. Results are shown for bulk Reynolds numbers of (a) Re$_b$ = 67, (b) Re$_b$ = 73, (c) Re$_b$ = 80, (d) Re$_b$ = 87, (e) Re$_b$ = 93 and (f) Re$_b$ = 100

that are shown in Figures 5.2(a) to (f).
From this representation, a maximum mean selectivity of $\bar{\kappa}_y = (0.981 \pm 0.010)$ is found for Re$_b$ = 73 and $\delta_y = 0.4$, as also indicated with a bold red cross in Figure 5.3(a). This situation is displayed in Figure 5.2(b). Here, PS-3 particles are located in the lateral channel sections, i.e. at $0 < y/W \leq 0.4$ and $0.6 < y/W \leq 1$, respectively, while the majority of PS-10 particles is located in the channels middle section, i.e. at $0.4 < y/W \leq 0.6$. The corresponding values for T are shown in Figure 5.3(b). As already expected from the corresponding particle distribution shown in Figure 5.3(b), T values switch from a low level of $T_1 = 0.003$ at $0 < y/W \leq 0.4$ to a high value of $T_2 = 0.994$ at $0.4 < y/W \leq 0.6$ and vice versa ($T_3 = 0.023$ at $0.6 < y/W \leq 1$). This corresponds to a nearly ideal separation situation.
Velocity measurements at this bulk Reynolds number by means of APTV reveal that PS-3 particles flow at a median speed of $(1.25 \pm 0.21)\,\mathrm{m\,s^{-1}}$. This is similar

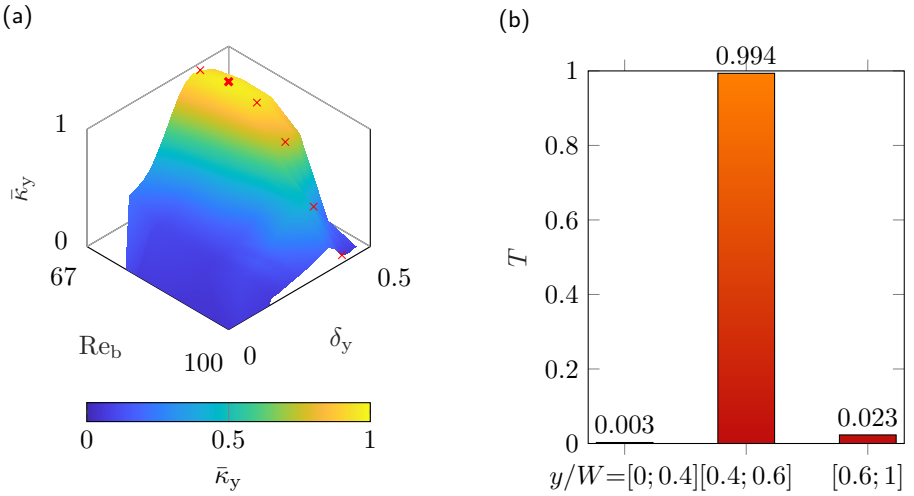

Figure 5.3.: (a) Mean selectivities $\bar{\kappa}_y$ of PS-3 and PS-10 particles as a function of the bulk Reynolds number $\mathrm{Re_b}$ and the partitioning wall position δ_y. The maximum mean selectivity of $\bar{\kappa}_y = (0.981 \pm 0.010)$ is reached at $\mathrm{Re_b} = 73$ and $\delta_y = 0.4$. Red crosses show the fractionation performances for the particle distributions and partitioning wall positions shown in Figures 5.2(a) to (f); (b) Separation degree T in three segments at a bulk Reynolds number of $\mathrm{Re_b} = 73$ and a partitioning wall position of $\delta_y = 0.4$

to the median velocity of PS-10 particles of $(1.27 \pm 0.10)\,\mathrm{m\,s^{-1}}$. Interestingly, both particle groups appear to be faster than the fluid bulk velocity of $u_b = 0.92\,\mathrm{m\,s^{-1}}$. A further investigation of PS-10 particles and PS particles of $(7.76 \pm 0.12)\,\mu\mathrm{m}$ diameter revealed that if the bulk Reynolds number, i.e. the volume flow rate in the experiment, can be controlled accurately enough, size fractionation can be realized even for a size difference as small as approximately $2\,\mu\mathrm{m}$. Specifically, a mean selectivity of $\bar{\kappa}_y \approx 0.9$ is obtained at a bulk Reynolds number of $\mathrm{Re_b} = 68$ for the particle groups described above. Higher selectivities could not be reached here, because the transition process from a 2×2 towards a 1×2 trajectory configuration occurs at similar bulk Reynolds numbers for both fractions.

5.2. Influence of the particle density

The sharp-corner serpentine microchannel is tested with regard to its capability to separate particles with the same size and different densities along the microchannel height in the bulk Reynolds number regime of $67 \leq \mathrm{Re_b} \leq 100$. In particular, PS-10 and MF-10 particles with densities of $\rho_{PS} = 1050\,\mathrm{kg\,m^{-3}}$ and $\rho_{MF} = 1510\,\mathrm{kg\,m^{-3}}$

are chosen. It is investigated, if corresponding particle trajectories develop at spatially separated height positions inside the serpentine microchannel. This would add an additional possibility for density fractionation inside sharp-corner serpentine microchannels, besides the possibility for an in-plane density fractionation of such particles at high bulk Reynolds numbers (see also section 4.1.2). Particle trajectories of both particle groups are recorded sequentially, while in both recordings PS-3 particles are included as a reference. Thus, resulting equilibrium trajectories of both measurements are superimposed for the same bulk Reynolds number. Particle trajectories at $\mathrm{Re_b} = 73$ are shown in Figure 5.4.

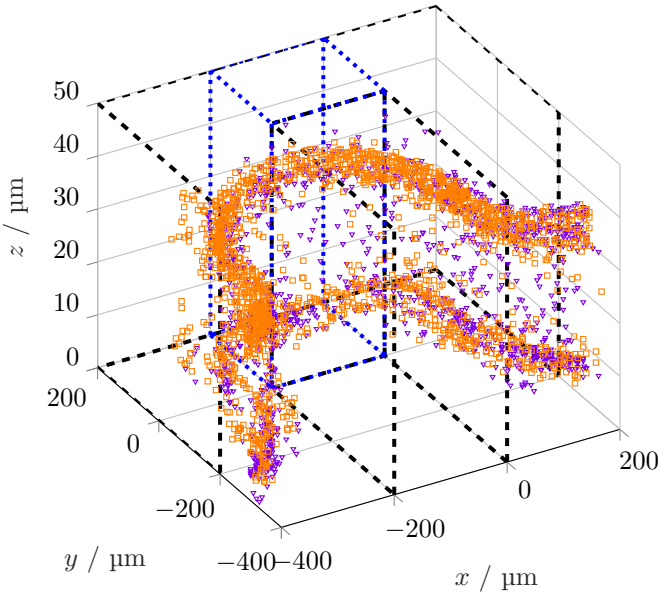

Figure 5.4.: Scatter plot of the three-dimensional distribution of PS-10 (□) and MF-10 (▽) particles at a bulk Reynolds number of $\mathrm{Re_b} = 73$. The density fractionation performance along the microchannel height is investigated inside the flow volume between $-200 < x < 0$ and $0 < y < 200$ (sketched in blue)

Obviously both, PS-10 and MF-10 particles, already follow a 1×2 trajectory configuration. In contrast to the size fractionation results, where PS-3 and PS-10 particles develop spatially separated in-plane equilibrium trajectories, PS-10 and MF-10 particles seem to follow identical trajectories. Figures 5.5(a) to (f) display particle distributions inside the evaluation volume that is sketched in blue in Figure 5.4 for bulk Reynolds numbers between $67 \leq \mathrm{Re_b} \leq 100$.
Here, both particle groups focus on a 1×2 trajectory configuration at all considered bulk Reynolds numbers. Both particle groups are located at $y/W \approx 0.6$ as well as

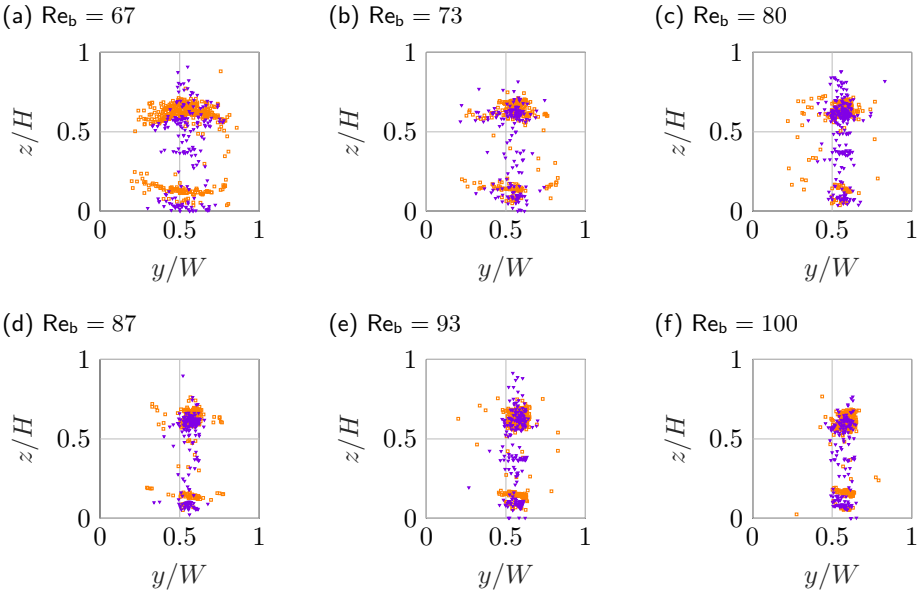

Figure 5.5.: Projected view of PS-10 (□) and MF-10 (▽) particles inside a 200 µm volume as indicated in blue in Figure 5.4. Results are shown for bulk Reynolds numbers of (a) $\mathrm{Re_b} = 67$, (b) $\mathrm{Re_b} = 73$, (c) $\mathrm{Re_b} = 80$, (d) $\mathrm{Re_b} = 87$, (e) $\mathrm{Re_b} = 93$ and (f) $\mathrm{Re_b} = 100$

at $z/H \approx 0.13$ and $z/H \approx 0.63$, respectively. Additionally, a minority of particles is detected between these trajectories at $z/H \approx 0.4$. However, as this is true for both particle groups, an increase of the particle density of $\rho_{\text{MF-10}}/\rho_{\text{PS-10}} = 1.4$ obviously is not sufficient to force particles on trajectories that are spatially separated along the microchannel height. Thus, no possibility for an out-of plane density fractionation is present for the considered particles in the considered bulk Reynolds number regime.

5.3. Conclusion

In this chapter, the size fractionation performance of a sharp-corner serpentine microchannel is determined for PS-3 and PS-10 particles. Additionally, the possibility for density fractionation along the microchannel height is tested for PS-10 and MF-10 particles. For this purpose, particle trajectories in dilute suspension flows are recorded at different bulk Reynolds numbers inside the 25th serpentine loop. An Astigmatism Particle Tracking Velocimetry (APTV) algorithm is utilized to reconstruct three-dimensional particle positions.

Distinct equilibrium trajectories are observed for all investigated particle fractions. While PS-3 particles undergo a transition from a 2×2 trajectory configuration at $\mathrm{Re_b} = 67$ towards a 1×2 trajectory configuration that is spread over the microchannel width at $\mathrm{Re_b} = 100$, PS-10 and MF-10 particles stay in a 1×2 configuration that narrows with increasing bulk Reynolds number. Thus, size fractionation is achieved, due to the spatial separation of differently sized polystyrene particles. Furthermore, it was found that equilibrium trajectories of particles with equal size but different densities do not develop significantly spatially separated equilibrium trajectories within the investigated parameter range.
The size fractionation performance is evaluated in terms of the separation degree and the selectivity, calculated over the microchannel width. For investigated PS-3 and PS-10 particles, a maximum mean selectivity of $\bar{\kappa}_\mathrm{y} = (0.981 \pm 0.010)$ is found at $\mathrm{Re_b} = 73$ utilizing two vertical partitioning walls located at $y/W = 0.4$ and $y/W = 0.6$.
Overall, in the present study, the three-dimensional distribution of microparticle equilibrium trajectories is investigated to perform a quantitative evaluation of the size fractionation performance in a sharp-corner serpentine microchannel for the first time. With this methodology, new means of size and density fractionation may be explored more easily in the future.

6. On the forces acting on particles in a sharp-corner serpentine microchannel flow

The forces that hold particles on their respective equilibrium trajectories inside the sharp-corner serpentine microchannel are investigated. With this, the present thesis aims to deepen the understanding of driving forces and figure out the dominant forces responsible for the lateral motion of suspended particles. For this purpose, numerical simulations of polystyrene particles of 3.55 µm (PS-3) and 9.89 µm (PS-10) diameter at different bulk Reynolds numbers are analyzed. Simulated particle trajectories are compared to experimental results, first. Afterwards, exemplary force distributions that act on a single particle while flowing through one full serpentine loop are investigated in detail. Simulated trajectories of PS-10 particles are investigated in section 6.1. An analysis of simulated trajectories of PS-3 particles is provided in section 6.2.

6.1. Fully coupled simulations of PS-10 particles

It shall be noted that the simulations on which the results of this section are based on are performed by our partner in the DFG priority program 2045, S. R. Reinecke at the Technische Universität Berlin. Results are kindly provided for further analysis. Simulations are performed by a coupled Lattice Boltzmann Method-Discrete Element Method code in accordance to Reinecke et al. (2021).
To gain a deeper understanding of the actual force balances after the transition towards a 1×2 trajectory configuration, simulations are performed at similar bulk Reynolds numbers as in the experiments to enable a comparison of results. This comparison and henceforth the resulting force balances are presented and discussed in the following.
Numerical and experimental trajectories of PS-10 particles are compared to each other at similar bulk Reynolds numbers. Figures 6.1(a) and (c) show numerically derived particle trajectories at $\mathrm{Re_b} = 33$ and $\mathrm{Re_b} = 100$ approximately 15 serpentine loops downstream of the inlet. Here, particle trajectories are fully converged as also confirmed by experimental investigations where particle trajectories stay constant after 11 serpentine loops (see also chapter 4). Corresponding experimental

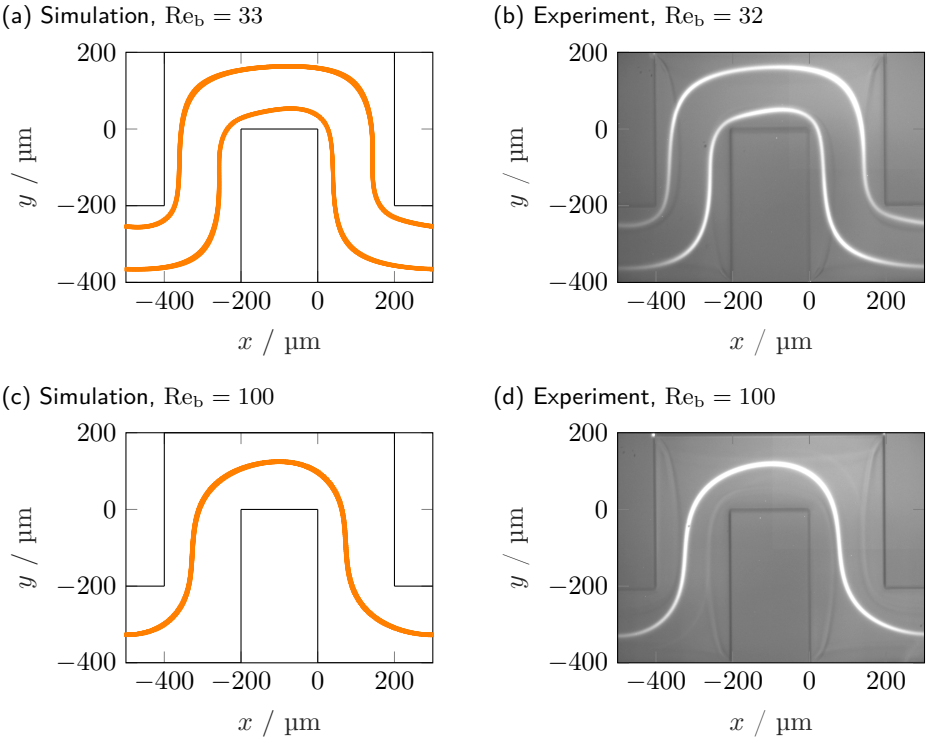

Figure 6.1.: Trajectories of PS-10 particles obtained from (a) a simulation at $\mathrm{Re_b} = 33$; (b) a long-exposure measurement at $\mathrm{Re_b} = 32$; (c) a simulation at $\mathrm{Re_b} = 100$ and (d) a long-exposure measurement at $\mathrm{Re_b} = 100$. Flow direction is from right to left.

results at bulk Reynolds numbers of $\mathrm{Re_b} = 32$ and $\mathrm{Re_b} = 100$ are captured inside the 27th serpentine loop and are shown in Figures 6.1(b) and (d).
The numerical results show a 2×2 configuration of particle trajectories at a bulk Reynolds number of $\mathrm{Re_b} = 33$. The locations of the trajectories that are visible in the x-y-plane in Figure 6.1(a) agree well with experimental results that are obtained from long-exposure measurements. Specifically, at $x = -100\,\mu\mathrm{m}$, the simulated particle trajectories are located at $x'/W \approx 0.25$ and $x'/W \approx 0.81$ at a bulk Reynolds number of $\mathrm{Re_b} = 33$. This is within the particle streak width that is determined experimentally in chapter 4 for this particle type and bulk Reynolds number. Furthermore, simulated particle trajectories develop at $z/H \approx 0.23$ and $z/H \approx 0.69$. An increase of the bulk Reynolds number to $\mathrm{Re_b} = 100$ leads to the development of a 1×2 configuration of particle trajectories in the experiments, which can be also captured well by the fully coupled numerical simulations. This

is visible from the trajectories shown in Figures 6.1(c) and (d). Simulated trajectories are located at in-plane positions of $x'/W \approx 0.59$ at $x = -100\,\mu\text{m}$ and at out-of-plane positions of $z/H \approx 0.25$ and $z/H \approx 0.68$, respectively, and are similar to those of experimentally determined trajectories.
Exemplary normal force distributions for a particle flowing at a bulk Reynolds number of $\text{Re}_\text{b} = 33$, i.e. in a 2×2 configuration, along the lower, inner trajectory through one serpentine loop is shown as a function of the normalized restitution time in Figure 6.2. Normal force contributions refer here to the direction normal to the particle main flow direction and parallel to the x-y-plane of the microchannel coordinate system (see also Figure 3.11). Considered are the normal centrifugal $F_{\text{c,n}}$, the normal drag $F_{\text{d,n}}$, the normal shear-gradient $F_{\text{s,n}}$ and the normal Saffman force $F_{\text{Saffman,n}}$. Additionally, the sum of the previously described normal force contributions $F_{\text{sum,n}}$ is plotted. The normalized restitution time is scaled such that it is $t/t_\text{ref} = 0$ when the particle is located at the inlet and $t/t_\text{ref} = 1$ when the particle is located at the outlet of the flow domain.

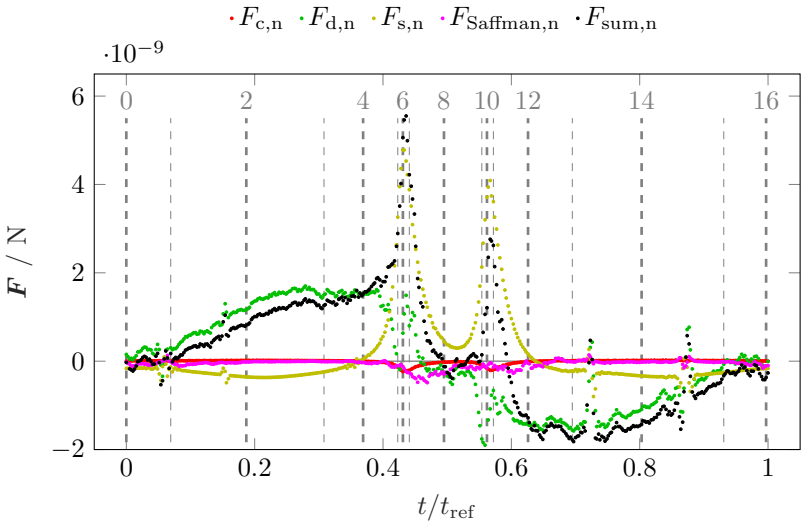

Figure 6.2.: Normal force distributions as a function of the normalized restitution time of a PS-10 particle that flows along the lower, inner trajectory through one serpentine loop at a bulk Reynolds number of $\text{Re}_\text{b} = 33$. Numbers above the vertical dashed lines indicate the position of the cross-sectional planes that are shown in Figure 6.3

Gray vertical dashed lines in Figure 6.2 indicate the instant at which the particle passes the corresponding cross-sectional plane, as shown in Figure 6.3. The trajectory of the considered particle is plotted here for visualization.
A comparison of the individual force contributions plotted in Figure 6.2 demon-

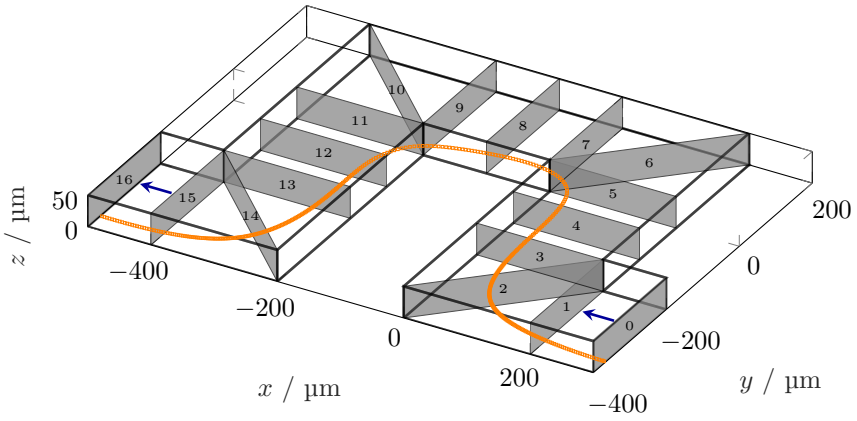

Figure 6.3.: Locations of evaluation planes inside one serpentine loop and trajectory of the considered PS-10 particle at $\mathrm{Re_b} = 33$.

strates that the normal drag force and the normal shear-gradient force are dominant for the particle motion. Compared to these, the normal centrifugal force and the normal Saffman force are one to two orders of magnitude smaller. However, as the normal centrifugal force scales with the density difference between liquid and particles and thus is assumed to become relevant for particles of larger densities, its characteristic force distribution is also discussed qualitatively additionally to the dominant normal drag and shear-gradient force distributions in the following.
Figure 6.2 reveals that particles following a lower, inner particle trajectory experience large shear-gradient forces when passing planes 6 and 10. Here, particles flow at a small orbit around the 90° turns at planes 5 to 7 and 9 to 11, respectively. Thus, particles pass the region where the largest flow velocities are present.
The normal shear-gradient force distribution can be divided into three characteristic regions. The first region ranges from plane 0 to plane 4, the second from plane 4 to plane 12 and the third from plane 12 to plane 16. It shall be noted that the force distribution in the third region is similar to that in the first region due to the periodicity of the serpentine flow. Considering the previous definitions, the three individual regions are divided near the location at which the curvature of the particle trajectory changes sign. Here, the normal shear-gradient force approaches zero.
In the first region, from plane 0 to 4, the considered particle flows at a large orbit around the 90° turn between planes 1 and 3. Consequently, the normal centrifugal force is small in this region. Considering the particle related coordinate system (see also Figure 3.11), the positive sign of the centrifugal force in this region indicates that this force contribution points towards the inner microchannel wall, i.e. to the left relative to the particle main flow direction. This is in agreement with the

expectations, as the particle moves on a right-hand curve. In contrast to this, the shear-gradient force is negative, but also relatively small between planes 0 and 4. This indicates that the shear-gradient normal to the particle main flow direction is negative and points towards the outer microchannel wall, i.e. to the right relative to the particle main flow direction.
In the second region, from plane 4 to 12, the particle flows around two consecutive 90° turns at a smaller orbit. Consequently, the normal centrifugal force develops two peaks inside of these 90° turns. The negative sign of the normal centrifugal force indicates that it points towards the outer microchannel wall, which again agrees with the expectation on the basis of the particle trajectory curvature. Also inside these 90° turns, the normal shear-gradient force develops two distinct peaks, but with a positive sign. Thus, the normal shear-gradient force in the vicinity of the considered particle points towards the inner microchannel wall, here. The magnitude of the normal shear-gradient force peaks is one order of magnitude larger than the normal centrifugal force. However, an increase of the normal centrifugal force magnitude can be expected for increasing particle densities.
In the third region, from plane 12 to 16, the normal centrifugal force and the normal shear-gradient force are similar to their respective distribution in the first region. This is due to the fact that the considered particle again moves at a larger orbit around the last 90° turn and the periodicity of the serpentine flow.
Interestingly, the distribution of the normal drag force can be divided into two, almost symmetric regions between planes 0 and 8 as well as between planes 8 and 16. Thus, the sign of the normal drag force changes near the location where the considered particle has exactly passed half a serpentine loop. The normal drag force points towards the inner microchannel wall in the first region and generally towards the outer microchannel wall in the second region. This is assumed to be caused by the characteristics of the liquid flow field. An analysis of the cross-sectional flow field at the individual evaluation planes revealed that the lateral liquid flow velocity points towards the inner microchannel wall, i.e. in the same direction as the normal drag force, between planes 2 and 5. A positive normal drag force indicates that this lateral liquid flow velocity is larger than the corresponding particle velocity. This is reasonable due to the larger inertia of suspended particles. Between planes 5 and 11, the normal shear-gradient force also becomes dominant. Thus, an interpretation of an isolated force contribution based on the particle dynamics is difficult. In the second region between planes 11 and 13 the cross-sectional flow field generally points towards the outer microchannel wall. Obviously, the liquid flow velocities are larger than the corresponding particle velocities in this region, as the normal drag force also points towards the outer microchannel wall here.
The normal centrifugal force, the normal drag force, the normal shear-gradient force and the normal Saffman force are summed in every time step. The resulting sum of normal forces $F_{\mathrm{sum,n}}$ is also plotted in Figure 6.2. The sum of the considered normal forces is dominated between planes 0 and 4 by the normal drag force. Between planes 4 and 12, the sum of normal forces is mainly characterized by the

normal shear-gradient force. Thus, also the sum of normal forces develops two distinct peaks in this region. In the third region, between planes 12 and 16, the summed normal force is dominated by the normal drag force again. Consequently, it is generally negative, i.e. pointing away from the inner microchannel wall in this region.

The integral over one serpentine loop of the summed normal force leads to a normal net force that is one order of magnitude smaller than the corresponding maximum normal force value near plane 6 and of positive sign. The main contribution of this non-zero normal net force is the normal shear-gradient force. A non-zero and positive normal net force indicates that another force contribution that points away from the inner microchannel wall may not be considered here. It is anticipated that this missing force contribution is the wall lift force. This force component arises from the hydrodynamic interactions of the disturbance flow that is caused by the presence of a particle with microchannel walls and usually drives particles away from a wall. In the past, this force contribution was found to be e.g. responsible for the particle equilibrium trajectories in a tube flow that were observed by Segré and Silberberg (1962a) and Segré and Silberberg (1962b). Although analytical and empirical solutions exist (Asmolov, 1999; Zeng et al., 2005), this force contribution is not considered here as the known solutions are valid only for straight channel walls. An adaption of existing solutions for strongly curved channel walls or even sharp corner flows does not exist up to date. However, due to the fully coupled simulation approach, such a wall lift force component is considered during the particle simulations.

An increase of the bulk Reynolds number leads to the development of a 1×2 configuration of particle trajectories, as shown in Figures 6.1(c) and (d). The path of an exemplary particle that flows along the lower trajectory at $\mathrm{Re_b} = 100$ is shown in Figure 6.4 together with the locations of the individual evaluation planes. The corresponding, exemplary force distributions for this particle as a function of the normalized restitution time are shown in Figure 6.5.

Again, the normal centrifugal force and the normal Saffman force are significantly smaller than the normal shear-gradient force and the normal drag force. In contrast to the previously discussed normal force distributions, the normal centrifugal force and the normal shear-gradient force develop no distinct peaks inside the 90° turns at planes 6 and 10. This is a result of the larger orbit at which the particle flows inside the individual 90° turns, which also leads to a larger distance to the regions of highest liquid flow velocities near the inner microchannel wall near planes 6 and 10. A larger distance to the regions of high liquid flow velocities leads to a reduced shear-gradient in the vicinity of the considered particle. Due to the larger orbit of the particle trajectory, the normal centrifugal force is reduced, as well. However, for the normal shear-gradient force, three characteristic regions with a negative contribution from plane 0 to 4, a positive contribution from plane 4 to 12 and a negative contribution from plane 12 to 16 can be determined, again.

For the normal drag force, two characteristic regions with a generally positive

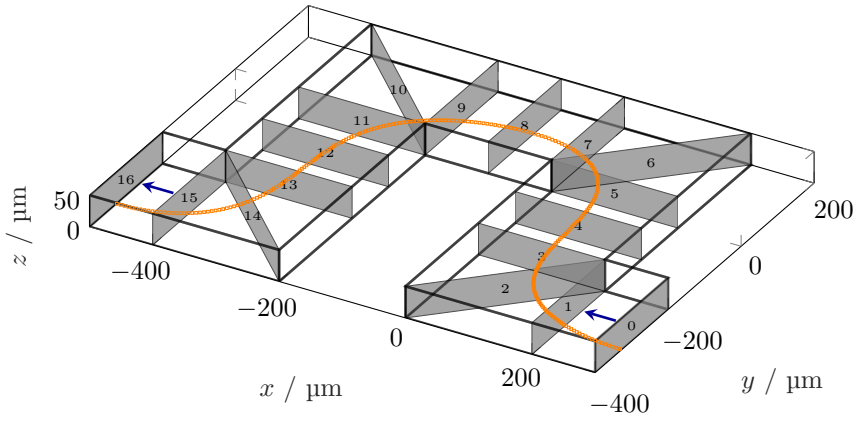

Figure 6.4.: Locations of evaluation planes inside one serpentine loop and trajectory of the considered PS-10 particle at $\mathrm{Re_b} = 100$.

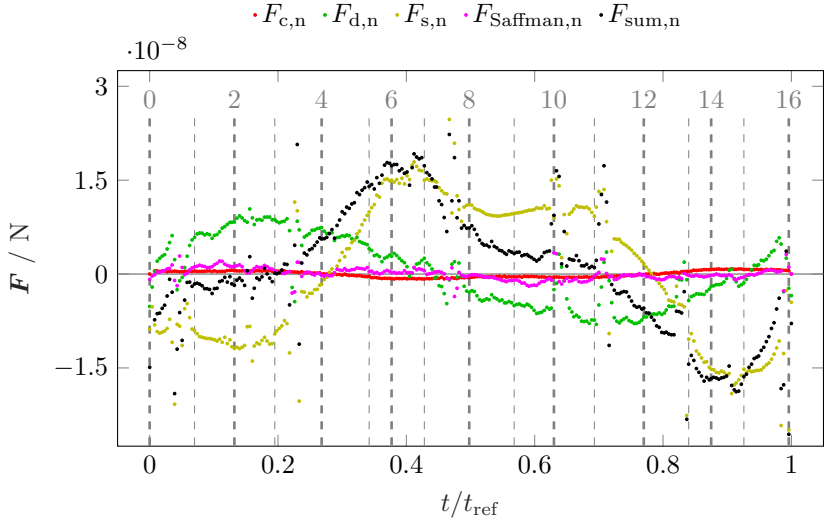

Figure 6.5.: Normal force distributions as a function of the normalized restitution time of a PS-10 particle that flows along the lower trajectory through one serpentine loop at a bulk Reynolds number of $\mathrm{Re_b} = 100$. Numbers above the vertical dashed lines indicate the position of the cross-sectional planes that are shown in Figure 6.4.

contribution between planes 0 and 8 and a generally negative contribution between planes 8 and 16 can be observed for the considered particle. The normal drag force

is in the same order of magnitude as the normal shear-gradient lift force.
The integrated sum of normal forces of the considered particle in the 1×2 configuration is positive and two orders of magnitude smaller than the maximum values of the individual force contributions. In contrast to the investigation of the results at a bulk Reynolds number of $\mathrm{Re_b} = 33$, the integrated normal drag force appears to be dominant for a non-zero normal net force at $\mathrm{Re_b} = 100$. However, as the relative deviation of the normal net force decreases with increasing bulk Reynolds number and thus with an increasing distance of the considered particle to the microchannel walls, this is a further indication that a non-zero normal net force is determined due to a neglected wall lift force contribution in this analysis.
Overall, the analysis of the fully coupled simulation results shows the contributions of the normal shear-gradient force, the normal drag force and the normal centrifugal force. This is interesting, as the influence of individual force contributions on the particle motion in serpentine microchannel flows was still a topic of research (Gossett and Carlo, 2009; Zhang et al., 2014b).

6.2. One-way coupled simulations of PS-3 particles

For coupled LBM-DEM simulations of even smaller particles, a numerical grid with significantly higher resolution is necessary. As such simulations are computationally costly and corresponding results are currently not available, a simple one-way coupled simulation approach is utilized in the following to numerically determine trajectories of PS-3 particles at bulk Reynolds numbers of $\mathrm{Re_b} = 33$ and $\mathrm{Re_b} = 67$. It may be noted that such a simple approach only allows to gain qualitative statements on the particle force balances and dynamics in close comparison with experiments. Nevertheless, a principal understanding of the behavior of small particles of 3.55 µm as also investigated experimentally is regarded crucial here, as it provides a qualitative understanding of the force balances that are responsible to hold such particles on their individual trajectories.
Results are generated by OpenFOAM v1912. Here, stationary, spatially high resolved liquid flow fields are calculated with the simpleFoam solver. Flow fields are then used as a basis for one-way coupled particle simulations with an in-house extension of the DPMFoam solver. Details on the simulation procedure can be found in section 3.5.2.
The flow field simulations are carefully carried out to obtain low discretization and iteration errors as described in section 3.5.2.2. Exemplary simulated velocity magnitude fields that are taken at $z = 25\,\mu\mathrm{m}$ and at bulk Reynolds numbers of $\mathrm{Re_b} = 33$ and $\mathrm{Re_b} = 67$ are shown in Figures 6.6(a) and (c), respectively. Corresponding flow fields that are extracted from µPIV measurements at the same locations and bulk Reynolds numbers are shown in Figures 6.6(b) and (d). Details on the experimental parameters and the evaluation procedure of these µPIV measurements are provided in section 3.5.4.

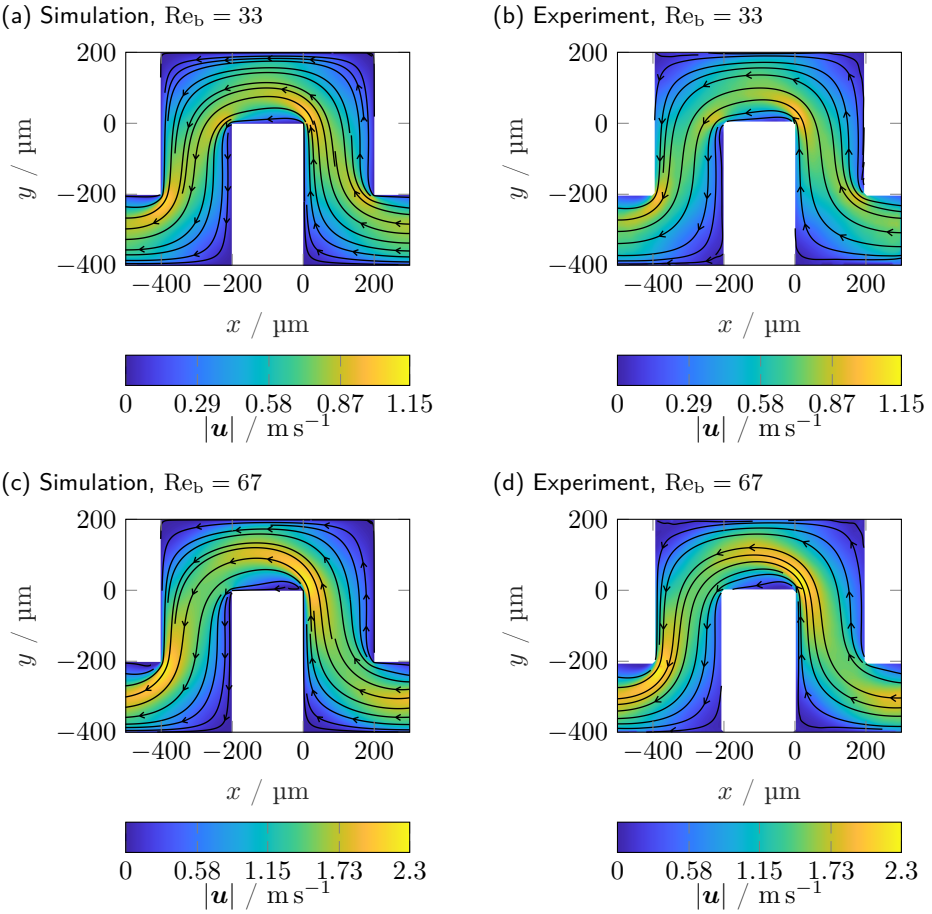

Figure 6.6.: Liquid flow velocity magnitudes and stream slices at $z \approx 25\,\mu\mathrm{m}$ obtained from (a) a simulation at $\mathrm{Re_b} = 33$; (b) a µPIV measurement at $\mathrm{Re_b} = 33$; (c) a simulation at $\mathrm{Re_b} = 67$ and (d) a µPIV measurement at $\mathrm{Re_b} = 67$. The flow direction is from right to left.

Flow fields that are shown in Figures 6.6(a) to (d) demonstrate the principal flow topology inside the serpentine microchannel. The liquid is accelerated inside the 90° turns, such that the respective maximum velocities can be found near the coordinate system origin at $(x, y) = (0\,\mu\mathrm{m}, 0\,\mu\mathrm{m})$. At $\mathrm{Re_b} = 33$, also a second velocity peak occurs near $(x, y) = (-200\,\mu\mathrm{m}, 0\,\mu\mathrm{m})$ in both, numerical and experimental data. At a higher bulk Reynolds number of $\mathrm{Re_b} = 67$, this second velocity peak is not present. Instead, an increase of the region of high

velocities near $(x, y) = (0\,\mu\text{m}, 0\,\mu\text{m})$ occurs in both, numerical and experimental results. Furthermore, the maximum velocity magnitude also increases with increasing bulk Reynolds number. Specifically, the maximum velocity magnitude in the shown planes is $|\boldsymbol{u}_{\max}| \approx 1.04\,\text{m}\,\text{s}^{-1}$ at $\text{Re}_\text{b} = 33$ and increases up to a value of $|\boldsymbol{u}_{\max}| \approx 2.27\,\text{m}\,\text{s}^{-1}$ at $\text{Re}_\text{b} = 67$. As can be expected for laminar flows, a doubled bulk Reynolds number also leads to an approximately doubled maximum liquid flow velocity magnitude.
Overall, the previously shown numerically and experimentally determined liquid flow fields are considered to be in good agreement. Here, numerically and experimentally obtained local maximum velocity magnitudes deviate less than 3% from each other.
Based on previously described flow fields, particle trajectories are simulated. The resulting trajectories of twelve and eleven independent particles are shown in Figures 6.7(a) and (c) for bulk Reynolds numbers of $\text{Re}_\text{b} = 33$ and $\text{Re}_\text{b} = 67$, respectively. It shall be noted that the flow direction is from right to left and, thus, is consistent with the previously shown flow fields. The total simulation time for the particle simulations is set constant to assure a converged state of particle trajectories. Additionally, long-exposure images of PS-3 particles at bulk Reynolds numbers of $\text{Re}_\text{b} = 32$ and $\text{Re}_\text{b} = 69$ are shown in Figures 6.7(b) and (d), respectively. Images of particle trajectories inside the 27th serpentine loop (see also Figure 3.3 for the exact measurement location) are shown.
Both, simulated and measured particle trajectories at the lower bulk Reynolds number (Figures 6.7(a) and (b)) demonstrate that the locations and also the widths of the visible particle streaks are in good agreement. Furthermore, simulated particle streaks develop at two different out-of-plane positions at $z/H \approx 0.27$ and $z/H \approx 0.73$ and, thus, develop a 2×2 configuration.
A 2×2 configuration is also observed for numerically determined particle trajectories at a bulk Reynolds number of $\text{Re}_\text{b} = 67$ (see Figures 6.7(c) and (d)). The numerical results additionally show distinct particle trajectories along the microchannel height at $z/H \approx 0.29$ and $z/H \approx 0.71$. This qualitatively also agrees with the out-of-plane positions of particle trajectories that are determined by APTV measurements (see also Figure 5.2(a)). Interestingly, the height variations between the inner and outer particle trajectory that are observed in APTV measurement results (see Figure 5.1), is also present in the simulation results.
The resulting normal force distributions as a function of the normalized restitution time are shown in Figure 6.8 for an exemplary particle that flows in the serpentine loop at a bulk Reynolds number of $\text{Re}_\text{b} = 33$. The considered particle flows along the lower, inner trajectory of the 2×2 configuration. Normal force contributions that are considered are the centrifugal force $F_{\text{c,n}}$, the drag force $F_{\text{d,n}}$, the shear-gradient force $F_{\text{s,n}}$ and the Saffman force $F_{\text{Saffman,n}}$. Additionally, the sum of the previously described normal force contributions $F_{\text{sum,n}}$ is plotted. It shall be noted that the normal force components are parallel to the x-y-plane and perpendicular to the particle main flow direction, as depicted in Figure 3.11. Furthermore, the

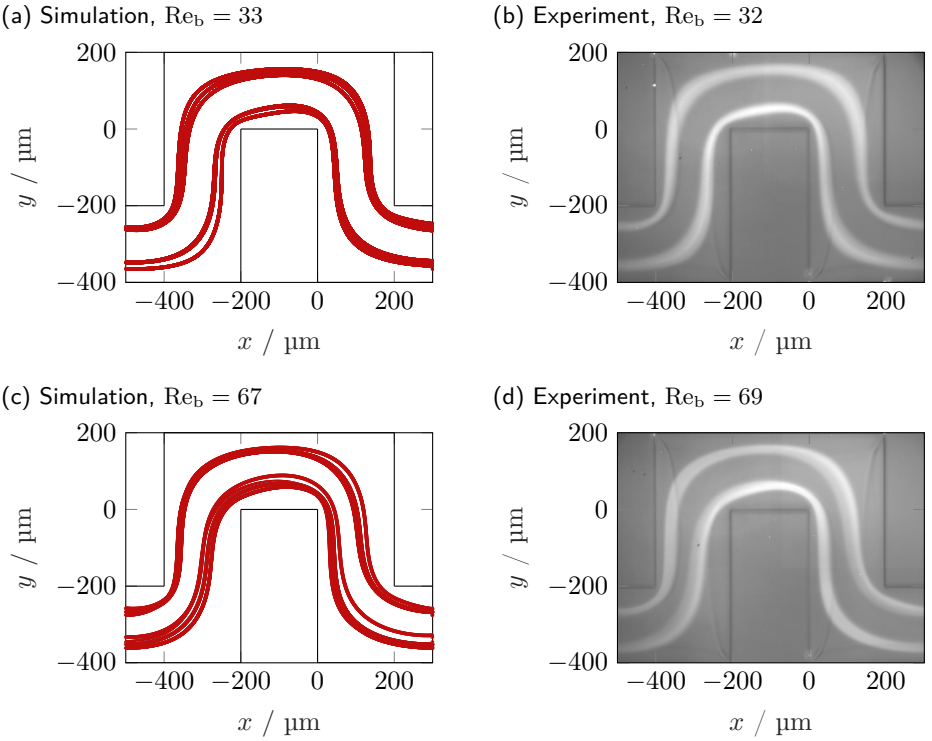

Figure 6.7.: Trajectories of PS-3 particles obtained from (a) a simulation at $\mathrm{Re_b} = 33$; (b) a long-exposure measurement at $\mathrm{Re_b} = 32$; (c) a simulation at $\mathrm{Re_b} = 67$ and (d) a long-exposure measurement at $\mathrm{Re_b} = 69$. Flow direction is from right to left.

normalized restitution time is scaled such that it is $t/t_{\mathrm{ref}} = 0$ when the particle is located at the inlet and $t/t_{\mathrm{ref}} = 1$ when the particle is located at the outlet of the flow domain. Additionally, gray vertical dashed lines indicate the moment at which the particle passes the corresponding cross-sectional evaluation plane, as defined in Figure 6.9. There, the corresponding particle trajectory is plotted, as well.
Similar as for PS-10 particles at the same bulk Reynolds number, the normal centrifugal force and the normal shear-gradient force develop distinct peaks inside the 90° turns, i.e. near planes 6 and 10. This is expected as the considered PS-3 particle follows a similar trajectory as the considered PS-10 particle at this bulk Reynolds number (see section 6.1). Thus, it follows a trajectory with a small orbit at planes 6 and 10 that is close to the regions where the maximum liquid flow velocities can be found (see also Figure 6.6). This leads to the previously described peaks in these force distributions.

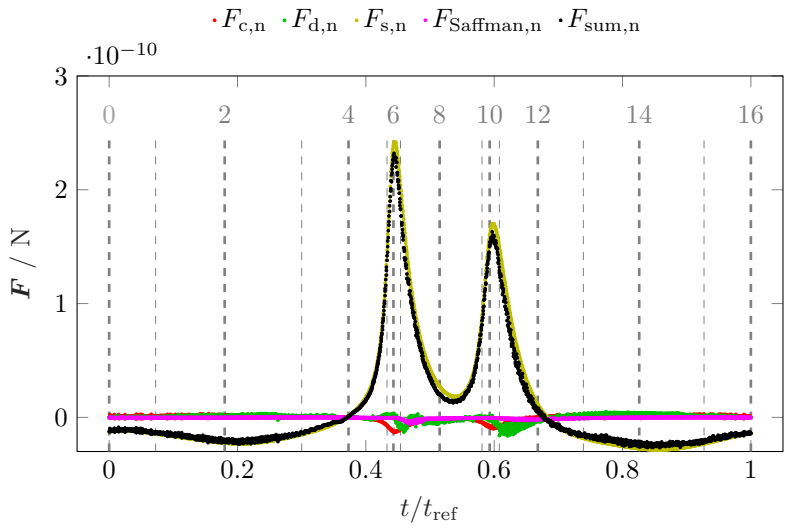

Figure 6.8.: Normal force distributions as a function of the normalized restitution time of a PS-3 particle that flows along the lower, inner trajectory through one serpentine loop at a bulk Reynolds number of $\mathrm{Re_b} = 33$. Numbers above the vertical dashed lines indicate the position of the cross-sectional planes that are shown in Figure 6.9.

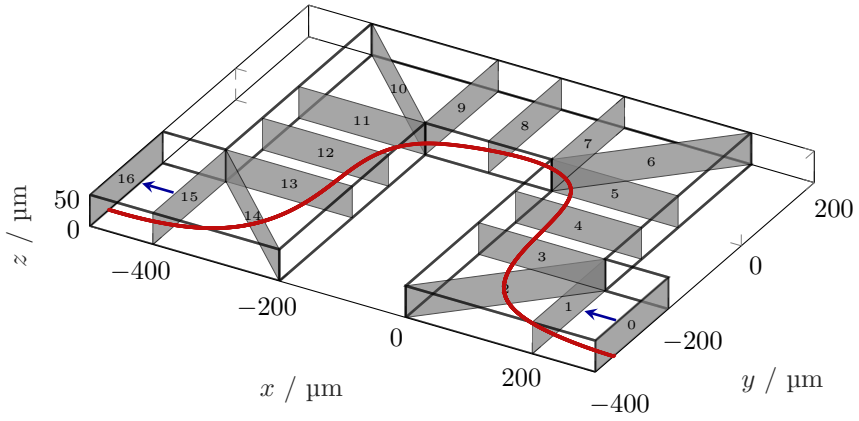

Figure 6.9.: Locations of evaluation planes inside one serpentine loop and trajectory of the considered PS-3 particle at $\mathrm{Re_b} = 33$.

Furthermore, force distributions plotted in Figure 6.8 demonstrate that the normal centrifugal force and the normal Saffman force are one to two orders of magnitude

smaller than the normal shear-gradient force.
In contrast to the investigations of the forces that act on PS-10 particles, the normal drag force is one to two orders of magnitude smaller than the normal shear-gradient force, as well. This is not surprising, as the drag force generally scales with the particle diameter (see also (2.5)).
For the normal centrifugal force and the normal shear-gradient force, the three characteristic regions that are already observed in section 6.1 for PS-10 particles are present. A qualitative similar distribution of the normal centrifugal force and the normal shear-gradient force is expected as the bulk Reynolds number and, thus, the characteristics of the liquid flow field, are similar. However, the force magnitudes that are determined for PS-3 particles are about one order of magnitude smaller than for PS-10 particles.
The sum of normal forces is dominated by the normal shear-gradient force. The integrated sum of normal forces is positive and two orders of magnitude smaller than the maximum values of the sum of normal forces. As discussed in section 6.1, it is assumed that neglecting the wall lift force is responsible for this non-zero normal net force. However, unlike as for fully coupled simulations, the simulated particle dynamics of one-way coupled simulations do not consider any wall lift force contribution, as particle induced disturbances of the flow field are not considered.
Figure 6.10 shows how the force contributions evolve when the same type of particle moves through the channel at an increased bulk Reynolds number of $\mathrm{Re_b} = 67$. The corresponding particle trajectory and the locations of the evaluation planes are plotted in Figure 6.11.
The individual normal force distributions and, consequently, also the sum of considered normal forces show a similar qualitative behavior for $\mathrm{Re_b} = 67$ as for $\mathrm{Re_b} = 33$. Consequently, the three previously described characteristic regions are also observable for the normal shear-gradient force and the normal centrifugal force at this increased bulk Reynolds number. In contrast to the previously discussed normal force distributions, the normal drag force increases relative to the normal centrifugal force and the normal shear-gradient force. This indicates that the normal relative velocity between particle and liquid increases at increased bulk Reynolds numbers. This may be caused due to the larger ratio between the normal shear-gradient force and the normal centrifugal force, which develops a peak that is up to three times larger compared to the $\mathrm{Re_b} = 33$ case. The normal Saffman force is obviously of minor importance for the motion of the considered particle at this bulk Reynolds number.
The integrated sum of normal forces is positive and two orders of magnitude smaller than the absolute maximum values of the sum of normal forces at a bulk Reynolds number of $\mathrm{Re_b} = 67$.
Overall, it is shown that the trajectories of PS-3 particles agree well with experimental results in the considered bulk Reynolds number regime. An essential result is here that also for smaller particles the normal shear-gradient force dominates, if particles follow a 2×2 trajectory configuration. While 2×2 particle configurations

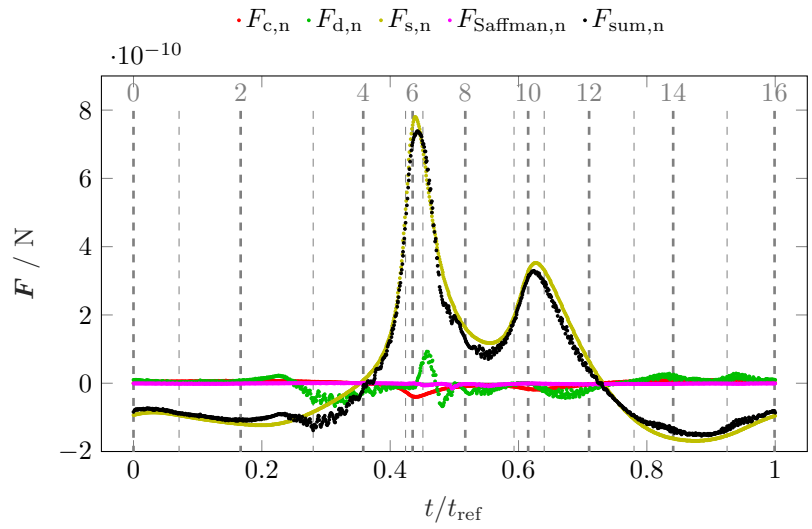

Figure 6.10.: Normal force distributions as a function of the normalized restitution time of a PS-3 particle that flows along the lower, inner trajectory through one serpentine loop at a bulk Reynolds number of $\mathrm{Re_b} = 67$. Numbers above the vertical dashed lines indicate the position of the cross-sectional planes that are shown in Figure 6.11.

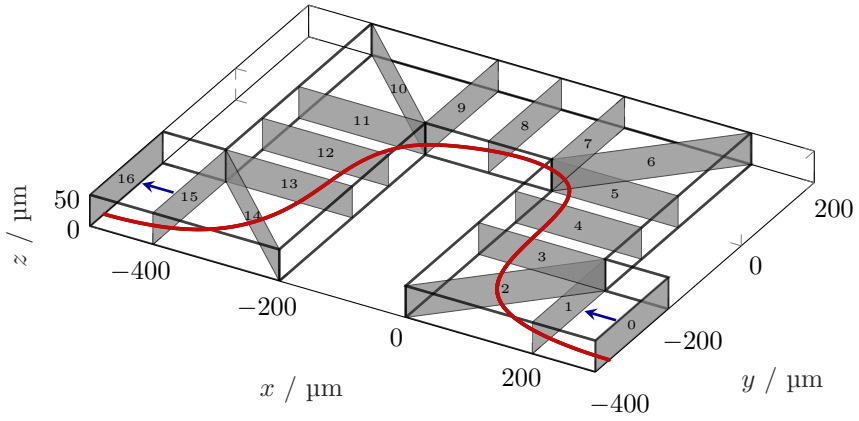

Figure 6.11.: Locations of evaluation planes inside one serpentine loop and trajectory of the considered PS-3 particle at $\mathrm{Re_b} = 67$.

as observed in the experiments could be well recovered by a simple one-way coupling approach, it was not possible to recover the merging of existing particle trajectories

towards a 1×2 configuration. It is assumed that this dynamics is strongly influenced by the interaction between fluid and particles, which is also indicated by a non-zero normal net force.

6.3. Conclusion

In this chapter, the force contributions that are responsible to hold particles on distinct trajectories are investigated. For this, a fully coupled LBM-DEM approach is utilized to simulate the trajectories of PS-10 particles at bulk Reynolds numbers of $\mathrm{Re_b} = 33$ and $\mathrm{Re_b} = 100$. Additionally, a simpler one-way coupled approach is utilized to gain a qualitative insight into the force balances acting on smaller PS-3 particles at bulk Reynolds numbers of $\mathrm{Re_b} = 33$ and $\mathrm{Re_b} = 67$.
The simulated particle trajectories for the previously described parameters agree well with experimental observations. The analysis of normal force contributions that act on PS-10 particles reveal that the drag and shear-gradient forces are dominant for the particle motion in a 2×2 trajectory configuration. The same is true at a bulk Reynolds number of $\mathrm{Re_b} = 100$, at which particles develop a 1×2 trajectory configuration. Here, the influence of the normal drag force increases relative to the normal shear-gradient force compared to $\mathrm{Re_b} = 33$. The qualitative characteristics of the normal centrifugal force and the normal shear-gradient force are similar for both, PS-10 and smaller PS-3 particles that flow in a 2×2 configuration through a serpentine loop.

7. On the accuracy and reliability of micro-PIV measurements utilizing ring-shaped particle images[1]

To assess the suitability of cross-correlation based measurement techniques like micro Particle Image Velocimetry for measurements in dense suspensions, the displacement estimation error and the detectability of zero-displaced Gaussian, ring- and plateau-shaped particle images of different particle image diameters is evaluated. For this purpose Monte Carlo simulations are conducted that are based on synthetically generated particle images (section 7.1). These show that the accuracy and reliability of particles with large image diameter strongly depends on the particle image shape.
To understand the dynamics of suspended particles, the relative motion between particles and surrounding fluid is evaluated. Relative motion may, e.g., occur when the particle diameter is in the order of magnitude of the characteristic channel dimensions and, therefore, is much larger than the diameter of tracer particles commonly used in PIV measurements. To demonstrate the suitability of the utilized ring-shaped particle images to measure such suspension dynamics, micro Particle Image Velocimetry (µPIV) measurements are performed (section 7.2). As, additionally, small tracer particles are suspended to the flow, a simultaneous evaluation of the velocity profiles of both, the continuous and the particulate phase is possible.

7.1. Results based on synthetically generated images

To evaluate the influence of the particle image diameter and shape on the displacement estimation error and the detectability, Monte Carlo simulations based on ensembles of 500 double-frame images are performed (section 7.1.1 and section 7.1.2).
For small particle images, an in-plane loss-of-pairs refers to particles that are located only in one interrogation window of the first or second frame (Keane and Adrian, 1992). However, when considering large particle image sizes, the contribution of

[1] Parts of this chapter are published in Blahout et al. (2021), used under CC BY 4.0. The original contents have been edited and/or extended for this work.

intersected particle images may become relevant, too. This effect is investigated for Gaussian, ring- and plateau-shaped particle images in section 7.1.3.
In real measurement situations, particle images are displaced between two consecutive frames. The influence of non-zero particle image displacements on the estimation error, the detectability and the deviation of the resulting displacement vector is investigated based on Monte Carlo simulations in section 7.1.4.
For the cross-correlation of synthetically generated data (see section 3.6.1), a commercial PIV evaluation software (DaVis 8.4, LaVision GmbH, Germany) is used.

7.1.1. Influence of the particle image shape and diameter on the estimation error

In this section, the influence of the particle image shape and diameter on the displacement estimation error is described. Excluded are the effects of particle images that are intersected at interrogation window borders and a non-zero particle image displacement between corresponding frames. These are discussed in sections 7.1.3 and 7.1.4, respectively.
Figures 7.1(a)-(f) show single cross-correlation results for two particle image sizes of synthetic image data with Gaussian, ring- and plateau-shaped particle images. Cross-correlation results for particle image diameters of $d_{\mathrm{p,I}} = 5\,\mathrm{px}$ (Figure 7.1(a), (c) and (e)), as well as $d_{\mathrm{p,I}} = 60\,\mathrm{px}$ (Figure 7.1(b), (d) and (f)) and zero displacement are shown on the left and right hand side, respectively. It is evident that the correlation peak width increases with the particle image diameter for all three types of particle image shapes. Furthermore, a comparison of displacement correlation peaks close to their maximum values reveals that correlation peaks resulting from ring-shaped particle images are most narrow compared to those of Gaussian and plateau-shaped particle images (see Figures 7.2(a) to (c)).
The scaling behavior between the particle image shape and the displacement estimation error is evident in the correlation peak width (see (2.21)). Here, the first term $\tilde{\epsilon}_{\mathrm{D},1}$ grows with an increasing displacement correlation peak width, while the second term $\tilde{\epsilon}_{\mathrm{D},2}$ of the displacement estimation error denotes random errors. Thus, in comparison to Gaussian particle images a reduced estimation error is expected for ring-shaped particle images while a slightly increased estimation error is expected for plateau-shaped particle images. Figure 7.3(a) shows the displacement estimation error without considered image noise in a semi-logarithmic scale as a function of the particle image diameter derived from a Monte Carlo simulation for Gaussian, ring- and plateau-shaped particle images.
Every data point results from 500 cross-correlated double-frames, each containing five particle images and zero displacement between corresponding frames. All graphs resemble a non-monotonic relationship with a minimum estimation error at $d_{\mathrm{p,I}} \approx 2 - 3\,\mathrm{px}$ as it is also shown for Gaussian particle images by Westerweel (1997). Obviously, this minimum value corresponds to the optimum particle image

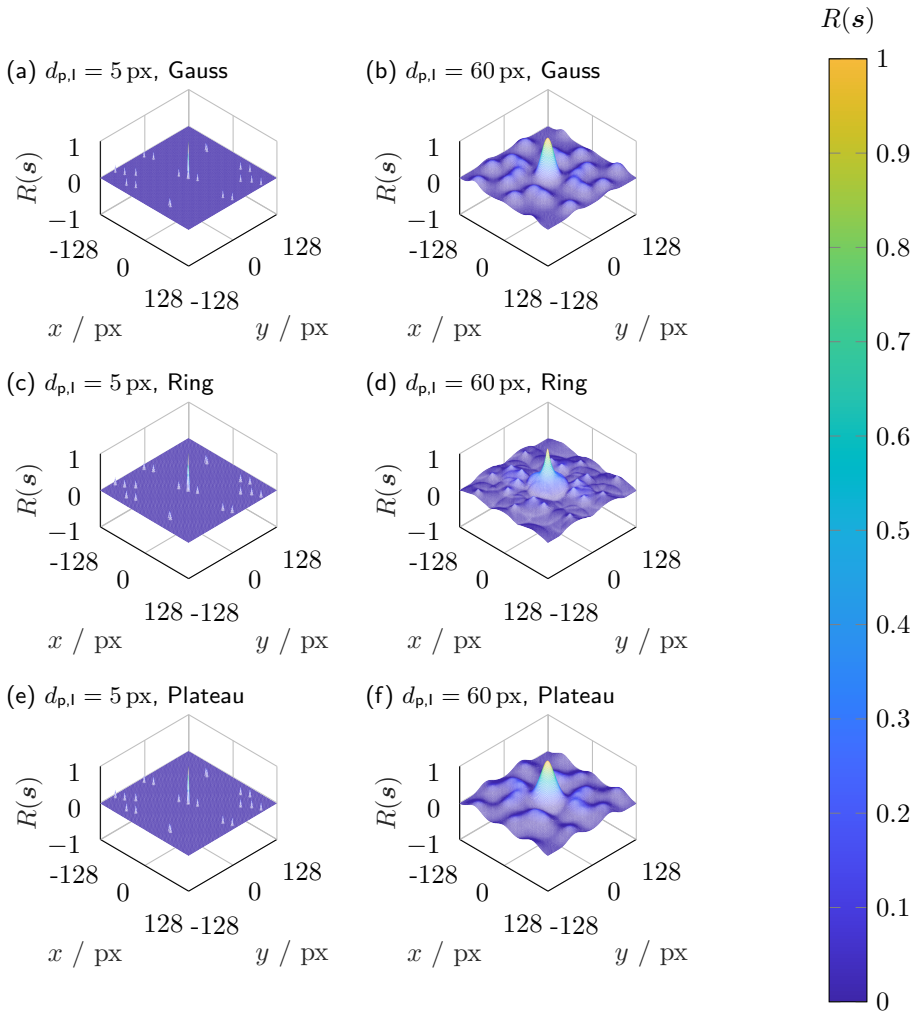

Figure 7.1.: Correlation maps resulting from the cross-correlation for a zero displacement of synthetically generated images with five (a) $5\,\mathrm{px}$ Gaussian, (b) $60\,\mathrm{px}$ Gaussian, (c) $5\,\mathrm{px}$ ring-shaped, (d) $60\,\mathrm{px}$ ring-shaped, (e) $5\,\mathrm{px}$ plateau-shaped and (f) $60\,\mathrm{px}$ plateau-shaped particle images.

diameter for PIV measurements as also given in the common literature (Raffel et al., 2007; Adrian and Westerweel, 2011). For smaller particle image diameters peak locking effects occur, which result in an increased estimation error. For larger particle image diameters random errors lead to an increased estimation

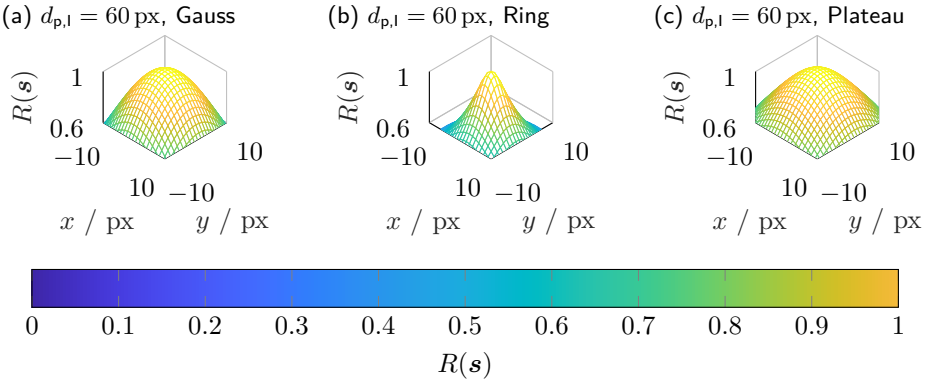

Figure 7.2.: Zoomed in view of displacement correlation peak tops resulting from the cross-correlation of double-frame images, each containing five particle images with zero displacement between corresponding frames, using (a) Gaussian, (b) ring-shaped and (c) plateau-shaped particle images of $d_{\mathrm{p,I}} = 60\,\mathrm{px}$.

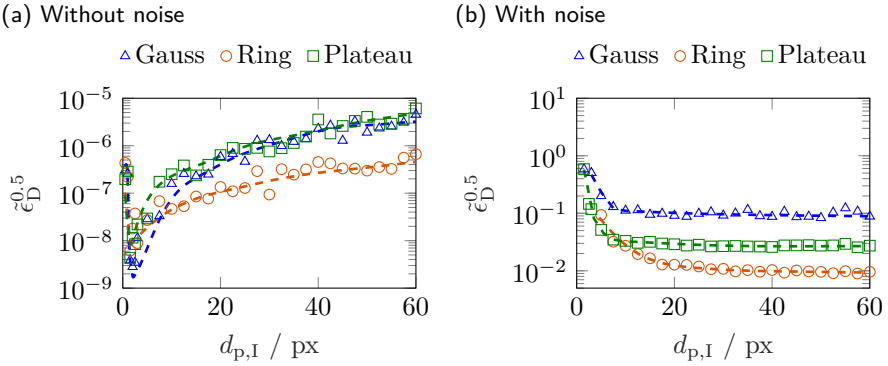

Figure 7.3.: Estimation error as a function of the particle image diameter (a) without and (b) with 8.5% image noise. Results are based on 500 samples per particle image diameter. Dashed lines denote fits to the respective data.

error (Westerweel, 1997). While the estimation error appears to stay in the same order of magnitude for Gaussian and plateau-shaped particle images with growing image diameter, a clear distinction has to be made for ring-shaped particle images for $d_{\mathrm{p,I}} \gtrsim 10\,\mathrm{px}$. Figure 7.3(a) shows a reduction of the displacement estimation error of up to one order of magnitude for ring-shaped particle images compared to Gaussian or plateau-shaped particle images (for $d_{\mathrm{p,I}} \gtrsim 10\,\mathrm{px}$). This can be

understood from the fact that, for a constant particle image diameter, ring-shaped particle images decorrelate faster than Gaussian or plateau-shaped particle images, due to their large intensity gradient at the particle image border and a nearly transparent center region. Thus, the correlation peak width decreases (see also Figure 7.1(d)), resulting in an improved displacement estimation error.
Figure 7.3(a) displays results for noise-free data only, a situation that is hardly found in experiments. To validate cross-correlation results of images that are closer to pre-processed experimental measurement data, image noise of 8.5% is added (for details of the synthetic image generation see section 3.6.1) and the data set is analyzed as well. The resulting estimation errors are shown in Figure 7.3(b).
A clear difference in displacement estimation error for all three particle image shapes is evident in Figure 7.3(b). However, image noise leads to a strong increase in random errors in the correlation plane (Meinhart et al., 2000). Thus, in comparison to the noise free data that are shown in Figure 7.3(a), the overall level of displacement estimation error is now increased by approximately four orders of magnitude. This is due to an increase in the correlation peak asymmetry, represented by $\tilde{\epsilon}_{\mathrm{D},2}$ in (2.21), i.e. random errors in the correlation plane.
Furthermore, it is remarkable to see that noisy Gaussian particle images have a significantly higher estimation error compared to noisy plateau-shaped particle images while the corresponding noise free particle images lead to very similar displacement estimation errors (see Figure 7.3(a)). Figure 7.4 shows both $\tilde{\epsilon}_{\mathrm{D},1}$ and $\tilde{\epsilon}_{\mathrm{D},2}$ as a function of the particle image diameter $d_{\mathrm{p,I}}$ for noise-free and noisy image data. It should be noted that results of $\tilde{\epsilon}_{\mathrm{D},1}$ for images with and without noise coincide. Therefore, results of noisy image data are left out in Figure 7.4 for a clearer presentation.
As shown in Figure 7.4, the increased estimation error of Gaussian particle images results from an increased amount of random errors in the correlation plane. This is obvious, since the values of $\tilde{\epsilon}_{\mathrm{D},1}$ are similar for Gaussian and plateau-shaped particle images with and without noise, but values of $\tilde{\epsilon}_{\mathrm{D},2}$ differ significantly.
For particle image diameters of $d_{\mathrm{p,I}} < 3\,\mathrm{px}$ the particle image diameter is of the same length scale as the image noise, leading to an increased asymmetry of individual particle image peaks. This induces an increase in random errors represented by $\tilde{\epsilon}_{\mathrm{D},2}$, as shown in Figure 7.4. Here, $\tilde{\epsilon}_{\mathrm{D},2}$ for images with noise shows increased values for all three particle image shapes, compared to the values of $\tilde{\epsilon}_{\mathrm{D},2}$ without noise. For larger particle images the random error decreases as the particle image diameter becomes significantly larger than the length scale of the image noise.

7.1.2. Influence of the particle image size and shape on the detectability

Figures 7.5(a) and (b) show the detectability D as a function of the particle image diameter for Gaussian, ring- and plateau-shaped particle images without and with image noise of 8.5%.

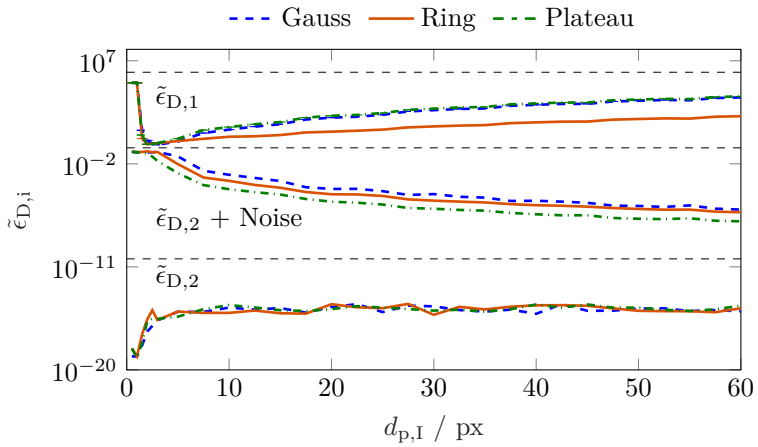

Figure 7.4.: Factors $\tilde{\epsilon}_{\mathrm{D},1}$ and $\tilde{\epsilon}_{\mathrm{D},2}$ of (2.21) for Gaussian, ring- and plateau-shaped particle images with and without noise. For a clearer presentation, results of $\tilde{\epsilon}_{\mathrm{D},1}$ for images with noise are not plotted, as they coincide with corresponding results without image noise.

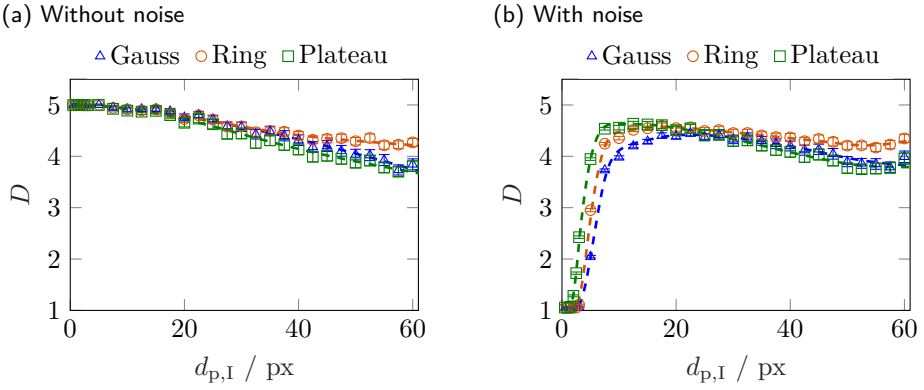

Figure 7.5.: Detectability with 95% confidence intervals as a function of the particle image diameter averaged over 500 samples per particle image diameter (a) without and (b) with 8.5% image noise. Dashed lines denote fits to the respective data.

A general decrease of the detectability with increasing particle image diameter can be associated with a significant increase of the particle image density N_{ppp}, i.e., the portion of pixels that is occupied by particle images relative to the total

amount of pixels within an interrogation window increases. While the effective number of particle images is constant ($N_{\mathrm{p,I}} = 5$ for all images), the particle image density increases from $N_{\mathrm{ppp}} \approx 0.00006$ for $d_{\mathrm{p,I}} = 1\,\mathrm{px}$ to $N_{\mathrm{ppp}} \approx 0.22$ for $d_{\mathrm{p,I}} = 60\,\mathrm{px}$. Since the particle image density N_{ppp} mainly influences the height of the secondary correlation peak (Scharnowski et al., 2018), an increase in particle image diameter and N_{ppp}, respectively, reduces the detectability for a constant $N_{\mathrm{p,I}}$. Furthermore, Figures 7.5(a) and (b) show that the detectability decreases slower for growing ring-shaped particle images compared to those with Gaussian or plateau shape. It is assumed, that this is due to the characteristics of ring-shaped particle images, as slightly shifted ring-shaped particle image groups decorrelate faster than corresponding Gaussian or plateau-shaped particle image groups.
Figure 7.5(b) shows the detectability as a function of the particle image diameter for images with noise (as described in section 3.6.1). Obviously, image noise affects especially the detectability for small particle image diameters ($d_{\mathrm{p,I}} < 10\,\mathrm{px}$). This is to be expected, as for small particle images the signal to noise ratio is decreased, leading to a lower detectability and thus to an increased probability of erroneous cross-correlations. A reduced signal to noise ratio originates from particle image discretization where very narrow particle image intensity peaks are averaged over a full pixel, thereby being reduced in their maximum intensity value (see also Figure 3.14). This effect is well-known from classical PIV experiments where one strives for particle image diameters of two to three pixels.

7.1.3. Influence of intersected particle images on the cross-correlation result

To study the influence of intersected particle images on the cross-correlation result, three cases are considered for one, three and five out of five particle images located with their center points on the interrogation window border. These cases with particle images located only to 50% inside the interrogation window are denoted with $K_5 = 1$, 3 and 5, respectively, where the index of K denotes the total amount of particle images inside the corresponding interrogation window. An intersection ratio of 50% is chosen, because the amount of pixels at which an intensity gradient jump occurs is largest for this situation. Thus, the influence of intersected particle images on the displacement estimation error and the detectability is assumed to be most significant.
Figures 7.6(a) to (c) show the displacement estimation error as a function of the particle image diameter for $K_5 = 1$, 3 and 5 for Gaussian and ring-shaped particle images. Since the results of plateau-shaped particle images strongly coincide with that of Gaussian particle images, results of plateau-shaped particle images are omitted here. It is obvious, that the amount of intersected particle images has a stronger influence on the displacement estimation error for Gaussian particle images compared to ring-shaped particle images.

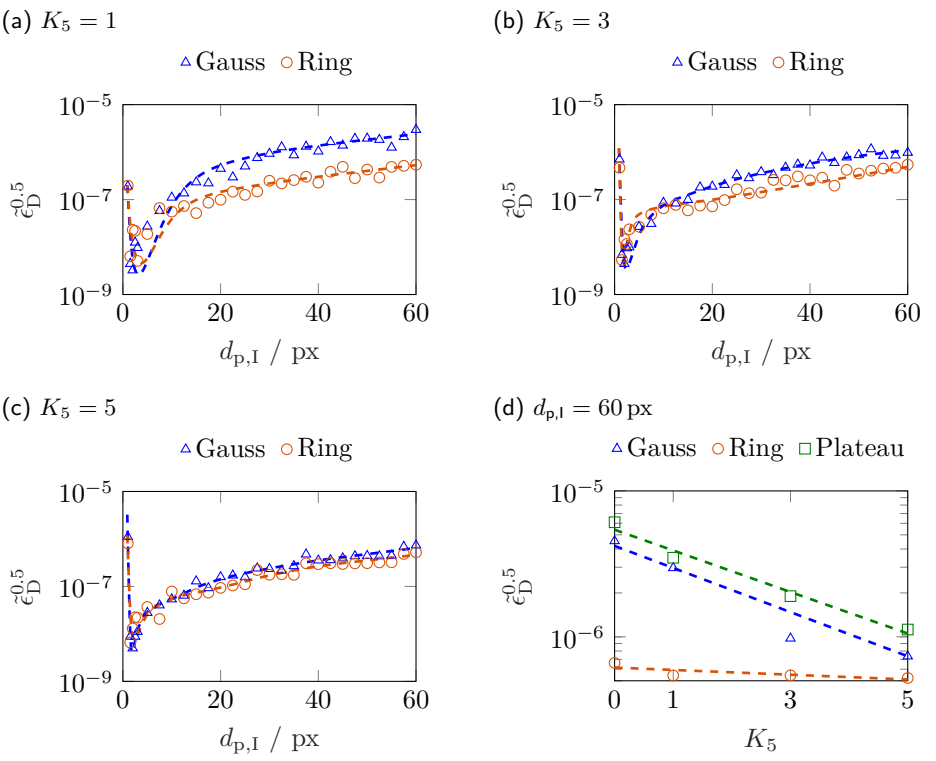

Figure 7.6.: Estimation error as a function of the particle image diameter for (a) $K_5 = 1$, (b) $K_5 = 3$ and (c) $K_5 = 5$. (d) Estimation error as a function of the amount of intersected particle images of $d_{p,I} = 60\,\mathrm{px}$. Dashed lines denote fits to the respective data.

Figure 7.6(d) displays the displacement estimation error as a function of K_5 for Gaussian, ring- and plateau-shaped particle images of $d_{p,I} = 60\,\mathrm{px}$. The displacement estimation error reduces for intersected Gaussian and plateau-shaped particle images for increasing K_5-values. This is because intersected particle images deliver a sharp intensity jump at the interrogation window border. Such a sharp intensity jump leads to a reduction in the correlation peak width and hence an improved displacement estimation error. As more particles are intersected, their contribution to the cross-correlation result enhances the aforementioned effect. As already shown in section 7.1.1, ring-shaped particle images decorrelate faster for slight image shifts due to the relatively small ring width and the transparent inner region. This is also the reason why the effect of intersected particle images on the estimation error is strongly reduced compared to Gaussian and plateau-shaped

particle images. Nevertheless, it should be noted that the development of the displacement estimation error may change significantly if particle images within an interrogation window are displaced by values other than zero. Especially if the particle image displacement is smaller than the portion of particle images that is located inside the interrogation window, cross-correlation based evaluations may lead to systematic errors. To overcome this, apodization window functions as they are described by A. C. Eckstein et al. (2008) and A. Eckstein and Vlachos (2009) may be used. Nevertheless, such apodization window functions have not been applied in the present study.

The influence of intersected particle images at the interrogation window border on the detectability D is illustrated in Figures 7.7(a) to (d). Figures 7.7(a) to 7.7(c) show how D alters as a function of the particle image diameter $d_{\mathrm{p,I}}$ for Gaussian and ring-shaped particle images with $K_5 = 1$, 3 and 5. For a better conciseness, curves for plateau-shaped particle images are omitted as they show no significant differences to those of Gaussian particle images.

Comparing different values of K_5, a qualitative change in the detectability evolution can be recognised. While a monotonous decrease in the detectability can be observed for $K_5 = 1$ (Figure 7.7(a)) with growing particle image size, it appears to be non-monotonous for $K_5 = 3$ (Figure 7.7(b)) and $K_5 = 5$ (Figure 7.7(c)). This qualitative behavior is found for all particle image shapes and indicates that different competing effects come into play here. Firstly, a decrease in detectability with increasing particle image size is also observed when no particle images intersect the interrogation window border (see Figure 7.5(a)). It originates from the relative increase in secondary correlation peak values that are a result of an increase of the particle image density N_{ppp} for a constant effective number of particle images $N_{\mathrm{p,I}}$. A growing number of intersected particle images is in our case associated with a decreasing number of particle images located inside the interrogation window (as the total number of particle images is chosen to be constant here). Thus, an increasing number of intersected particle images leads to a decreased particle image density N_{ppp}, which in turn results in an improved detectability due to a decrease in secondary correlation peak values. However, the overall detectability seems to be lowest for $K_5 = 3$ while it is clearly enhanced for smaller or larger K_5 values. Therefore, this effect alone does not explain the overall behavior. It is assumed, that the detectability is decreased as the probability of erroneous correlations resulting from particle images inside the interrogation window correlating with intersected particle images is largest for $K_5 \approx 1/2 \cdot N_{\mathrm{p,I}}$. This is due to a similar number of particle images inside the interrogation window and on the interrogation window border, respectively. Furthermore, the location of particle images at the interrogation window border is strongly restricted. This obviously leads to a relative increase in secondary correlation peak values and hence a reduced detectability. It should be noted that, to overcome a decrease in detectability due to a certain amount of intersected particle images, apodization window functions may be applied.

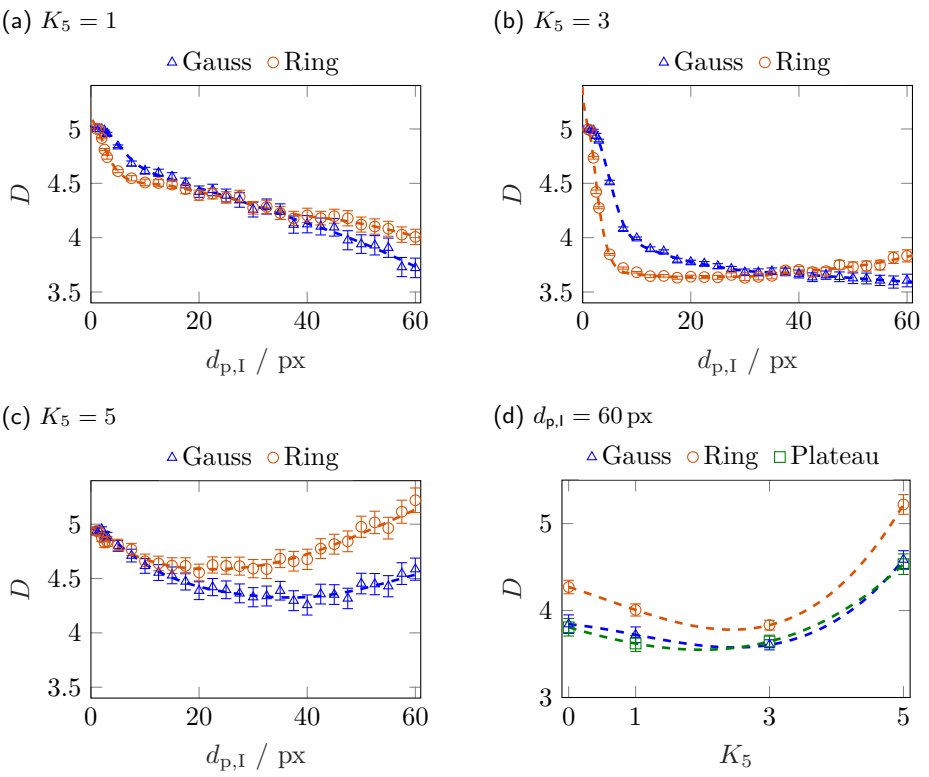

Figure 7.7.: Detectability with 95% confidence intervals for Gaussian and ring-shaped particle images as a function of the particle image diameter for (a) $K_5 = 1$, (b) $K_5 = 3$ and (c) $K_5 = 5$. (d) Detectability with 95% confidence intervals as a function of the amount of intersected particle images of $d_{p,I} = 60\,px$. Dashed lines denote fits to the respective data.

Figure 7.7(d) shows detectability values of Gaussian, ring- and plateau-shaped particle images of $d_{p,I} = 60\,px$ diameter as a function of K_5. The detectability shows a non-monotonic behavior for growing K_5 values. Furthermore, the detectability of Gaussian and plateau-shaped particle images has similar values (see also Figure 7.5(a)), while it is slightly increased for ring-shaped particle images. It may be noted here that values of $K_5 = 5$ are a hypothetical case. However, for high-resolution studies on dense particle systems such as suspension micro flows, large values of K can be expected as K scales with the particle image diameter or, respectively, decreasing interrogation window size.
Figure 7.8 illustrates the evolution of the ratio of K to the total amount of particle images per interrogation window as a function of the ratio between interrogation

window edge length l_{IW} to particle image diameter $d_{\mathrm{p,I}}$, for in-plane particle images with simple cubic packing (see inset of Figure 7.8).

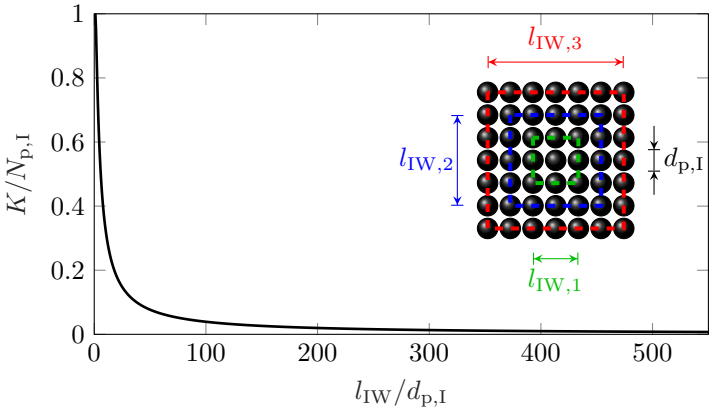

Figure 7.8.: Development of the ratio of the amount of intersected particle images and the total amount of particle images per interrogation window $K/N_{\mathrm{p,I}}$ as a function of the ratio of the corresponding interrogation window length and the particle image diameter $l_{\mathrm{IW}}/d_{\mathrm{p,I}}$.

As can be seen, values in the order of one can be expected for a ratio of interrogation window size and particle image diameter of $l_{\mathrm{IW}}/d_{\mathrm{p,I}} < 5$ - a situation easily encountered in suspension flow studies.
Similar qualitative results in terms of estimation error and detectability as shown in Figure 7.6(d) and Figure 7.7(d) are also obtained from experiments. Both, the estimation error and the detectability are determined for experimental images containing ring- or plateau-shaped particles of $d_{\mathrm{p}} = 60\,\mu\mathrm{m}$, respectively. Images are auto-correlated in the commercial software DaVis 8.4 (LaVision GmbH, Germany) utilizing decreasing interrogation window sizes. The latter results in interrogation window length to particle image diameter ratios of $l_{\mathrm{IW}}/d_{\mathrm{p,I}} = 5.3$, 2.6, 1.3, 0.7 and 0.3. Similar to the results obtained from synthetically generated images, also for experimental images the dominant term of the displacement estimation error $\tilde{\epsilon}_{\mathrm{D,1}}$ is one to two orders of magnitude smaller for ring-shaped particle images than for plateau-shaped particle images (see also Figure 7.4 and Figure 7.6(d)). This holds true for all considered values of $l_{\mathrm{IW}}/d_{\mathrm{p,I}}$.
The detectability of experimental ring-shaped particle images is slightly larger than for experimental plateau-shaped particle images for $l_{\mathrm{IW}}/d_{\mathrm{p,I}} = 5.3$. Qualitatively, this is in accordance to the detectability results obtained from synthetic data for $l_{\mathrm{IW}}/d_{\mathrm{p,I}} = 4.3$ (see also Figure 7.7(d)). For smaller values of $l_{\mathrm{IW}}/d_{\mathrm{p,I}}$, the variation of the detectability of experimental ring-shaped particle images increases, such that similar detectabilities are obtained for both particle image shapes.

7.1.4. Influence of non-zero particle image displacements on the cross-correlation result

In the preceding sections, the influence of the particle image size and shape on the cross-correlation result has been investigated only for zero-displaced particle images. The influence of non-zero particle image displacements on the cross-correlation result is discussed in the following.
As a basis, 500 synthetic double-frame images, each consisting of five Gaussian, ring- or plateau-shaped particle images, are generated without image noise (see also section 3.6.1). Particle images have a constant diameter of $d_{\mathrm{p,I}} = 60\,\mathrm{px}$. Between both frames, particle images are displaced uniformly by several non-fractional values that range from $\delta\boldsymbol{X}_{\mathrm{p,I}} = 1\,\mathrm{px}$ to $\delta\boldsymbol{X}_{\mathrm{p,I}} = 60\,\mathrm{px} = d_{\mathrm{p,I}} \approx 0.25 \cdot l$ in horizontal direction. The cross-correlation evaluation is performed in the commercial software DaVis 8.4 (LaVision GmbH, Germany) and is analysed with regard to the displacement estimation error, the detectability and the deviation between the calculated and the specified particle image displacement.
Figure 7.9 shows the displacement estimation error as a function of the magnitude of the displacement vector $|\delta\boldsymbol{X}_{\mathrm{p,I}}|$, i.e. the horizontal displacement, for Gaussian, ring- and plateau-shaped particle images.

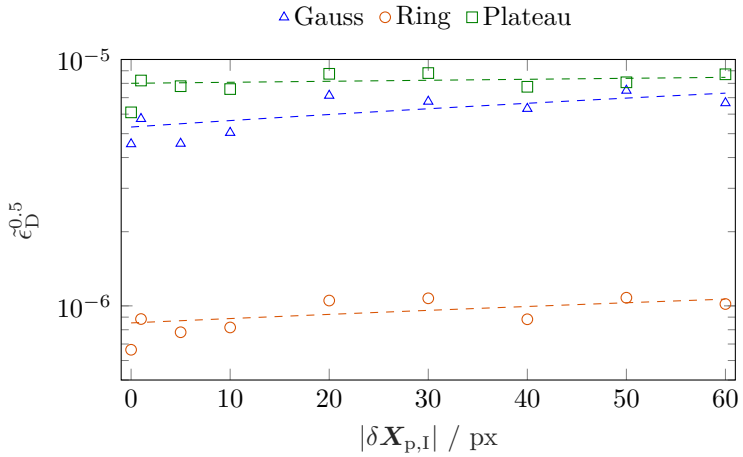

Figure 7.9.: Estimation error as a function of the particle image displacement for Gaussian, ring- and plateau-shaped particle images of $d_{\mathrm{p,I}} = 60\,\mathrm{px}$. Dashed lines denote fits to the respective data.

Compared to zero-displaced particle images (see also Figure 7.3 in section 7.1.1), the displacement estimation error slightly increases for particle image displacements of $\delta\boldsymbol{X}_{\mathrm{p,I}} \geq 1\,\mathrm{px}$ for all considered particle image shapes. Figure 7.9 also shows that the displacement estimation error slightly increases with increasing particle image

displacement for Gaussian and ring-shaped particle images. Qualitatively, this is in agreement with the development of the estimation error for Gaussian particle images of $d_{\mathrm{p,I}} = 2\,\mathrm{px}$ (Westerweel, 1997). This increase can be associated with an increase of the second term of the displacement estimation error $\tilde{\epsilon}_{\mathrm{D},2}$ (see also (2.21)), as shown in Figures 7.10(a) and (b). Here, the deviations of the individual error contributions for non-zero displacements relative to the corresponding error contributions of zero displacements, i.e. $\tilde{\epsilon}_{\mathrm{D,i,rel}} = |[\tilde{\epsilon}_{\mathrm{D,i}}(|\delta\boldsymbol{X}_{\mathrm{p,I}}|) - \tilde{\epsilon}_{\mathrm{D,i}}(|\delta\boldsymbol{X}_{\mathrm{p,I}}| = 0)]\,/\tilde{\epsilon}_{\mathrm{D,i}}(|\delta\boldsymbol{X}_{\mathrm{p,I}}| = 0)|$, are plotted as a function of the magnitude of the particle image displacement.

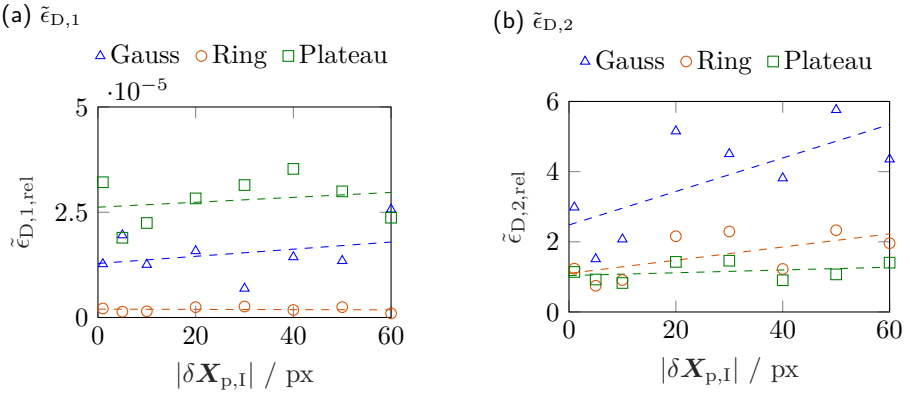

Figure 7.10.: Relative deviations of the estimation error components (a) $\tilde{\epsilon}_{\mathrm{D,1,rel}}$ and (b) $\tilde{\epsilon}_{\mathrm{D},2}$ as a function of the particle image displacement for Gaussian, ring- and plateau-shaped particle images of $d_{\mathrm{p,I}} = 60\,\mathrm{px}$. Dashed lines denote fits to the respective data.

Figure 7.10(a) shows that the first estimation error term $\tilde{\epsilon}_{\mathrm{D},1}$ is rather insensitive to a non-zero displacement for all particle image shapes considered. In contrast to this, the second term $\tilde{\epsilon}_{\mathrm{D},2}$ increases with increasing particle image displacement for Gaussian and ring-shaped particle images, as shown in Figure 7.10(b). For plateau-shaped particle images the second term $\tilde{\epsilon}_{\mathrm{D},2}$ is generally larger for non-zero particle image displacements than for a zero displacement, but remains constant over the whole considered particle image displacement range. This is a result of the plateau shape of the particle image that leads to a broadening of the displacement correlation peaks in comparison with those of Gaussian and ring-shaped particle images (see also Figure 7.2). Obviously, this makes the correlation result insensitive against errors that result from a non-zero particle image displacement. Nevertheless, it should be noted that the highest displacement estimation errors are generally observed for plateau-shaped particle images. Overall, for ring-shaped particle images, the estimation error is approximately one order of magnitude smaller than for Gaussian and plateau-shaped particle images over the whole range of considered

particle image displacements.
Figure 7.11 shows the detectability D as a function of the particle image displacement for Gaussian, ring- and plateau-shaped particle images.

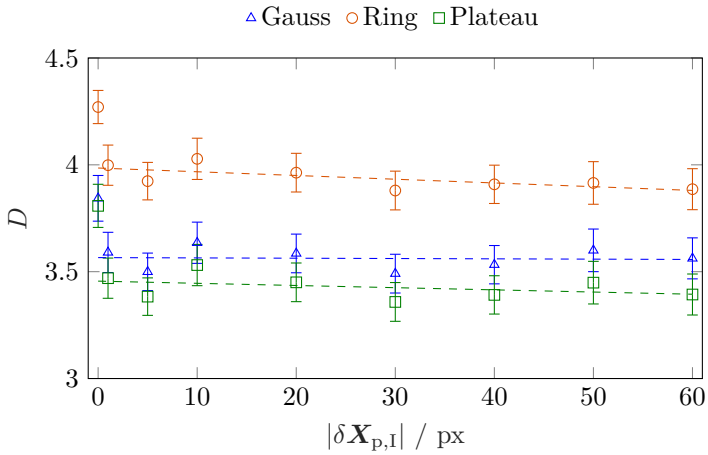

Figure 7.11.: Detectability D with 95% confidence intervals as a function of the particle image displacement for Gaussian, ring- and plateau-shaped particle images of $d_{\mathrm{p,I}} = 60\,\mathrm{px}$. Dashed lines denote fits to the respective data.

Compared to zero-displaced particle images of the same size (see also Figure 7.5(a) in section 7.1.2), the respective detectability is slightly lower for each particle image shape. A comparison of the detectability evolution for different displacement values reveals that the detectability is insensitive against a particle image displacement of up to one particle image diameter for all considered particle image shapes. Overall, the detectability for ring-shaped particle images is slightly larger than for Gaussian and plateau-shaped particle images for all considered displacement values.
Figure 7.12 shows the deviations of the displacements that are determined by the cross-correlation evaluation $\delta \boldsymbol{X}_{\mathrm{p,I,cc}}$ to the specified displacements $\delta \boldsymbol{X}_{\mathrm{p,I}}$ in horizontal direction as a function of the specified displacement magnitude. For this, the vector results of all 500 double-frame images are averaged for each particle image shape and displacement value, respectively.
Interestingly, calculated displacements of ring-shaped particle images seem to show negligible deviations. In contrast to this, calculated displacements of Gaussian and plateau-shaped particle images deviate from the specified displacements. For Gaussian particle images, the standard deviations are significantly larger compared to plateau-shaped particle images for displacements of $\delta \boldsymbol{X}_{\mathrm{p,I}} \geq 5\,\mathrm{px}$. Non-zero displacements of Gaussian particle images lead to an increase in $\tilde{\epsilon}_{\mathrm{D},2}$, which is less significant for plateau-shaped particle images (see also Figure 7.10(b)), resulting in larger standard deviations of the calculated particle image displacements.

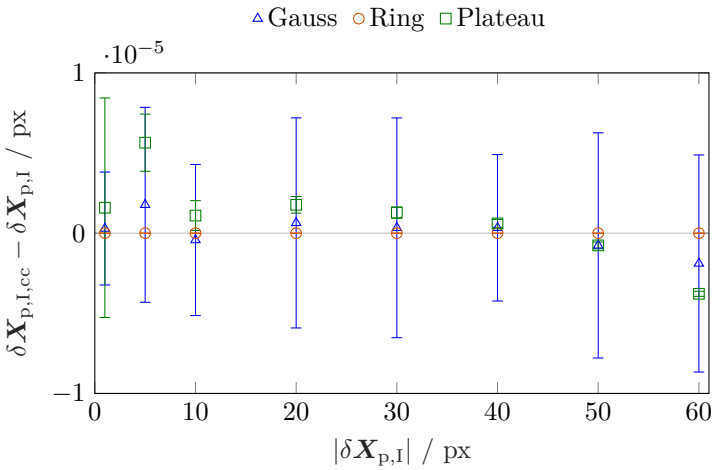

Figure 7.12.: Deviation between calculated and specified particle image displacement in horizontal direction as a function of the particle image displacement magnitude for Gaussian, ring- and plateau-shaped particle images of $d_{\mathrm{p,I}} = 60\,\mathrm{px}$.

7.2. Experimental results

The previous study shows that the usage of particles with an image size larger than 10 px leads to a reduced displacement estimation error, if they display a ring-shaped particle image instead of a plateau or Gaussian shape. Such particle images are encountered in a refractive index matched suspension with surface labelled suspension particles. It is demonstrated in the following that such suspension systems allow to study in detail the bulk behavior of suspensions of up to 5% volume fraction by means of µPIV. For this, PMMA particles of $d_{\mathrm{p,I}} = 60\,\mu\mathrm{m}$ diameter that display ring-shaped images are suspended in a ternary carrier liquid. Flow velocities of both phases of the suspension flow are determined inside the straight microchannel with trapezoidal cross-section at the location that is indicated in Figure 3.2(a). The flow field results are discussed in section 7.2.1. These show that a spatial resolution beyond the particle image size can be reached through ensemble averaging to reveal the suspension bulk dynamics. Through refractive index matching and a labelling of only the suspension particle surfaces, an enhanced optical accessibility of the suspension flow could be reached. It should be noted that the intensity signal of ring-shaped particle images is reduced compared to fully labelled particles of the same size. Thus, a suitable illumination source is needed to obtain a sufficient intensity signal. However, in this study a similar signal to noise ratio is obtained for ring-shaped particle images and for plateau-shaped

particle images of the same size as well as for standard PIV tracer particles. In this way, it was possible to measure velocity profiles of the suspension carrier liquid simultaneously with those of suspension particles. Measurement results of the one phase flow with refractive index matched carrier liquid are compared to measurements of the liquid and particle phase of the suspension flow. For this, flow field results for both phases are derived from a single recording, i.e. at the same time. An error analysis of the µPIV measurement results is performed in section 7.2.2.

7.2.1. Flow field results

The performed flow field measurements demonstrate the ability to use ring-shaped particle images in combination with standard PIV tracer particles to determine simultaneously velocity fields from both phases of a suspension flow by means of µPIV.
PIV vector fields are derived through ensemble-averaging of 500 double-frame images. Measurements are performed at 25 equidistantly spaced measurement planes. Velocity results of the one phase flow (OPF) are compared against the suspension carrier liquid (SCL) and the suspension particles (SP) velocities. Velocity fields are averaged in streamwise direction. For the one phase flow this results in the streamwise averaged velocity field that is shown over the cross-section in Figure 7.13. The microchannel walls are sketched as crosshatched regions, indicating the trapezoidal cross-sectional shape.
The velocity profile has its maximum at $z \approx 335\,\mu\text{m}$ (horizontal dashed line in Figure 7.13). The corresponding velocity profile is shown in Figure 7.14(a) for the one phase flow (OPF), the suspension carrier liquid (SCL) and the suspension particle (SP) flow.
Figures 7.14(a) and (b) show the velocity profiles of the one phase flow, the suspension carrier liquid and the suspension particle flow, respectively, at $z \approx 335\,\mu\text{m}$ and at the microchannel bisector, i.e. $y = 0\,\mu\text{m}$. Error bars indicate the overall measurement uncertainty that results from streamwise averaging and the uncertainty estimation of the particle image displacement detection at the upper limit of the 68.5% confidence interval. Further details on the error analysis are given in section 7.2.2. The in-plane velocity profile of the one phase flow (OPF) as shown in Figure 7.14(a) has a parabolic shape with a maximum velocity of $u = (0.0136 \pm 0.0001)\,\text{m}\,\text{s}^{-1}$. At the microchannel side walls, velocities deviate from zero, which results from the presence of near-wall tracer particles that move with a non-zero velocity. Due to spatial averaging inside near-wall interrogation windows and a high velocity gradient in these regions, the presence of those tracer particles results in non-zero velocities.
A comparison of the in-plane velocity profiles at $z = 335\,\mu\text{m}$ between the one phase flow (OPF) and the suspension carrier liquid (SCL) flow shows no significant differences. Suspension particles (SP) generally tend to lag behind the suspension

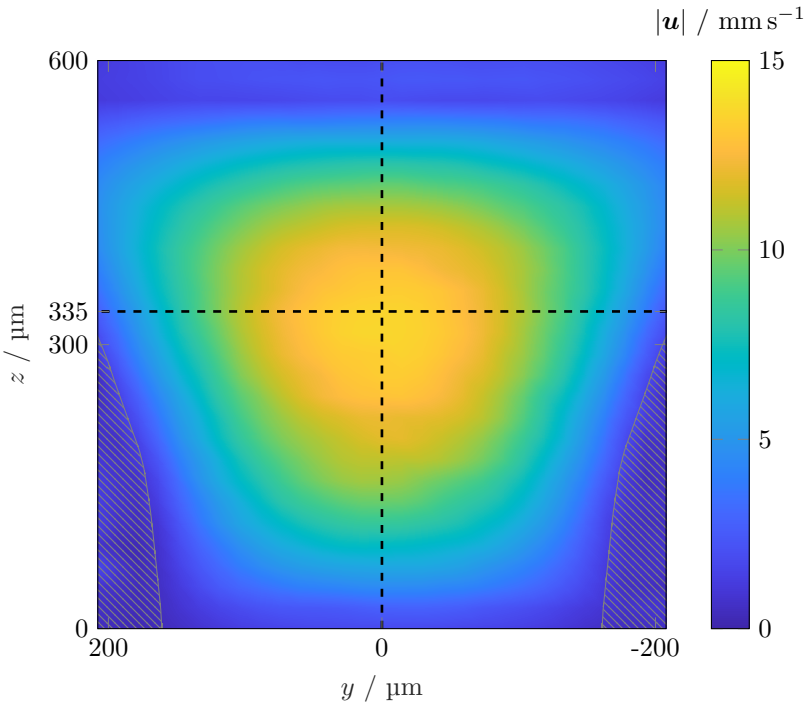

Figure 7.13.: Streamwise averaged velocity magnitudes in the microchannel cross-section obtained from µPIV measurements of the one phase flow (OPF). Velocity profiles are analysed on the x-y-plane and the x-z-plane that are indicated here by dashed lines. Channel walls are sketched as crosshatched regions.

carrier liquid (SCL) up to 7.4%. An error analysis shows that this can be confirmed within a 68.5% confidence interval (see also section 7.2.2). Liquid-particle slip velocities are expected, due to a suspension particle size which is of similar order of magnitude as the microchannel height ($d_\mathrm{p}/H = 0.1$) and is a well-known effect in Poiseuille flow for neutrally buoyant particles (Brenner, 1966; Feng et al., 1994; Guazzelli and Morris, 2011). Numerical investigations of Loisel et al. (2015) showed similar trends of such relative velocities compared to the results of the present study in suspension flows with homogeneously distributed particles and volume concentrations of up to 5%. Their results indicate that the particle slip velocity is rather a function of the Reynolds number than of the particle volume concentration in the investigated particle volume concentration regime.
The velocity profiles in the x-z-plane on the microchannel bisector ($y = 0\,\mu\mathrm{m}$, see also vertical dashed line in Figure 7.13), are shown in Figure 7.14(b). In the lower

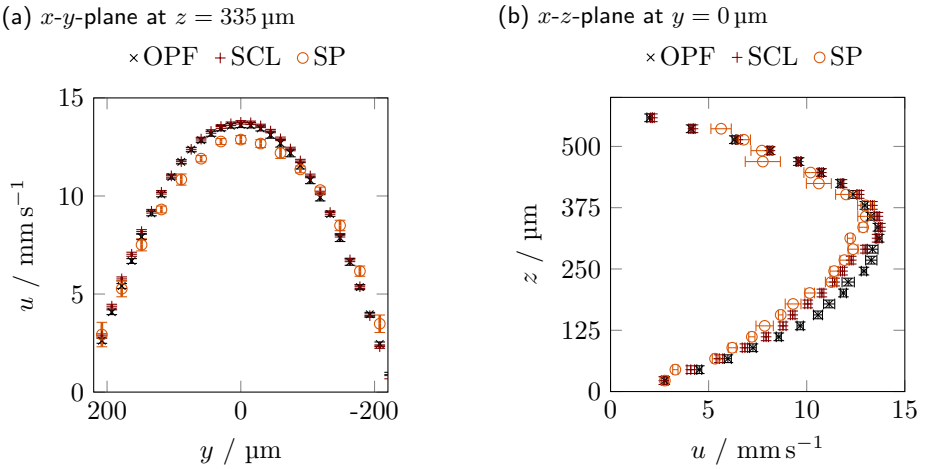

Figure 7.14.: Velocity profiles obtained from µPIV measurements of the one phase flow (OPF), the suspension carrier liquid (SCL) and the suspension particle (SP) flow (a) on the x-y-plane at $z = 335\,\mu m$ above the channel bottom and (b) on the x-z-plane in the channel bisector at $y = 0\,\mu m$. Error bars indicate uncertainties resulting from streamwise averaging and the particle image displacement detection uncertainty at the upper limit of the 68.5% confidence interval.

part of the microchannel for $z < 300\,\mu m$, the suspension carrier liquid (SCL) lags behind the one phase flow (OPF) up to 12%. In contrast to this, similar flow velocities can be observed in the top region of the microchannel for $z \gtrsim 300\,\mu m$. Suspension particles (SP) in turn have a generally lower velocity than the suspension carrier liquid (SCL) at the microchannel center, as already discussed above. This can be qualitatively understood when looking at the particle image density over the channel height, being an indication for the particle concentration distribution, see Figure 7.15. The number of segmented suspension particle images $N_{p,I}$ within the field of view during the whole time series is divided by the amount of interrogation windows N_{IW} of the resulting vector field in streamwise direction. These values are plotted for the microchannel bisector as a function of the microchannel height. A particle image is assigned to an interrogation window, if its center point is located inside the corresponding interrogation window borders. Therefore, the ratio $N_{p,I}/N_{IW}$ indicates how many particle images contribute on average to the displacement correlation peak of a single interrogation window. Clearly, particles are distributed inhomogeneously over the microchannel height. It is anticipated that a particle drift away from the channel top is induced at the inlet region where a sharp corner flow is induced, accelerating particles towards the channel bottom.

It may be noted that the data of Figure 7.15 display the particle image number density within each measurement volume.

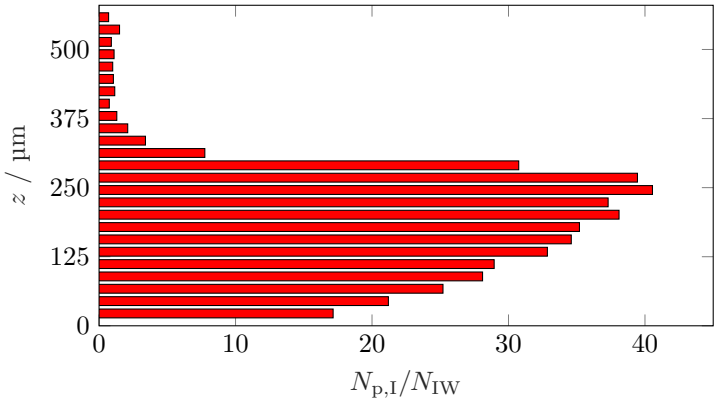

Figure 7.15.: Average number of segmented suspension particle images $N_{\mathrm{p,I}}$ divided by the number of interrogation windows in streamwise direction N_{IW} along the microchannel height at the microchannel bisector.

For $z \gtrsim 300\,\mu\mathrm{m}$, the amount of particle images per interrogation window is on average $N_{\mathrm{p,I}}/N_{\mathrm{IW}} < 5$ which is below the effective number of particle images which ensures a high detectability in PIV measurements (Keane and Adrian, 1992). This becomes evident through increasing standard deviations of suspension particle velocity data for $z > 300\,\mu\mathrm{m}$ in Figure 7.14(b). As the particle concentration is significantly reduced in this region, the velocity of the suspension carrier liquid equals that of the one phase flow here.

7.2.2. Error analysis of the flow field results

An error analysis is performed by utilizing two different approaches. Firstly, the spatial distributions of the root mean square errors (RMSE) of the streamwise velocity component are calculated. The second approach determines the measurement uncertainty U of the displacement magnitude at the upper limit (UL) and lower limit (LL) of the 68.5% and 95% confidence intervals. These are based on the empirical equation developed by Xue et al. (2014). For this, the correlation map entropy is used as representative correlation SNR metric (see also section 2.2.2.2). Thus, these uncertainty estimates are measures for the random errors of the cross-correlation evaluations. For the calculation of the RMSE distributions of the streamwise velocity component, RMS errors of consecutive vector results in streamwise direction are calculated. The resulting RMSE distributions for the one phase flow (OPF) the suspension carrier liquid (SCL) and the suspension particle (SP) flow, respectively, are shown in Figure 7.16(a) to (c) as contour plots.

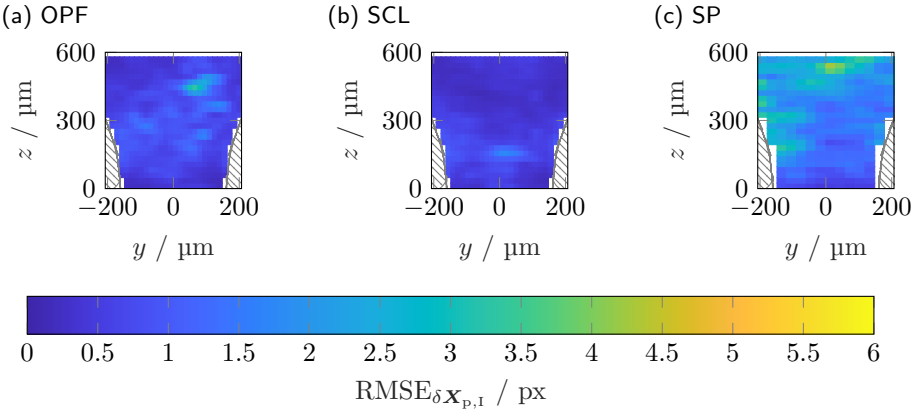

Figure 7.16.: Root mean square error distributions over the microchannel cross-section for (a) the one phase flow (OPF), (b) the suspension carrier liquid (SCL) flow and (c) the suspension particle (SP) flow.

A comparison of Figures 7.16(a) and (b) reveals that the RMSE of the one phase and the suspension carrier liquid flow are similar. It shall be noted that Figures 7.16(a) and (b) are both derived from PIV recordings of 1.19 µm fluid tracers. A comparable RMSE for these flows shows that the separation of fluid tracer and suspension particle images, as described in section 3.6.2.3, has only a minor influence on the image result. From Figures 7.16(a) to (c), average RMSE values are calculated. These are shown in Table 7.1 in displacement (px) and velocity ($\mathrm{mm\,s^{-1}}$) dimensions.
The average RMSE of the suspension particle flow is approximately one order of magnitude larger than for the one phase flow and the suspension carrier liquid flow. This is assumed to result from an inhomogeneous particle distribution over the microchannel cross-section (see also Figure 7.15) as well as interactions between suspension particles and microchannel walls and particle-particle interactions, which are known to occur in suspension flows with volume concentrations of 5%.
Measurement uncertainties at the upper and lower limit of the 68.5% and 95% confidence intervals are calculated for the ensemble-averaged cross-correlation results utilizing the empirical relation developed by Xue et al. (2014). Here, the correlation entropy is utilized to calculate uncertainty estimates for each interrogation window. Distributions of the streamwise averaged measurement uncertainties at the upper limit of the 95% confidence interval are shown in Figures 7.17(a) to (c) for the one phase flow (OPF), the suspension carrier liquid (SCL) and the suspension particle (SP) flow.
The resulting uncertainty estimates at the upper and lower limit of the 68.5% and 95% confidence intervals are averaged over all interrogation windows of all

Table 7.1.: Average root mean square error (RMSE) and measurement uncertainty U at the upper limit (UL) and lower limit (LL) of the 68.5% and 95% confidence intervals for the one phase flow (OPF), the suspension carrier liquid (SCL) flow and the suspension particle (SP) flow.

		OPF	**SCL**	**SP**
$\mathrm{RMSE}_{\delta \boldsymbol{X}_{\mathrm{p,I}}}$	/ px	$(5.8\pm2.1)\times10^{-1}$	$(3.8\pm1.3)\times10^{-1}$	1.7 ± 0.5
RMSE_{u}	/ mm s^{-1}	$(1.8\pm0.7)\times10^{-1}$	$(1.2\pm0.4)\times10^{-1}$	$(5.3\pm0.2)\times10^{-1}$
$U_{\delta \boldsymbol{X}_{\mathrm{p,I}},\mathrm{UL},68.5}$	/ px	$(2.726\pm0.004)\times10^{-1}$	$(2.724\pm0.004)\times10^{-1}$	$(2.717\pm0.009)\times10^{-1}$
$U_{\delta \boldsymbol{X}_{\mathrm{p,I}},\mathrm{LL},68.5}$	/ px	$(5.328\pm0.008)\times10^{-2}$	$(5.325\pm0.008)\times10^{-2}$	$(5.31\pm0.02)\times10^{-2}$
$U_{u,\mathrm{UL},68.5}$	/ mm s^{-1}	$(8.43\pm0.01)\times10^{-2}$	$(8.42\pm0.01)\times10^{-2}$	$(8.40\pm0.03)\times10^{-2}$
$U_{u,\mathrm{LL},68.5}$	/ mm s^{-1}	$(1.647\pm0.003)\times10^{-2}$	$(1.646\pm0.002)\times10^{-2}$	$(1.641\pm0.006)\times10^{-2}$
$U_{\delta \boldsymbol{X}_{\mathrm{p,I}},\mathrm{UL},95}$	/ px	1.754 ± 0.003	1.753 ± 0.003	1.750 ± 0.006
$U_{\delta \boldsymbol{X}_{\mathrm{p,I}},\mathrm{LL},95}$	/ px	$(2.046\pm0.003)\times10^{-2}$	$(2.045\pm0.003)\times10^{-2}$	$(2.038\pm0.007)\times10^{-2}$
$U_{u,\mathrm{UL},95}$	/ mm s^{-1}	$(5.423\pm0.009)\times10^{-1}$	$(5.419\pm0.008)\times10^{-1}$	$(5.41\pm0.01)\times10^{-1}$
$U_{u,\mathrm{LL},95}$	/ mm s^{-1}	$(6.3\pm0.1)\times10^{-3}$	$(6.32\pm0.01)\times10^{-3}$	$(6.30\pm0.02)\times10^{-3}$

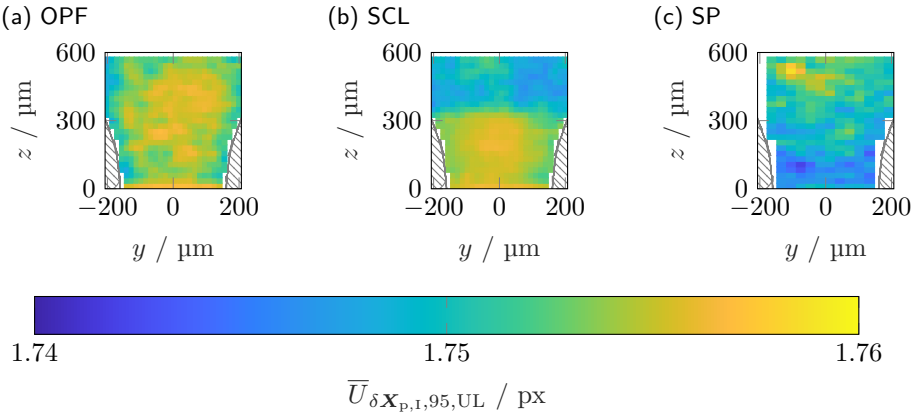

Figure 7.17.: Streamwise averaged measurement uncertainty at the upper limit of the 95% confidence interval based on the correlation entropy (Xue et al., 2014) for (a) the one phase flow (OPF), (b) the suspension carrier liquid (SCL) flow and (c) the suspension particle (SP) flow at $z = 335\,\mu\mathrm{m}$.

measurement planes. The results are also shown in Table 7.1 in displacement (px) and velocity (mm s^{-1}) dimensions. The average uncertainty estimates are at least one order of magnitude smaller than the maximum streamwise velocities. Furthermore, the uncertainty estimates are similar for all particle image shapes considered. A slightly increased uncertainty for the suspension carrier liquid (Fig-

ure 7.17(b)) below $z \leq 300\,\mu m$ can be associated with an increased amount of detected suspension particles in this region. However, these deviations are below 1%.
Thus, the presence of a slip velocity between carrier liquid and suspension particles can be confirmed within a 68.5% confidence interval for which the uncertainty is approximately one order of magnitude smaller than for measured slip velocities (see also the velocity profiles shown in Figure 7.14(a) and (b)). Furthermore, the usage of large ring-shaped particle images for the cross-correlation evaluation does not lead to a significant increase of the measurement uncertainty within the considered uncertainty bounds.

7.3. Conclusion

Overall, it is demonstrated that refractive index matched and surface labelled suspension particles open up the possibility to investigate both suspension and carrier bulk dynamics simultaneously by means of µPIV. The size sensitivity of Gaussian, ring- and plateau-shaped particle images on cross-correlation based PIV evaluations is compared. When particle images become large compared to standard PIV tracer particle images, accuracy and reliability of cross-correlations on resulting standard Gaussian or plateau-shaped particle images are known to decrease. At higher particle volume fractions, the optical accessibility of such suspension flows is usually limited, as well. To overcome this, a refractive index matching of a carrier fluid to PMMA suspension particles is performed. Furthermore, a surface labelling of such suspension particles leads to ring-shaped particle images. The suitability of such particle images with regard to a PIV cross-correlation evaluation is investigated in this work. For all parameter studies, cross-correlation results of synthetic particle images are evaluated by means of displacement estimation error and detectability for particle image diameters between $1\,px \leq d_{p,I} \leq 60\,px$. The study is based on Monte Carlo simulations with 500 double-frame images for each particle image diameter. Particle images are cross-correlated using a commercial PIV evaluation algorithm.
It is shown that the usage of ring-shaped particle images leads to a reduced displacement estimation error for particle image diameters beyond $d_{p,I} = 10\,px$ compared to Gaussian and plateau-shaped particle images while there is no significant difference in the detectability for different particle image shapes. This reduction in displacement estimation error of ring-shaped particle images is related to increased intensity gradients at the particle image rim in combination with a nearly transparent center region. This leads to a faster decorrelation and thus reduces the correlation peak width. When image noise is added, the overall estimation error is increased by several orders of magnitude due to an increase in random errors (here an increase of four orders of magnitude is observed for 8.5% image noise). Thus, special attention has to be spent on the elimination of image noise

during pre-processing of experimental data, since image noise generally leads to an increased displacement estimation error for all investigated particle image shapes at various particle image diameters. However, also in this situation the usage of ring-shaped particle images leads to a reduced displacement estimation error compared to Gaussian and plateau-shaped particle images.
Furthermore, the influence of particle images being intersected at the interrogation window border is investigated. For this, synthetic images with one, three and five intersected particle images out of five within each interrogation window are evaluated for Gaussian, ring- and plateau-shaped particle images. While the displacement estimation error of ring-shaped particle images appears to be insensitive to particle image intersection at the interrogation window border, a strong reduction in estimation error is observed for Gaussian and plateau-shaped particle images with increasing amount of intersected particle images. This can be explained by intensity jumps of particle images that occur at the intersection line along the interrogation window border. These intensity jumps, which are much more prominent for Gaussian and plateau-shaped particle images, lead to a reduction of the correlation peak width and hence a reduced estimation error.
When a non-zero particle image displacement is considered, the displacement estimation error increases with the displacement value for Gaussian and ring-shaped particle images. In contrast to this, the displacement estimation error of plateau-shaped particle images is insensitive against a non-zero particle image displacement within the investigated range. Compared to a zero particle image displacement, the displacement estimation error increases for all considered particle image shapes. However, the displacement estimation error is approximately one order of magnitude smaller for ring-shaped particle images than for Gaussian and plateau-shaped particle images for all particle image displacements considered.
The quality of a PIV evaluation can be evaluated from the displacement estimation error and the detectability. The detectability is known to depend on the signal to noise ratio, the effective number of particle images, the correlated ensemble size and the particle image density. In this work the first three parameters are fixed for all particle image shapes. Therefore, no significant difference in detectability is observed between different particle image shapes for particle images located inside the interrogation window. This holds also true for particle images of $d_{\mathrm{p,I}} = 60\,\mathrm{px}$, when a non-zero particle image displacement is considered. However, the detectability is found to decrease with increasing particle image size. This is due to a rise in the particle image density N_{ppp} associated with an increasing particle image diameter. Secondly, a decrease in detectability is observed for particle image diameters below $d_{\mathrm{p,I}} = 10\,\mathrm{px}$ with image noise of 8.5%. That is, because intensity values are averaged over a full pixel leading to a reduction in intensity peaks, especially for small particle images. This leads to a significant decrease in signal to noise ratio and hence a reduced detectability.
Furthermore, the detectability is investigated for a growing number of intersected particle images, keeping the total number of particle images within the interroga-

tion window constant. Here, a non-linear behavior is observed with a minimum in detectability for a similar number of particle images located inside the interrogation window and on the interrogation window border. It is assumed that for K_5 being approximately equal to half the total amount of particle images per interrogation window the probability for particle images inside the interrogation window to correlate with intersected particle images is increased, leading to an increase in secondary correlation peak values.
Summed up, the usage of refractive index matched and surface labelled particles not only enhances optical accessibility, but also leads to a reduction of the displacement estimation error and a similar or even better detectability compared to Gaussian or plateau-shaped particle images. This holds true also for situations where intersected particle images at interrogation window borders occur.
Refractive index matching led to an enhanced optical accessibility of the system. Combined with a labelling, the accuracy and reliability of the µPIV evaluation are enhanced compared to Gaussian particle images. It is demonstrated theoretically and experimentally that such particle systems are suitable to study the bulk dynamics of suspension flows. Measurements are performed with surface labelled and refractive index matched suspension particles that display ring-shaped particle images. Hence, the particle bulk dynamics of a 5 Vol.-% suspension is measured together with the carrier liquid flow and the measurement uncertainty is estimated. By this, liquid-particle slip velocities are determined.
Overall, it is demonstrated that µPIV measurements utilizing ring-shaped particle images bring along advantageous properties from both, a theoretical and practical point of view. Additionally, the usage of ring-shaped particle images allows to investigate suspension bulk dynamics by measuring velocity fields of both, the suspended and the continuous phase, simultaneously and with an overall uncertainty that is in the same order of magnitude as for standard µPIV measurements. This is considered to be an important step for further µPIV measurements in a variety of suspension flows. For studies of even higher volume fractions, a well defined temperature control will be required to achieve a matching of the refractive index between particles and carrier liquid up to the fourth digit (Wiederseiner et al., 2011).

8. Summary of conclusions and outlook

This work investigates the ability of a sharp-corner serpentine microchannel to fractionate particles smaller than 10 µm with regard to their size and density by experimental as well as numerical methods. Additionally, a new extension of the µPIV measurement technique is presented that enables the simultaneous determination of the liquid and the particulate phase of a suspension.
The fractionation principle that is utilized in such a sharp-corner serpentine microchannel relies on the spatial separation of particles due to a property dependent force equilibrium. With this, particles of different properties are driven onto spatially separated trajectories at the same bulk Reynolds number.
To investigate the multi-dimensional fractionation potential of a sharp-corner serpentine microchannel, the locations of particle trajectories are determined by long-exposure measurements. For these, polystyrene, melamine and silica particles with diameters of $d_\mathrm{p} \approx 3.5\,\mu\mathrm{m}$ and $d_\mathrm{p} \approx 10\,\mu\mathrm{m}$ are investigated at various bulk Reynolds numbers. These investigations show that the sharp-corner serpentine microchannel has a high potential to fractionate particles of different materials with regard to the considered sizes between $63 \leq \mathrm{Re_b} \leq 90$. In this bulk Reynolds number range larger particles are focused on two visible streaks, while smaller particles are focused on one, spatially separated visible streak. Furthermore, a significant influence of the particle density on the location of particle trajectories is found for particles with $d_\mathrm{p} \approx 10\,\mu\mathrm{m}$ diameter at bulk Reynolds numbers above $\mathrm{Re_b} \geq 105$. Here, the corresponding particles develop one visible streak that is spatially separated at certain locations inside a serpentine loop. The particle focusing behavior of sub-micron polystyrene particles with diameters down to $0.45\,\mu\mathrm{m}$ is investigated by long-exposure measurements, as well. It is revealed that sub-micron particles may also develop two distinct particle streaks below a certain bulk Reynolds number. In contrast to micron particles, for sub-micron particles it is observed that an increase of the bulk Reynolds number leads to a disintegration of particle streaks before the transition towards one visible streak is finished. To understand this behavior, further studies are necessary to investigate in detail the underlying liquid flow field as well as the balance of forces that are relevant for the motion of sub-micron particles at such bulk Reynolds numbers.
A more detailed investigation of the three-dimensional distributions of particles inside one serpentine loop is performed by means of Astigmatism Particle

Tracking Velocimetry (APTV). With this, the size fractionation performance of polystyrene particles with $d_p = 3.55\,\mu m$ and $d_p = 9.89\,\mu m$ diameter is determined to nearly reach 100%. Furthermore, the three-dimensional reconstructions of particle distributions reveal that particles develop distinct trajectories along the microchannel height. Thus, instead of developing only two or one visible trajectories as anticipated in existing experimental literature, particles allocate in a 2×2 or 1×2 configuration. Additionally, the analysis of three-dimensional distributions of particles with different densities show that this density difference does not lead to a significant height difference of corresponding trajectories. Thus, an additional possibility to realize density fractionation through sedimentation effects inside serpentine microchannels of the present design cannot be confirmed. To deepen the understanding of the acting forces that are relevant to maintain stable particle trajectories at a constant bulk Reynolds number, numerical simulations are performed. Fully coupled simulation results from a coupled Lattice Boltzmann Method-Discrete Element Method provided by cooperation partners are carefully analyzed and interpreted. These simulations are performed for polystyrene particles with $d_p = 9.89\,\mu m$ diameter at bulk Reynolds numbers of $Re_b = 33$ and $Re_b = 100$. Here, particles develop trajectories in a 2×2 and 1×2 configuration, as also observed from experiments. The results reveal that in these flow configurations the shear-gradient force and the drag force are dominant for the lateral particle motion. Furthermore, results indicate that additional forces such as the wall lift force may be relevant for the development of distinct particle trajectories, as well. A one-way coupled Euler-Lagrange approach is utilized to simulate polystyrene particles of $d_p = 3.55\,\mu m$ diameter up to a bulk Reynolds number of $Re_b = 67$. In this bulk Reynolds number regime, particles develop trajectories in a 2×2 configuration. A comparison with experimental results shows a good agreement, both for the underlying liquid velocity field solutions as well as for the simulated particle trajectories. An evaluation of individual force contributions also confirms the importance of the shear-gradient force that acts lateral to the particle main flow direction. In contrast to larger particles, the lateral drag force component is of minor importance.

The analysis of individual force contributions that act on suspended particles emphasizes the necessity to determine the flow fields of both, the particulate and the liquid phase of a suspension. Thus, a new extension of the micro Particle Image Velocimetry (µPIV) measurement technique is developed and evaluated that addresses this challenge. The presented approach is based on the usage of ring-shaped images of particles that are significantly larger than images of commonly used tracer particles. These are generated due to a refractive index matching of a ternary carrier liquid to polymethylmethacrylate (PMMA) particles in combination with a custom surface labelling procedure. This grants a good optical accessibility of suspension flows. An investigation based on synthetically generated particle images shows the superiority of ring-shaped particle images compared to Gaussian or plateau-shaped particle images in

terms of accuracy above $d_{\mathrm{p,I}} \geq 10\,\mathrm{px}$ particle image diameter and for a zero displacement between correlated frames. Additionally, the investigation of the influence of particle images that are intersected at interrogation window borders reveals that ring-shaped particle images are rather insensitive against such an intersection. In contrast to this, the accuracy decreases with increasing particle image displacement, if particles display a Gaussian or ring-shaped image, whereas plateau-shaped particle images are rather insensitive against a non-zero displacement. However, the accuracy is still one order of magnitude higher for ring-shaped particle images than for Gaussian and plateau-shaped particle images for the considered displacement values. A comparison of the detectability of various cross-correlation results shows a similar performance of all three considered particle image shapes. The suitability of ring-shaped particle images for real, experimental measurement situations is demonstrated as well. Here, ring-shaped particle images are used together with standard tracers to measure the bulk dynamics of both phases of a suspension simultaneously.

The investigations that are summarized in the preceding also lead to follow up questions. With regard to the multi-dimensional fractionation especially the quantification of the density fractionation performance is an open task. This is also the basis for the determination of two-dimensional partition curves as they are proposed by Schach et al. (2019). However, these typically utilize samples with continuous distributions of a certain particle characteristic. Thus, for a comprehensive study of the multi-dimensional fractionation performance, particle probes of well-known size and density distributions and with suitable fluorescent characteristics need to be investigated in the future. Whereas fluorescent microparticles with different sizes are commercially available, the availability of corresponding particles with different densities, i.e. made from different materials, is considerably limited. This challenge may be solved by designing a serpentine microchannel with several suitable outlet geometries. This would open the opportunity to separate suspended particles of an initial batch into several fractions that could be analyzed separately. With this an in situ observation inside individual serpentine loops would not be necessary, which also results in lower requirements for the fluorescence properties of individual particle fractions. Furthermore, a comparison of force balances of particles with different densities is necessary to fully understand the development of spatially separated trajectories. A change of the particle density is expected to influence the particle centrifugal force. Thus, a detailed comparison of force balances would be interesting to investigate if this induces also differences in the shear-gradient force and the drag force.
Another challenge is to analyze the role of the wall lift force during the particle motion inside a serpentine microchannel in the future. A suitable formulation for the wall lift force in the vicinity of corner flows does not exist up to date. However, a potential starting point for the implementation of a suitable wall lift force could

be the work of Zeng et al. (2005). There, an empirical model is provided that is based on direct numerical simulations and that considers the distance of a particle to a straight wall as well as the particle Reynolds number.
To determine the bulk dynamics of the particulate and the liquid phase of a suspension also experimentally, an extension of the µPIV measurement technique is developed that utilizes ring-shaped particle images. During experimental studies it is observed that such ring-shaped particle images defocus faster with increasing out-of-plane positions than particles with a plateau-shaped image of the same size. Thus, it seems to be questionable that the widely used formulation for the depth of correlation of a µPIV measurement (Olsen and Adrian, 2000) is also valid for such ring-shaped particle images. That is because the commonly used formulation utilizes the actual particle diameter for the calculation. Instead, a proportionality of the depth of correlation to the particle image ring width should be investigated in the future.
Overall, the present thesis deepens the understanding of the particle dynamics inside sharp-corner serpentine microchannel flows. Furthermore, parameters are identified at which multi-dimensional fractionation with respect to the particle size and density is promising. Moreover, the present thesis provides a method that enables detailed experimental investigations of both phases of a suspension flow.

Bibliography

[1] R. J. Adrian. "Particle-Imaging Techniques for Experimental Fluid Mechanics". In: *Annual Review of Fluid Mechanics* 23.1 (1991), pp. 261–304. ISSN: 0066-4189. DOI: 10.1146/annurev.fl.23.010191.001401.

[2] R. J. Adrian and J. Westerweel. *Particle Image Velocimetry*. Cambridge Aerospace Series. Cambridge University Press, 2011. ISBN: 9780521440080.

[3] C. K. Aidun et al. "Direct analysis of particulate suspensions with inertia using the discrete Boltzmann equation". In: *Journal of Fluid Mechanics* 373 (1998), pp. 287–311. ISSN: 00221120. DOI: 10.1017/S0022112098002493.

[4] I. Ali et al. "Phytogenic magnetic nanoparticles for wastewater treatment: A review". In: *RSC Advances* 7.64 (2017), pp. 40158–40178. ISSN: 20462069. DOI: 10.1039/c7ra04738j.

[5] S. Anders et al. "Spectral random masking: a novel dynamic masking technique for PIV in multiphase flows". In: *Experiments in Fluids* 60.4 (2019), pp. 1–6. ISSN: 07234864. DOI: 10.1007/s00348-019-2703-8.

[6] E. S. Asmolov. "The inertial lift on a spherical particle in a plane Poiseuille flow at large channel Reynolds number". In: *Journal of Fluid Mechanics* 381.1 (Feb. 1999), pp. 63–87. ISSN: 0022-1120. DOI: 10.1017/S0022112098003474.

[7] T. R. Auton et al. "The force exerted on a body in inviscid unsteady non-uniform rotational flow". In: *Journal of Fluid Mechanics* 197 (1988), pp. 241–257. ISSN: 14697645. DOI: 10.1017/S0022112088003246.

[8] Z. Baghban Taraghdari et al. "A Review on Bioengineering Approaches to Insulin Delivery: A Pharmaceutical and Engineering Perspective". In: *Macromolecular Bioscience* 19.4 (2019), pp. 1–21. ISSN: 16165195. DOI: 10.1002/mabi.201800458.

[9] B. C. Bailey and M. Yoda. "An aqueous low-viscosity density- and refractive index-matched suspension system". In: *Experiments in Fluids* 35.1 (2003), pp. 1–3. ISSN: 07234864. DOI: 10.1007/s00348-003-0598-9.

[10] M. Barasinski and G. Garnweitner. "Restricted and Unrestricted Migration Mechanisms of Silica Nanoparticles in Agarose Gels and Their Utilization for the Separation of Binary Mixtures". In: *Journal of Physical Chemistry C* 124.9 (2020), pp. 5157–5166. ISSN: 19327455. DOI: 10.1021/acs.jpcc.9b10644.

[11] A. A. S. Bhagat et al. “Continuous particle separation in spiral microchannels using dean flows and differential migration”. In: *Lab on a Chip* 8.11 (2008), p. 1906. ISSN: 1473-0197. DOI: 10.1039/b807107a.

[12] S. Bhattacharya et al. “Particle image velocimetry (PIV) uncertainty quantification using moment of correlation (MC) plane”. In: *Measurement Science and Technology* 29.11 (2018). ISSN: 13616501. DOI: 10.1088/1361-6501/aadfb4.

[13] S. Blahout et al. “On the 3D Distribution and Size Fractionation of Microparticles in a Serpentine Microchannel”. In: *Microfluidics and Nanofluidics* (2020), pp. 1–10. ISSN: 1613-4990. DOI: 10.1007/s10404-020-2326-7.

[14] S. Blahout et al. “On the micro-PIV accuracy and reliability utilizing non-Gaussian particle images”. In: *Experiments in Fluids* 62.9 (Sept. 2021), p. 191. ISSN: 0723-4864. DOI: 10.1007/s00348-021-03283-8.

[15] F. Blanc et al. “Microstructure in sheared non-Brownian concentrated suspensions”. In: *Journal of Rheology* 57.1 (2013), pp. 273–292. ISSN: 0148-6055. DOI: 10.1122/1.4766597.

[16] C. J. Bourdon et al. “The depth of correlation in micro-PIV for high numerical aperture and immersion objectives”. In: *Journal of Fluids Engineering, Transactions of the ASME* 128.4 (2006), pp. 883–886. ISSN: 00982202. DOI: 10.1115/1.2201649.

[17] H. Brenner. “Hydrodynamic Resistance of Particles at Small Reynolds Numbers”. In: *Advances in Chemical Engineering*. Ed. by T. B. Drew et al. Vol. 6. Advances in Chemical Engineering. Academic Press, 1966, pp. 287–438. DOI: 10.1016/S0065-2377(08)60277-X.

[18] W. P. Breugem. “A second-order accurate immersed boundary method for fully resolved simulations of particle-laden flows”. In: *Journal of Computational Physics* 231.13 (2012), pp. 4469–4498. ISSN: 10902716. DOI: 10.1016/j.jcp.2012.02.026.

[19] P. Brockmann and J. Hussong. “On the calibration of Astigmatism particle tracking velocimetry for suspensions of different volume fractions”. In: *Experiments in Fluids* 62.1 (2021), pp. 1–11. ISSN: 14321114. DOI: 10.1007/s00348-020-03120-4.

[20] P. Brockmann et al. “Utilizing the ball lens effect for astigmatism particle tracking velocimetry”. In: *Experiments in Fluids* 61.2 (2020), pp. 1–19. ISSN: 14321114. DOI: 10.1007/s00348-020-2900-5.

[21] M. L. Byron and E. A. Variano. “Refractive-index-matched hydrogel materials for measuring flow-structure interactions”. In: *Experiments in Fluids* 54.2 (2013). ISSN: 07234864. DOI: 10.1007/s00348-013-1456-z.

[22] I. B. Celik et al. “Procedure for estimation and reporting of uncertainty due to discretization in CFD applications”. In: *Journal of Fluids Engineering, Transactions of the ASME* 130.7 (2008), pp. 0780011–0780014. ISSN: 00982202. DOI: 10.1115/1.2960953.

[23] J. J. Charonko and P. P. Vlachos. “Estimation of uncertainty bounds for individual particle image velocimetry measurements from cross-correlation peak ratio”. In: *Measurement Science and Technology* 24.6 (2013). ISSN: 13616501. DOI: 10.1088/0957-0233/24/6/065301.

[24] B. Chen et al. “Experimental studies on transient features of natural convection in particles suspensions”. In: *International Journal of Heat and Mass Transfer* 48.14 (2005), pp. 2933–2942. ISSN: 00179310. DOI: 10.1016/j.ijheatmasstransfer.2004.11.016.

[25] C. Cierpka et al. “A simple single camera 3C3D velocity measurement technique without errors due to depth of correlation and spatial averaging for microfluidics”. In: *Measurement Science and Technology* 21.4 (Apr. 2010), p. 045401. ISSN: 0957-0233. DOI: 10.1088/0957-0233/21/4/045401.

[26] C. Cierpka et al. “On the calibration of astigmatism particle tracking velocimetry for microflows”. In: *Measurement Science and Technology* 22.1 (Jan. 2011), p. 015401. ISSN: 0957-0233. DOI: 10.1088/0957-0233/22/1/015401.

[27] J. M. Coupland and C. J. Pickering. “Particle image velocimetry: Estimation of measurement confidence at low seeding densities”. In: *Optics and Lasers in Engineering* 9.3-4 (Jan. 1988), pp. 201–210. ISSN: 01438166. DOI: 10.1016/S0143-8166(98)90003-3.

[28] P. A. Cundall and O. D. L. Strack. “A discrete numerical model for granular assemblies”. In: *Géotechnique* 29.1 (Mar. 1979), pp. 47–65. ISSN: 0016-8505. DOI: 10.1680/geot.1979.29.1.47.

[29] D. d’Humières. “Multiple–relaxation–time lattice Boltzmann models in three dimensions”. In: *Philosophical Transactions of the Royal Society of London. Series A: Mathematical, Physical and Engineering Sciences* 360.1792 (Mar. 2002). Ed. by P. V. Coveney et al., pp. 437–451. ISSN: 1364-503X. DOI: 10.1098/rsta.2001.0955.

[30] R. S. Davuluri et al. “A drag coefficient model for Lagrangian particle dynamics relevant to high-speed flows”. In: *International Journal of Heat and Fluid Flow* 87.September 2020 (2021), p. 108706. ISSN: 0142727X. DOI: 10.1016/j.ijheatfluidflow.2020.108706.

[31] W. R. Dean. “Fluid Motion in a Curved Channel”. In: *Proceedings of the Royal Society A: Mathematical, Physical and Engineering Sciences* 121.787 (Nov. 1928), pp. 402–420. ISSN: 1364-5021. DOI: 10.1098/rspa.1928.0205.

[32] D. Di Carlo. “Inertial microfluidics”. In: *Lab on a Chip* 9.21 (2009), pp. 3038–3046. ISSN: 14730189. DOI: 10.1039/b912547g.

[33] D. Di Carlo et al. “Continuous inertial focusing, ordering, and separation of particles in microchannels”. In: *Proceedings of the National Academy of Sciences of the United States of America* 104.48 (2007), pp. 18892–18897. ISSN: 00278424. DOI: 10.1073/pnas.0704958104.

[34] D. Di Carlo et al. “Equilibrium separation and filtration of particles using differential inertial focusing”. In: *Analytical Chemistry* 80.6 (2008), pp. 2204–2211. ISSN: 00032700. DOI: 10.1021/ac702283m.

[35] D. Drew et al. “The analysis of virtual mass effects in two-phase flow”. In: *International Journal of Multiphase Flow* 5.4 (1979), pp. 233–242. ISSN: 03019322. DOI: 10.1016/0301-9322(79)90023-5.

[36] D. A. Drew and R. T. Lahey. “The virtual mass and lift force on a sphere in rotating and straining inviscid flow”. In: *International Journal of Multiphase Flow* 13.1 (Jan. 1987), pp. 113–121. ISSN: 03019322. DOI: 10.1016/0301-9322(87)90011-5.

[37] A. Eckstein and P. P. Vlachos. “Digital particle image velocimetry (DPIV) robust phase correlation”. In: *Measurement Science and Technology* 20.5 (2009). ISSN: 09570233. DOI: 10.1088/0957-0233/20/5/055401.

[38] A. C. Eckstein et al. “Phase correlation processing for DPIV measurements”. In: *Experiments in Fluids* 45.3 (Sept. 2008), pp. 485–500. ISSN: 0723-4864. DOI: 10.1007/s00348-008-0492-6.

[39] L. L. Fan et al. “Continuous size-based separation of microparticles in a microchannel with symmetric sharp corner structures”. In: *Biomicrofluidics* 8.2 (2014). ISSN: 19321058. DOI: 10.1063/1.4870253.

[40] L.-L. Fan et al. “Continuous 3D particle focusing in a microchannel with curved and symmetric sharp corner structures”. In: *Journal of Micromechanics and Microengineering* 25.3 (Mar. 2015), p. 035020. ISSN: 0960-1317. DOI: 10.1088/0960-1317/25/3/035020.

[41] J. Feng et al. “Direct simulation of initial value problems for the motion of solid bodies in a Newtonian fluid. part 2. Couette and Poiseuille flows”. In: *Journal of Fluid Mechanics* 277 (1994), pp. 271–301. ISSN: 14697645. DOI: 10.1017/S0022112094002764.

[42] J. Ferziger and M. Peric. *Numerische Strömungsmechanik*. Berlin, Heidelberg: Springer Berlin Heidelberg, 2008. ISBN: 978-3-540-67586-0. DOI: 10.1007/978-3-540-68228-8.

[43] W. Fornari et al. “Suspensions of finite-size neutrally buoyant spheres in turbulent duct flow”. In: *Journal of Fluid Mechanics* 851 (2018), pp. 148–186. ISSN: 14697645. DOI: 10.1017/jfm.2018.490.

[44] S. Funatani et al. “Simultaneous measurement of temperature and velocity using two-colour LIF combined with PIV with a colour CCD camera and its application to the turbulent buoyant plume”. In: *Measurement Science and Technology* 15.5 (2004), pp. 983–990. ISSN: 09570233. DOI: 10.1088/0957-0233/15/5/030.

[45] L. Gloag et al. “Advances in the Application of Magnetic Nanoparticles for Sensing”. In: *Advanced Materials* 31.48 (2019), pp. 1–26. ISSN: 15214095. DOI: 10.1002/adma.201904385.

[46] W. R. Goossens. “Review of the empirical correlations for the drag coefficient of rigid spheres”. In: *Powder Technology* 352 (2019), pp. 350–359. ISSN: 1873328X. DOI: 10.1016/j.powtec.2019.04.075.

[47] D. R. Gossett and D. D. Carlo. “Particle Focusing Mechanisms in Curving Confined Flows”. In: *Analytical Chemistry* 81.20 (Oct. 2009), pp. 8459–8465. ISSN: 0003-2700. DOI: 10.1021/ac901306y.

[48] E. Guazzelli and J. F. Morris. *A physical introduction to suspension dynamics*. Vol. 45. Cambridge University Press, 2011. ISBN: 9781139503938.

[49] S. J. Haam et al. “Laser Doppler anemometry measurements in an index of refraction matched column in the presence of dispersed beads: Part I”. In: *International Journal of Multiphase Flow* 26.9 (2000), pp. 1401–1418. ISSN: 03019322. DOI: 10.1016/S0301-9322(99)00094-4.

[50] Y. A. Hassan and E. E. Dominguez-Ontiveros. “Flow visualization in a pebble bed reactor experiment using PIV and refractive index matching techniques”. In: *Nuclear Engineering and Design* 238.11 (2008), pp. 3080–3085. ISSN: 00295493. DOI: 10.1016/j.nucengdes.2008.01.027.

[51] X. He et al. “Analytic solutions of simple flows and analysis of nonslip boundary conditions for the lattice Boltzmann BGK model”. In: *Journal of Statistical Physics* 87.1-2 (1997), pp. 115–136. ISSN: 00224715. DOI: 10.1007/BF02181482.

[52] M. van Hinsberg et al. “An efficient, second order method for the approximation of the Basset history force”. In: *Journal of Computational Physics* 230.4 (Feb. 2011), pp. 1465–1478. ISSN: 00219991. DOI: 10.1016/j.jcp.2010.11.014.

[53] B. P. Ho and L. G. Leal. “Inertial migration of rigid spheres in two-dimensional unidirectional flows”. In: *Journal of Fluid Mechanics* 65.2 (Aug. 1974), pp. 365–400. ISSN: 0022-1120. DOI: 10.1017/S0022112074001431.

[54] D. Jiang et al. “Numerical simulation of particle migration in different contraction–expansion ratio microchannels”. In: *Microfluidics and Nanofluidics* 23.1 (Jan. 2019), p. 7. ISSN: 1613-4982. DOI: 10.1007/s10404-018-2176-8.

[55] M. C. Jo and R. Guldiken. "Active density-based separation using standing surface acoustic waves". In: *Sensors and Actuators, A: Physical* 187 (2012), pp. 22–28. ISSN: 09244247. DOI: 10.1016/j.sna.2012.08.020.

[56] H. T. Kazerooni et al. "Inertial migration in dilute and semidilute suspensions of rigid particles in laminar square duct flow". In: *Physical Review Fluids* 2.8 (Aug. 2017), p. 084301. ISSN: 2469-990X. DOI: 10.1103/PhysRevFluids.2.084301.

[57] R. D. Keane and R. J. Adrian. "Optimization of particle image velocimeters. I. Double pulsed systems Optimization of particle image ve I oci m e te rs. Part I: Double pulsed systems". In: *Meas. Sci. Technol. Meas. Sci. Technol* 1.1 (1990), pp. 1202–1215.

[58] R. D. Keane and R. J. Adrian. "Theory of cross-correlation analysis of PIV images". In: *Applied Scientific Research* 49.3 (July 1992), pp. 191–215. ISSN: 0003-6994. DOI: 10.1007/BF00384623.

[59] S. Khirevich et al. "Coarse-and fine-grid numerical behavior of MRT/TRT lattice-Boltzmann schemes in regular and random sphere packings". In: *Journal of Computational Physics* 281 (2015), pp. 708–742. ISSN: 10902716. DOI: 10.1016/j.jcp.2014.10.038.

[60] L. S. Klyachko. "Heating and ventilation". In: *USSR Journal Otopl. i Ventil* 4 (1934).

[61] S. Kordel et al. "Combined density gradient and velocity field measurements in transient flows by means of Differential Interferometry and Long-range μ PIV". In: *Experiments in Fluids* 57.9 (2016), pp. 1–11. ISSN: 07234864. DOI: 10.1007/s00348-016-2224-7.

[62] J. Kottmeier et al. "Accelerated Particle Separation in a DLD Device at Re $>$ 1 Investigated by Means of µPIV". In: *Micromachines* 10.11 (Nov. 2019), p. 768. ISSN: 2072-666X. DOI: 10.3390/mi10110768.

[63] A. G. Koutsiaris et al. "Microscope PIV for velocity-field measurement of particle suspensions flowing inside glass capillaries". In: *Measurement Science and Technology* 10.11 (1999), pp. 1037–1046. ISSN: 09570233. DOI: 10.1088/0957-0233/10/11/311.

[64] V. M. Kumar and C. V. Venkatesh. "A comprehensive review on material selection, processing, characterization and applications of aluminium metal matrix composites". In: *Materials Research Express* 6.7 (2019). ISSN: 20531591. DOI: 10.1088/2053-1591/ab0ee3.

[65] B. Kwak et al. "Hydrodynamic blood cell separation using fishbone shaped microchannel for circulating tumor cells enrichment". In: *Sensors and Actuators, B: Chemical* 261 (2018), pp. 38–43. ISSN: 09254005. DOI: 10.1016/j.snb.2018.01.135.

[66] T. Leistner et al. “Selective separation using fluid-liquid interfaces”. In: *Materials Science Forum* 959 MSF (2019), pp. 113–124. ISSN: 16629752. DOI: 10.4028/www.scientific.net/MSF.959.113.

[67] S. Li et al. “Solvent-Processed Metallic Lithium Microparticles for Lithium Metal Batteries”. In: *ACS Applied Energy Materials* 2.3 (2019), pp. 1623–1628. ISSN: 25740962. DOI: 10.1021/acsaem.9b00107.

[68] R. Lima et al. “Confocal micro-PIV measurements of three-dimensional profiles of cell suspension flow in a square microchannel”. In: *Measurement Science and Technology* 17.4 (2006), pp. 797–808. ISSN: 13616501. DOI: 10.1088/0957-0233/17/4/026.

[69] R. Lindken and W. Merzkirch. “A novel PIV technique for measurements in multiphase flows and its application to two-phase bubbly flows”. In: *Experiments in Fluids* 33.6 (2002), pp. 814–825. ISSN: 07234864. DOI: 10.1007/s00348-002-0500-1.

[70] L. Liu et al. “Hydrodynamic separation by changing equilibrium positions in contraction–expansion array channels”. In: *Microfluidics and Nanofluidics* 23.4 (Apr. 2019), pp. 1–12. ISSN: 1613-4982. DOI: 10.1007/s10404-019-2219-9.

[71] V. Loisel et al. “Inertia-driven particle migration and mixing in a wall-bounded laminar suspension flow”. In: *Physics of Fluids* 27.12 (2015). ISSN: 10897666. DOI: 10.1063/1.4936402.

[72] P. Lösch et al. “Fractionating of finest particles using cross-flow separation with superimposed electric field”. In: *Separation and Purification Technology* 257.October 2020 (2021). ISSN: 18733794. DOI: 10.1016/j.seppur.2020.117820.

[73] E. Loth and A. J. Dorgan. “An equation of motion for particles of finite Reynolds number and size”. In: *Environmental Fluid Mechanics* 9.2 (2009), pp. 187–206. ISSN: 1573-1510. DOI: 10.1007/s10652-009-9123-x.

[74] A. J. Mach et al. “Automated cellular sample preparation using a Centrifuge-on-a-Chip”. In: *Lab on a Chip* 11.17 (2011), p. 2827. ISSN: 1473-0197. DOI: 10.1039/c1lc20330d.

[75] J. M. Martel and M. Toner. “Inertial Focusing in Microfluidics”. In: *Annual Review of Biomedical Engineering* 16.1 (2014), pp. 371–396. ISSN: 1523-9829. DOI: 10.1146/annurev-bioeng-121813-120704.

[76] M. R. Maxey and J. J. Riley. “Equation of motion for a small rigid sphere in a nonuniform flow”. In: *Physics of Fluids* 26.4 (1983), pp. 883–889. ISSN: 10706631. DOI: 10.1063/1.864230.

[77] R. Mei. "An approximate expression for the shear lift force on a spherical particle at finite reynolds number". In: *International Journal of Multiphase Flow* 18.1 (1992), pp. 145–147. ISSN: 03019322. DOI: 10.1016/0301-9322(92)90012-6.

[78] R. Mei and R. J. Adrian. "Flow past a sphere with an oscillation in the free-stream velocity and unsteady drag at finite reynolds number". In: *Journal of Fluid Mechanics* 237.323 (1992), pp. 323–341. ISSN: 14697645. DOI: 10.1017/S0022112092003434.

[79] C. D. Meinhart et al. "A PIV Algorithm for Estimating Time-Averaged Velocity Fields". In: *Journal of Fluids Engineering* 122.2 (June 2000), pp. 285–289. ISSN: 0098-2202. DOI: 10.1115/1.483256.

[80] C. Menter and D. Segets. "Scalable classification of nanoparticles: A proof of principle for process design". In: *Advanced Powder Technology* 30.11 (2019), pp. 2801–2811. ISSN: 15685527. DOI: 10.1016/j.apt.2019.08.027.

[81] A. A. Mohamad and A. Kuzmin. "A critical evaluation of force term in lattice Boltzmann method, natural convection problem". In: *International Journal of Heat and Mass Transfer* 53.5-6 (2010), pp. 990–996. ISSN: 00179310. DOI: 10.1016/j.ijheatmasstransfer.2009.11.014.

[82] S. Nagrath et al. "Isolation of rare circulating tumour cells in cancer patients by microchip technology". In: *Nature* 450.7173 (2007), pp. 1235–1239. ISSN: 14764687. DOI: 10.1038/nature06385.

[83] N. Nakagawa et al. "Inertial migration of a spherical particle in laminar square channel flows from low to high Reynolds numbers". In: *Journal of Fluid Mechanics* 779 (2015), pp. 776–793. ISSN: 14697645. DOI: 10.1017/jfm.2015.456.

[84] J. Oakey et al. "Particle Focusing in Staged Inertial Microfluidic Devices for Flow Cytometry". In: *Analytical Chemistry* 82.9 (May 2010), pp. 3862–3867. ISSN: 0003-2700. DOI: 10.1021/ac100387b.

[85] M. G. Olsen and R. J. Adrian. "Out-of-focus effects on particle image visibility and correlation in microscopic particle image velocimetry". In: *Experiments in Fluids* 29.7 (Dec. 2000), S166–S174. ISSN: 0723-4864. DOI: 10.1007/s003480070018.

[86] V. Olszok et al. "Particle-induced nanobubble generation for material-selective nanoparticle flotation". In: *Colloids and Surfaces A: Physicochemical and Engineering Aspects* 592.February (2020), p. 124576. ISSN: 18734359. DOI: 10.1016/j.colsurfa.2020.124576.

[87] N. T. Ouellette et al. "A quantitative study of three-dimensional Lagrangian particle tracking algorithms". In: *Experiments in Fluids* 40.2 (2006), pp. 301–313. ISSN: 07234864. DOI: 10.1007/s00348-005-0068-7.

[88] J.-S. Park and H.-I. Jung. "Multiorifice Flow Fractionation: Continuous Size-Based Separation of Microspheres Using a Series of Contraction/Expansion Microchannels". In: *Analytical Chemistry* 81.20 (Oct. 2009), pp. 8280–8288. ISSN: 0003-2700. DOI: 10.1021/ac9005765.

[89] S. N. Podoynitsyn et al. "Barrier contactless dielectrophoresis: A new approach to particle separation". In: *Separation Science Plus* 2.2 (2019), pp. 59–68. DOI: 10.1002/sscp.201800128.

[90] M. Raffel et al. *Particle Image Velocimetry: A Practical Guide*. Experimental Fluid Mechanics. Springer Berlin Heidelberg, 2007. ISBN: 9783540723073.

[91] M. Raffel et al. *Particle Image Velocimetry*. Cham: Springer International Publishing, 2018. ISBN: 978-3-319-68851-0. DOI: 10.1007/978-3-319-68852-7.

[92] S. Reinecke et al. "DEM-LBM simulation of multidimensional fractionation by size and density through deterministic lateral displacement at various Reynolds numbers". In: *Powder Technology* 385 (Feb. 2021), pp. 418–433. ISSN: 00325910. DOI: 10.1016/j.powtec.2021.02.062.

[93] M. Rossi and C. J. Kähler. "Optimization of astigmatic particle tracking velocimeters". In: *Experiments in Fluids* 55.9 (Sept. 2014), p. 1809. ISSN: 0723-4864. DOI: 10.1007/s00348-014-1809-2.

[94] P. G. Saffman. "The lift on a small sphere in a slow shear flow". In: *Journal of Fluid Mechanics* 22.2 (1965), pp. 385–400. ISSN: 14697645. DOI: 10.1017/S0022112065000824.

[95] P. Sajeesh and A. K. Sen. "Particle separation and sorting in microfluidic devices: A review". In: *Microfluidics and Nanofluidics* 17.1 (2014), pp. 1–52. ISSN: 16134990. DOI: 10.1007/s10404-013-1291-9.

[96] J. G. Santiago et al. "A particle image velocimetry system for microfluidics". In: *Experiments in Fluids* 25.4 (1998), pp. 316–319. ISSN: 07234864. DOI: 10.1007/s003480050235.

[97] E. Schach et al. "Multidimensional characterization of separation processes – Part 1: Introducing kernel methods and entropy in the context of mineral processing using SEM-based image analysis". In: *Minerals Engineering* 137.November 2018 (2019), pp. 78–86. ISSN: 08926875. DOI: 10.1016/j.mineng.2019.03.026.

[98] D. Schanz et al. "Shake-The-Box: Lagrangian particle tracking at high particle image densities". In: *Experiments in Fluids* 57.5 (2016), pp. 1–27. ISSN: 07234864. DOI: 10.1007/s00348-016-2157-1.

[99] S. Scharnowski et al. "A new look on the "Valid Detection Probability" of PIV Vectors". In: *LXLASER2018: 19th International Symposium on the Application of Laser and Imaging Techniques to Fluid Mechanics*. 2018.

[100] J. A. Schonberg and E. J. Hinch. “Inertial migration of a sphere in Poiseuille flow”. In: *Journal of Fluid Mechanics* 203 (June 1989), pp. 517–524. ISSN: 0022-1120. DOI: 10.1017/S0022112089001564.

[101] J. Schreier and U. Bröckel. “Multidimensional separation due to selective spherical agglomeration—Evidence of shape separation via X-ray microtomography”. In: *Particuology* 58 (2021), pp. 316–323. ISSN: 22104291. DOI: 10.1016/j.partic.2021.04.003.

[102] A. Sciacchitano. “Uncertainty quantification in particle image velocimetry”. In: *Measurement Science and Technology* 30.9 (2019). ISSN: 13616501. DOI: 10.1088/1361-6501/ab1db8.

[103] A. Sciacchitano and B. Wieneke. “PIV uncertainty propagation”. In: *Measurement Science and Technology* 27.8 (2016). ISSN: 13616501. DOI: 10.1088/0957-0233/27/8/084006.

[104] A. Sciacchitano et al. “Collaborative framework for PIV uncertainty quantification: Comparative assessment of methods”. In: *Measurement Science and Technology* 26.7 (2015). ISSN: 13616501. DOI: 10.1088/0957-0233/26/7/074004.

[105] A. Sciacchitano et al. “PIV uncertainty quantification by image matching”. In: *Measurement Science and Technology* 24.4 (2013). ISSN: 13616501. DOI: 10.1088/0957-0233/24/4/045302.

[106] G. Segré and A. Silberberg. “Behaviour of macroscopic rigid spheres in Poiseuille flow Part 1. Determination of local concentration by statistical analysis of particle passages through crossed light beams”. In: *Journal of Fluid Mechanics* 14.1 (Sept. 1962), pp. 115–135. ISSN: 0022-1120. DOI: 10.1017/S002211206200110X.

[107] G. Segré and A. Silberberg. “Behaviour of macroscopic rigid spheres in Poiseuille flow Part 2. Experimental results and interpretation”. In: *Journal of Fluid Mechanics* 14.1 (Sept. 1962). Ed. by Intergovernmental Panel on Climate Change, pp. 136–157. ISSN: 0022-1120. DOI: 10.1017/S0022112062001111.

[108] T. S. Sim et al. “Multistage-multiorifice flow fractionation (MS-MOFF): Continuous size-based separation of microspheres using multiple series of contraction/expansion microchannels”. In: *Lab on a Chip* 11.1 (2011), pp. 93–99. ISSN: 14730189. DOI: 10.1039/c0lc00109k.

[109] B. Skarman et al. *Simultaneous 3D-PIV and temperature measurements using a new CCD-based holographic interferometer*. 1996. DOI: 10.1016/0955-5986(96)00006-4.

[110] B. L. Smith and W. L. Oberkampf. “Limitations of and Alternatives to Traditional Uncertainty Quantification for Measurements”. In: *Volume 1D, Symposia: Transport Phenomena in Mixing; Turbulent Flows; Urban Fluid Mechanics; Fluid Dynamic Behavior of Complex Particles; Analysis of Elementary Processes in Dispersed Multiphase Flows; Multiphase Flow With Heat/Mass Transfer in Process Tec.* American Society of Mechanical Engineers, Aug. 2014, pp. 1–12. ISBN: 978-0-7918-4624-7. DOI: 10.1115/FEDSM2014-22068.

[111] X. Song et al. “A new model for predicting drag coefficient and settling velocity of spherical and non-spherical particle in Newtonian fluid”. In: *Powder Technology* 321 (2017), pp. 242–250. ISSN: 1873328X. DOI: 10.1016/j.powtec.2017.08.017.

[112] T. Spengler et al. “Integrated planning of acquisition, disassembly and bulk recycling: A case study on electronic scrap recovery”. In: *OR Spectrum* 25.3 (2003), pp. 413–442. ISSN: 14366304. DOI: 10.1007/s00291-003-0119-5.

[113] M. Stieß. *Mechanische Verfahrenstechnik - Partikeltechnologie 1*. Springer-Lehrbuch. Berlin, Heidelberg: Springer Berlin Heidelberg, 2009. ISBN: 978-3-540-32551-2. DOI: 10.1007/978/3-540-32552-9.

[114] M. Suwa and H. Watarai. “Magnetoanalysis of micro/nanoparticles: A review”. In: *Analytica Chimica Acta* 690.2 (2011), pp. 137–147. ISSN: 00032670. DOI: 10.1016/j.aca.2011.02.019.

[115] F. Takemura and J. Magnaudet. “The transverse force on clean and contaminated bubbles rising near a vertical wall at moderate Reynolds number”. In: *Journal of Fluid Mechanics* 495.495 (2003), pp. 235–253. ISSN: 00221120. DOI: 10.1017/S0022112003006232.

[116] A. H. Talasaz et al. “Isolating highly enriched populations of circulating epithelial cells and other rare cells from blood using a magnetic sweeper device”. In: *Proceedings of the National Academy of Sciences of the United States of America* 106.10 (2009), pp. 3970–3975. ISSN: 00278424. DOI: 10.1073/pnas.0813188106.

[117] B. H. Timmins et al. “A method for automatic estimation of instantaneous local uncertainty in particle image velocimetry measurements”. In: *Experiments in Fluids* 53.4 (2012), pp. 1133–1147. ISSN: 07234864. DOI: 10.1007/s00348-012-1341-1.

[118] L. Torobin and W. Gauvin. “Fundamnetal aspects of solid-gas flow part:I Introductory concepts and idelized sphere motion in viscous regime”. In: *The Canadian Journal of Chemical Engineering* 37.4 (1959), pp. 129–141.

[119] P. Vasseur and R. G. Cox. “The lateral migration of spherical particles sedimenting in a stagnant bounded fluid”. In: *Journal of Fluid Mechanics* 80.3 (1977), pp. 561–591. ISSN: 14697645. DOI: 10.1017/S0022112077001840.

[120] L. Wakaba and S. Balachandar. “On the added mass force at finite Reynolds and acceleration numbers”. In: *Theoretical and Computational Fluid Dynamics* 21.2 (2007), pp. 147–153. ISSN: 09354964. DOI: 10.1007/s00162-007-0042-5.

[121] F. Wang et al. “Metals recovery from dust derived from recycling line of waste printed circuit boards”. In: *Journal of Cleaner Production* 165 (2017), pp. 452–457. ISSN: 09596526. DOI: 10.1016/j.jclepro.2017.07.112.

[122] L. Wang and D. S. Dandy. “High-Throughput Inertial Focusing of Micrometer- and Sub-Micrometer-Sized Particles Separation”. In: *Advanced Science* 4.10 (2017). ISSN: 21983844. DOI: 10.1002/advs.201700153.

[123] P. Wang et al. “Particle dynamics and effective temperature of jammed granular matter in a slowly sheared three-dimensional Couette cell”. In: *Physical Review E - Statistical, Nonlinear, and Soft Matter Physics* 77.6 (2008), pp. 1–15. ISSN: 15393755. DOI: 10.1103/PhysRevE.77.061309.

[124] S. Wegt et al. *Computational Study on the Erosive Surface Degradation in a Pipe Elbow by Relevance to Internal Combustion Engine Cooling Systems*. June 2020.

[125] J. Westerweel. “Fundamentals of digital particle image velocimetry”. In: *Measurement Science and Technology* 8.12 (1997), pp. 1379–1392. ISSN: 09570233. DOI: 10.1088/0957-0233/8/12/002.

[126] S. Wiederseiner et al. “Refractive-index and density matching in concentrated particle suspensions: A review”. In: *Experiments in Fluids* 50.5 (2011), pp. 1183–1206. ISSN: 07234864. DOI: 10.1007/s00348-010-0996-8.

[127] B. Wieneke. “PIV uncertainty quantification from correlation statistics”. In: *Measurement Science and Technology* 26.7 (July 2015), p. 074002. ISSN: 0957-0233. DOI: 10.1088/0957-0233/26/7/074002.

[128] C. E. Willert. “The fully digital evaluation of photographic PIV recordings”. In: *Flow, Turbulence and Combustion* 56.2-3 (1996), pp. 79–102. ISSN: 13866184.

[129] C. E. Willert and M. Gharib. “Digital particle image velocimetry”. In: *Experiments in Fluids* 10.4 (1991), pp. 181–193. ISSN: 07234864. DOI: 10.1007/BF00190388.

[130] Z. Xue et al. “Particle image velocimetry correlation signal-to-noise ratio metrics and measurement uncertainty quantification”. In: *Measurement Science and Technology* 25.11 (2014). ISSN: 13616501. DOI: 10.1088/0957-0233/25/11/115301.

[131] Y. Ying and Y. Lin. “Inertial Focusing and Separation of Particles in Similar Curved Channels”. In: *Scientific Reports* 9.1 (2019), pp. 1–12. ISSN: 20452322. DOI: 10.1038/s41598-019-52983-z.

[132] D. Yuan et al. “Dean-flow-coupled elasto-inertial particle and cell focusing in symmetric serpentine microchannels”. In: *Microfluidics and Nanofluidics* 23.3 (Mar. 2019), p. 41. ISSN: 1613-4982. DOI: 10.1007/s10404-019-2204-3.

[133] L. Zeng et al. “Wall-induced forces on a rigid sphere at finite Reynolds number”. In: *Journal of Fluid Mechanics* 536 (2005), pp. 1–25. ISSN: 00221120. DOI: 10.1017/S0022112005004738.

[134] J. Zhang et al. “Fundamentals and applications of inertial microfluidics: A review”. In: *Lab on a Chip* 16.1 (2016), pp. 10–34. ISSN: 14730189. DOI: 10.1039/c5lc01159k.

[135] J. Zhang et al. “Inertial particle separation by differential equilibrium positions in a symmetrical serpentine micro-channel”. In: *Scientific Reports* 4.1 (May 2014), p. 4527. ISSN: 2045-2322. DOI: 10.1038/srep04527.

[136] J. Zhang et al. “Particle inertial focusing and its mechanism in a serpentine microchannel”. In: *Microfluidics and Nanofluidics* 17.2 (Aug. 2014), pp. 305–316. ISSN: 1613-4982. DOI: 10.1007/s10404-013-1306-6.

A. Particle focusing behavior

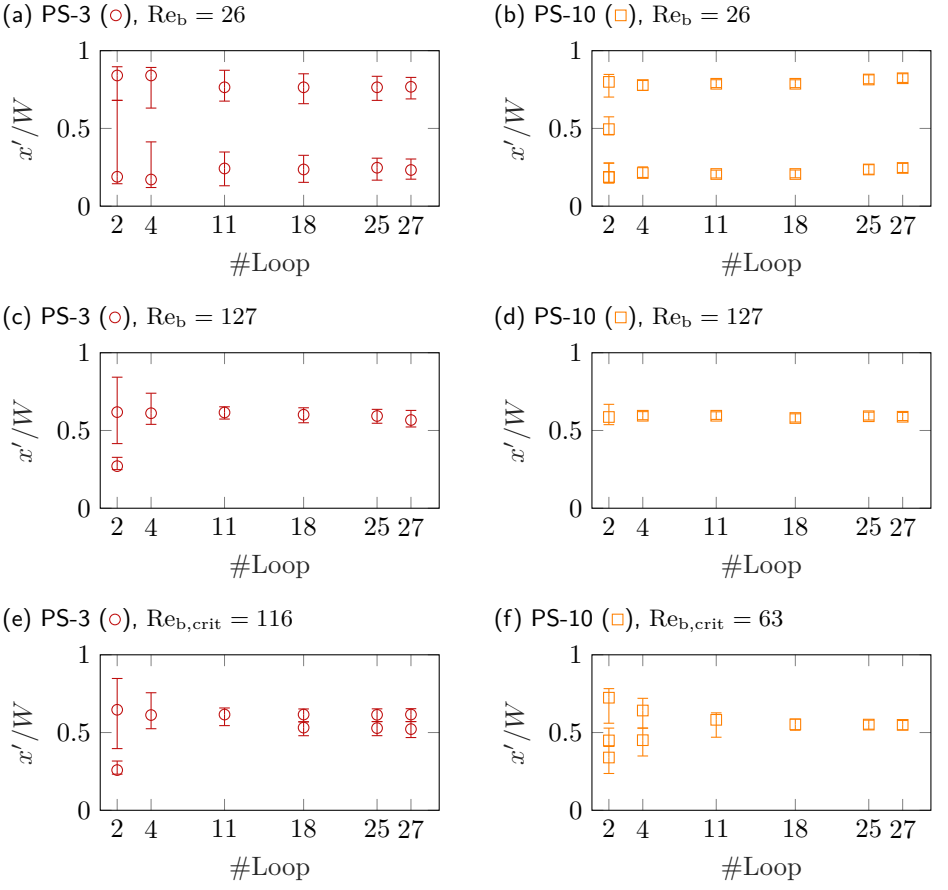

Figure A.1.: Normalized particle streak locations and widths as a function of the measurement location for (a) PS-3 particles at $\mathrm{Re_b} = 26$; (b) PS-10 particles at $\mathrm{Re_b} = 26$; (c) PS-3 particles at $\mathrm{Re_b} = 127$; (d) PS-10 particles at $\mathrm{Re_b} = 127$; (e) PS-3 particles at $\mathrm{Re_{b,crit}} = 116$ and (f) PS-3 particles at $\mathrm{Re_{b,crit}} = 63$.

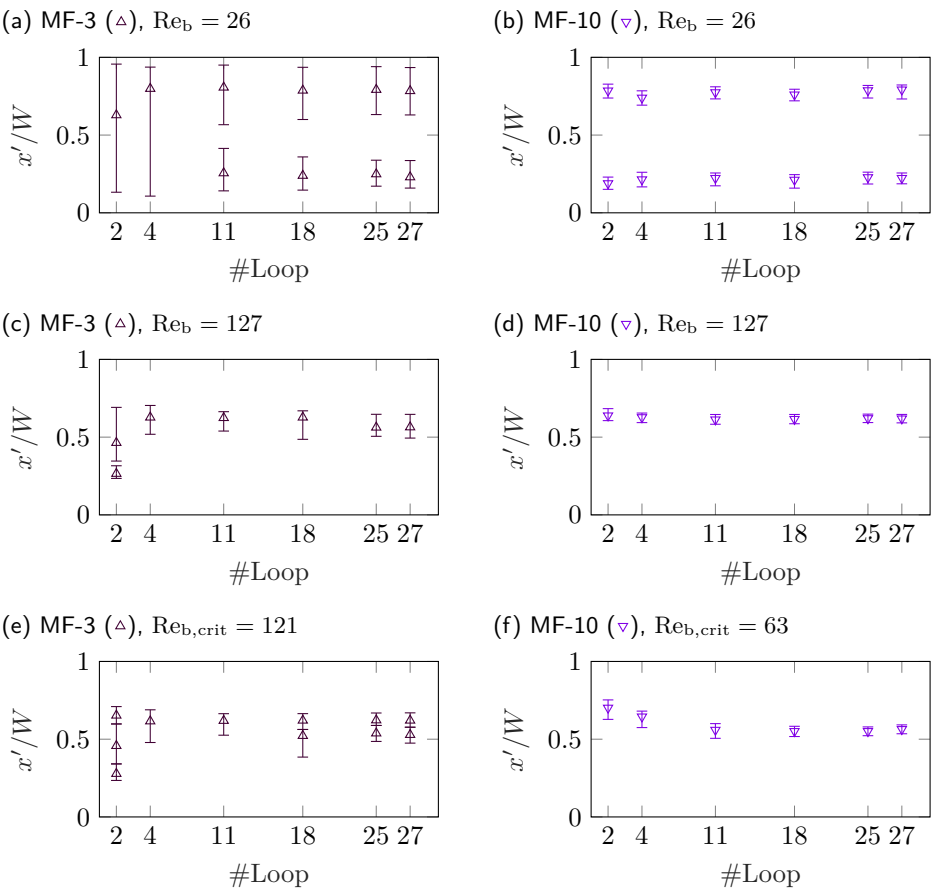

Figure A.2.: Normalized particle streak locations and widths as a function of the measurement location for (a) MF-3 particles at $\mathrm{Re_b} = 26$; (b) MF-10 particles at $\mathrm{Re_b} = 26$; (c) MF-3 particles at $\mathrm{Re_b} = 127$; (d) MF-10 particles at $\mathrm{Re_b} = 127$; (e) MF-3 particles at $\mathrm{Re_{b,crit}} = 121$ and (f) MF-3 particles at $\mathrm{Re_{b,crit}} = 63$.

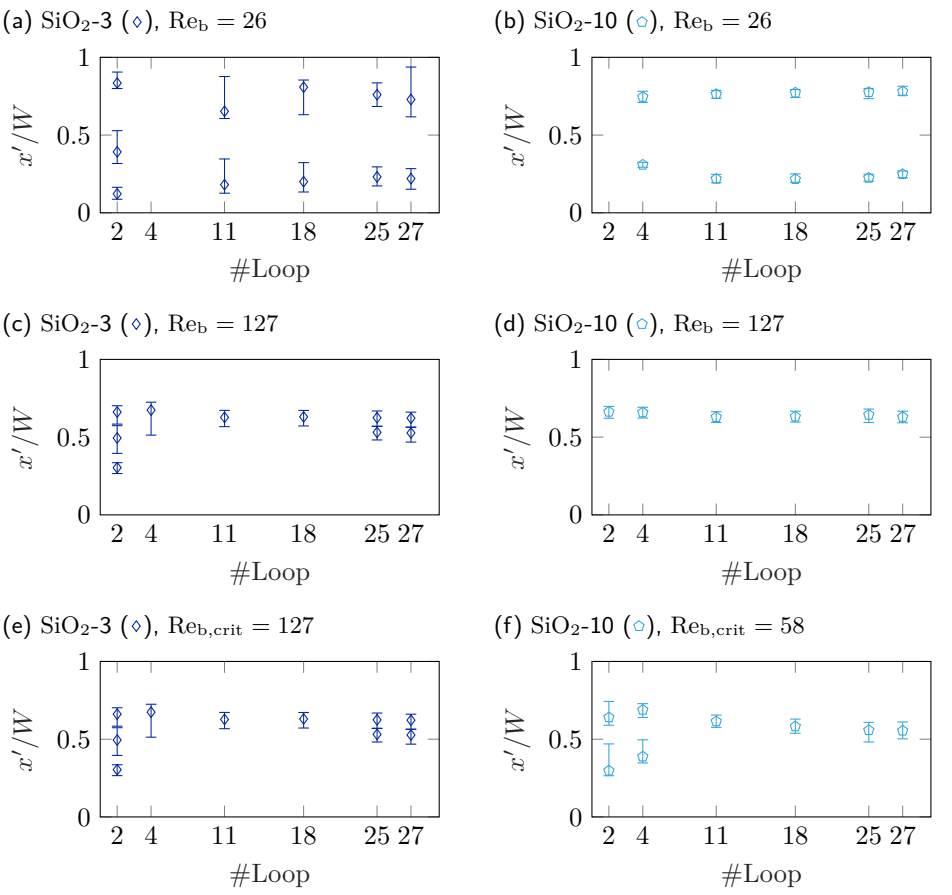

Figure A.3.: Normalized particle streak locations and widths as a function of the measurement location for (a) SiO_2-3 particles at $Re_b = 26$; (b) SiO_2-10 particles at $Re_b = 26$; (c) SiO_2-3 particles at $Re_b = 127$; (d) SiO_2-10 particles at $Re_b = 127$; (e) SiO_2-3 particles at $Re_{b,crit} = 127$ and (f) SiO_2-3 particles at $Re_{b,crit} = 58$.

B. Acknowledgements

At this point I would like to thank all the people who supported and believed in me during my work as a research associate at the Chair of Hydraulic Fluid Machinery of the Ruhr-University of Bochum and at the Institute for Fluid Mechanics and Aerodynamics of the Technical University of Darmstadt.

I would like to express my deepest thanks to Prof. Dr.-Ing. Jeanette Hussong for supervising my work during the last years. Without the numerous discussions and advices this work would not have been possible.

I am grateful to Prof. Dr.-Ing. Christian Cierpka for acting as co-examiner.

My special thanks go to Prof. Dr.-Ing. Harald Kruggel-Emden and Simon R. Reinecke for the great collaboration during our work in the priority program SPP 2045 of the German research foundation (DFG). The permanent exchange has been extraordinarily important for me.

I wish to thank all the friends and colleagues at the Chair of Hydraulic Fluid Machinery of the Ruhr-University Bochum for the inspiring and always friendly atmosphere. I would also like to extend my gratitude to all the friends and colleagues at the Institute for Fluid Mechanics and Aerodynamics of the Technical University of Darmstadt for the warm welcome and the fruitful discussions.

I would like to acknowledge the assistance of Dr.-Ing. Stephan Kordel, Maximilian Lausch, Bastian Stumpf and Jens Piloth with proofreading.

Thanks go also to my family and my friends who trusted and encouraged me in difficult times.

Last, but not least, I am deeply indebted to my wife Sandra who always supported and never lost patience with me.

Financial support from the German research foundation (DFG-SPP 2045) is gratefully acknowledged (HU2264/3-1 | HU2264/3-2).